

*Evaporation of Thin Lubricant Films under Laminar and Turbulent  
Boundary Layers*

by

*Stephen James Gill*

A thesis  
presented to the University of Waterloo  
in fulfilment of the  
thesis requirements for the degree of  
*Master of Applied Science*  
in  
*Mechanical Engineering*

Waterloo, Ontario, Canada, 2019

© Stephen James Gill 2019

## **Author's Declaration**

This thesis consists of material all of which I authored or co-authored: see Statement of Contributions included in the thesis. This is a true copy of the thesis, including any required final revisions, as accepted by my examiners.

I understand that my thesis may be made electronically available to the public.

## Statement of Contributions

Section 3.2 of this thesis paraphrases content featured within a paper which has been submitted for publication to ASME, Journal of Fluids Engineering. The paper was coauthored by myself, my supervisor (Prof. Xianguo Li), Dr. Burak Ahmet Tuna, and Prof. Serhiy Yarusevych. I primarily authored the text of the paper, and performed the lab experiments presented therein. The passages in question are located on pp. 43 – 44 and concern the experimental setup for the PIV measurements presented in this study. Likewise, Sections 3.3.4 and 4.2 feature figures initially prepared for the same publication (Figures 3-8, 3-9, and 4-4 – 4-8).

Section 3.2 and 3.3.3 also reference an accepted paper by Dr. Burak Ahmet Tuna, Prof. Li, and Prof. Yarusevych [46] which details the duct flow development measurements performed with the same apparatus. I had no part in authoring the paper or analyzing the post-processed results, although I contributed to conducting the experimental measurements.

## Abstract

The evaporation of engine oil hydrocarbons from the cylinder liner of internal combustion engines is a significant contributor to engine emissions. This evaporation occurs from the thin films deposited by the piston compression ring as it sweeps along the liner. Establishing the magnitude of the liner evaporation with respect to different lubricant and engine conditions is therefore important to both engine performance and oil consumption. The contribution from liner evaporation to oil consumption has been the subject of several experimental studies which show reasonable agreement with liner evaporation models employing one-dimensional heat and mass transfer. However, models normally eschew specification of the convective mass transfer conditions at the liquid interface, opting instead to employ heat-mass transfer analogies for given convective heat transfer conditions. Direct measurement of the evaporation of discrete oil films under turbulent boundary layer flow is therefore a useful comparative tool for evaluating model performance and methodology, especially for full-engine simulations which employ submodels for liner evaporation.

This study experimentally investigates the effects of laminar and turbulent boundary layers on the evaporation of thin, liquid oil films. A wind tunnel, incorporating a flow conditioner and test section, is designed and validated in order to produce repeatable boundary layer flows within an aspect ratio 2 rectangular duct ( $20 \text{ mm} \times 40 \text{ mm}$ ) with a length of  $1 \text{ m}$  ( $\sim 37.5D_h$ ). Particle image velocimetry (PIV) is used to characterize the velocity fields and turbulence statistics within the test section. Reynolds numbers based on hydraulic diameter of 10,650, 17,750, and 35,500 are considered, with grid-generated inlet turbulence being manipulated by wire-meshes and validated by hot-wire measurement. The evaporation of oil films with initial thicknesses of  $50 \mu\text{m}$  and temperatures of  $50^\circ\text{C}$  are then measured directly by an analytical microbalance for different exposures under the laminar and turbulent boundary layers with varying levels of near-wall turbulence intensity and shape. Reynolds number is found to have a significant effect on the evaporation rate. Specifically, increasing near-wall velocity gradient is found to increase the rate of evaporation. Varying near-wall turbulence intensity is shown to have little effect for the length scales of the study, implying that the shear velocity and transport within the viscous sublayer are the predominant parameters governing the convection-limited mass transfer.

# Acknowledgements

First and foremost, I wish to thank my supervisor, Prof. Xianguo Li for his contributions to my work. His advice was greatly appreciated when I struggled and invaluable throughout my degree.

Similarly, I would like to thank the members of my examining committee, Prof. Serhiy Yarusevych and Prof. Roydon Fraser, for their patience and insight.

I would also like to express my profound thanks to Dr. Burak Ahmet Tuna, without whom I would not have completed this thesis. Burak was my constant mentor during my experimental work, and introduced me to the finer points of fluid measurement techniques.

My fellow research group members have also been a great source of support, for their advice both academic and practical.

To my friends and family, I wish to say thank you for your tireless support while I completed my degree.

Finally, I wish to thank the machinists working for the University of Waterloo Engineering Department and Machine Shop. When I couldn't mill or turn something myself you folks did so peerlessly.

For my kith and kin,  
and those no longer with us,  
who kept me going.

# Table of Contents

Author’s Declaration.....	ii
Statement of Contributions.....	iii
Abstract.....	iv
Acknowledgements.....	v
List of Figures.....	ix
List of Tables.....	xii
Nomenclature.....	xiii
1 Introduction.....	1
1.1 Automotive Lubricant Overview.....	2
1.2 Lubricant Contribution to Emissions.....	3
1.3 Engine Oil Consumption Mechanisms.....	5
1.4 Boundary Layer Flow.....	8
1.4.1 Developing Duct Flow.....	11
1.4.2 Law of the Wall.....	12
1.4.3 Airflow Within an Engine Cylinder.....	14
1.5 Lubricant Films on the Cylinder Liner.....	15
1.6 Scope and Outline of Thesis.....	16
2 Literature Review.....	18
2.1 Evaporation under Boundary Layer Flow.....	18
2.2 Multicomponent Mixture Evaporation.....	21
2.3 Cylinder Liner Evaporation Modelling.....	24
2.5 Gap In Literature.....	26
2.6 Approach.....	26
3 Boundary Layer Measurements.....	28
3.1 Wind Tunnel Design.....	28
3.2 Experimental Setup.....	37
3.3 Flow Characterization.....	45
3.3.1 Experimental Conditions.....	45
3.3.2 Flow Conditioner Performance.....	46
3.3.3 Duct Flow Measurements.....	48

3.3.4	Evaporation Test Section PIV Measurements	50
3.3.5	Law of the Wall	52
4	Evaporation Measurements.....	56
4.1	Experimental Setup	56
4.2	Evaporation Results	64
5	Conclusions.....	74
6	Future Work.....	76
	References.....	77
	Appendix A – Blasius Laminar Boundary Layer Solution .....	84
	Appendix B – Wind Tunnel Design Drawings .....	86
	Appendix C – Detailed Test Section Flow .....	96
	Appendix D – Evaporation Measurement Data.....	115



# List of Figures

Figure 1-1.	Schematic of a typical, two-dimensional boundary layer flow over a flat plate where the flow transitions from laminar to turbulent .....	9
Figure 3-1.	Overall layout of the flow conditioner, including major changes between inlet and outlet cross-sections for different components.....	30
Figure 3-2.	Final contraction geometry resulting from the Morel axisymmetric design method, including equivalent inlet and outlet geometries.....	33
Figure 3-3.	Major components of the evaporation test section and their assembly. Also shown are the sample holder inset geometry and coordinate system.....	40
Figure 3-4.	General coordinate system and duct geometry implemented for the experimental fluids measurements.....	41
Figure 3-5.	Experimental setups for experimental fluids measurements .....	42
Figure 3-6.	Perturbation of the streamwise velocity and turbulence intensity for $Re_{D_h} = 1.0 \times 10^4$ , $1.7 \times 10^4$ , and $3.5 \times 10^4$ at the contraction exit .....	47
Figure 3-7.	Shape factor variation of the boundary layer within the $x$ - $y$ plane at the duct centreline ( $z = 0$ ) for Grid 3 (red) and Baseline (black) inlet conditions.....	49
Figure 3-8.	Convergence of downstream velocity profiles for each Reynolds number and inlet condition. Grid 1 and 2 cases omitted for clarity in a).....	51
Figure 3-9.	Velocity profiles above the sample holder at each axial location ( $x/a = 2$ and $45$ ), shown over the length of inset ( $z = 0$ ) and across its half-width ( $x'/a = 0.5$ ) .....	52
Figure 3-10.	$u^+$ profiles within the $x$ - $y$ plane at $x'/a = -0.1$ ( $x'/a = 45$ ) for each Reynolds number case under the a) Baseline and b) Grid 3 inlet conditions. Profiles are compared to either the Musker profile (black) or $u^+ = y^+$ (red).....	54
Figure 4-1.	Main components of heated parts within the evaporation test section and the clearances between them .....	57
Figure 4-2.	IR measurements of a $50 \mu\text{m}$ oil film and the sample holder. Showing a) the change in film thickness with time under approximately the Baseline, $Re_{D_h} = 1.7 \times 10^4$ , b) the associated experimental setup, and c) temperature distribution over the sample holder inset for $\bar{T} = 150^\circ\text{C}$ ( $\sigma = 1.1^\circ\text{C}$ ) .....	62
Figure 4-3.	Evaporation results and estimated evaporation rates for oil films for each airflow case, including the natural evaporation case .....	65
Figure 4-4.	Comparison of Baseline, $Re_{D_h} = 10,650$ , $17,750$ , and $35,500$ evaporation cases at $x/a = 2$ . Showing a) film evaporation and b) velocity profiles. Subfigures show same properties with relevant parameters scaled by $\delta^*$ . Solid black line in b) denotes the Blasius laminar boundary layer .....	67
Figure 4-5.	Comparison of Baseline and Grid 3 cases for $Re_{D_h} = 10,650$ at $x/a = 2$ . Showing a) film evaporation, b) velocity profiles, and c) turbulence intensities .....	68

Figure 4-6.	Comparison of Baseline and Grid 1 – 3 cases for $Re_{D_h} = 17,750$ at $x/a = 2$ . Showing a) film evaporation, b) velocity profiles, and c) turbulence intensities.....	69
Figure 4-7.	Comparison of Baseline, $Re_{D_h} = 10,650$ and $17,750$ cases at $x/a = 45$ . Showing a) film evaporation, b) velocity profiles, and c) turbulence intensities .....	71
Figure 4-8.	Evaporation rates from linear regression of forced convection data ( $\dot{m}_f$ ) relative to natural evaporation rate ( $\dot{m}_n$ ). Shown with respect to a) $Re_c$ and b) $Re_{\delta^*}$ for each Baseline and Grid case .....	72
Figure B-1.	Drawing of wind tunnel settling chamber and component assemblies (assy.).....	87
Figure B-2.	Drawing of test section mounting plate and insert geometry .....	88
Figure B-3.	Drawing of top, bottom, and side contraction components .....	89
Figure B-4.	Drawing of settling chamber mounting plates.....	90
Figure B-5.	Drawing of settling chamber screens and honeycomb holder .....	91
Figure B-6.	Drawing of diverging section (diffuser) side wall components .....	92
Figure B-7.	Drawing of diverging section (diffuser) top and bottom wall components .....	93
Figure B-8.	Drawing of top and bottom halves of the circular-rectangular transition.....	94
Figure B-9.	Drawing of transition mounting plates .....	95
Figure C-1.	Summary of PIV measurements for Baseline, $Re_{D_h} = 10,650$ case at $x/a = 2$ .....	97
Figure C-2.	Summary of PIV measurements for Baseline, $Re_{D_h} = 35,500$ case at $x/a = 45$ .....	97
Figure C-3.	Summary of PIV measurements for Baseline, $Re_{D_h} = 17,750$ case at $x/a = 2$ .....	98
Figure C-4.	Summary of PIV measurements for Baseline, $Re_{D_h} = 35,500$ case at $x/a = 2$ .....	98
Figure C-5.	Summary of PIV measurements for Grid 3, $Re_{D_h} = 10,650$ case at $x/a = 2$ .....	99
Figure C-6.	Summary of PIV measurements for Grid 1, $Re_{D_h} = 17,750$ case at $x/a = 2$ .....	100
Figure C-7.	Summary of PIV measurements for Grid 2, $Re_{D_h} = 17,750$ case at $x/a = 2$ .....	101
Figure C-8.	Summary of PIV measurements for Grid 3, $Re_{D_h} = 17,750$ case at $x/a = 2$ .....	102
Figure C-9.	Summary of PIV measurements for Grid 1, $Re_{D_h} = 35,500$ case at $x/a = 2$ .....	103
Figure C-10.	Summary of PIV measurements for Grid 2, $Re_{D_h} = 35,500$ case at $x/a = 2$ .....	104
Figure C-11.	Summary of PIV measurements for Grid 3, $Re_{D_h} = 35,500$ case at $x/a = 2$ .....	105
Figure C-12.	Summary of PIV measurements for Baseline, $Re_{D_h} = 17,750$ case at $x/a = 45$ .....	106
Figure C-13.	Summary of PIV measurements for Baseline, $Re_{D_h} = 35,500$ case at $x/a = 45$ .....	107
Figure C-14.	Summary of PIV measurements for Grid 3, $Re_{D_h} = 10,650$ case at $x/a = 45$ .....	108
Figure C-15.	Summary of PIV measurements for Grid 1, $Re_{D_h} = 17,750$ case at $x/a = 45$ .....	109

Figure C-16.	Summary of PIV measurements for Grid 2, $Re_{D_h} = 17,750$ case at $x/a = 45$ .....	110
Figure C-17.	Summary of PIV measurements for Grid 3, $Re_{D_h} = 17,750$ case at $x/a = 45$ .....	111
Figure C-18.	Summary of PIV measurements for Grid 1, $Re_{D_h} = 35,500$ case at $x/a = 45$ .....	112
Figure C-19.	Summary of PIV measurements for Grid 2, $Re_{D_h} = 35,500$ case at $x/a = 45$ .....	113
Figure C-20.	Summary of PIV measurements for Grid 3, $Re_{D_h} = 35,500$ case at $x/a = 45$ .....	114

## List of Tables

Table 3-1.	Screen design parameters for different $Re_{D_h}$ .....	36
Table 3-2.	Wire mesh dimensions for each turbulence grid. ....	39
Table 3-3.	Dry air properties at 19°C. ....	46
Table 4-1.	Experimental conditions for film evaporation measurements.....	61
Table C-1.	Colour scheme for $z/c$ locations.....	96
Table D-1.	Evaporation data for Natural Convection case ( $Gr_c = 3838$ ) .....	115
Table D-2.	Evaporation data for Baseline, $Re_{D_h} = 17,750$ case ( $x/a = 2$ ) .....	116
Table D-3.	Evaporation data for Baseline, $Re_{D_h} = 10,650$ case ( $x/a = 2$ ) .....	117
Table D-4.	Evaporation data for Baseline, $Re_{D_h} = 35,500$ case ( $x/a = 2$ ) .....	117
Table D-5.	Evaporation data for Grid 1, $Re_{D_h} = 10,650$ case ( $x/a = 2$ ).....	118
Table D-6.	Evaporation data for Grid 1, $Re_{D_h} = 17,750$ case ( $x/a = 2$ ).....	118
Table D-7.	Evaporation data for Grid 2, $Re_{D_h} = 17,750$ case ( $x/a = 2$ ).....	119
Table D-8.	Evaporation data for Grid 3, $Re_{D_h} = 17,750$ case ( $x/a = 2$ ).....	119
Table D-9.	Evaporation data for Baseline, $Re_{D_h} = 10,650$ case ( $x/a = 45$ ) .....	120
Table D-10.	Evaporation data for Baseline, $Re_{D_h} = 17,750$ case ( $x/a = 45$ ) .....	120

# Nomenclature

$\langle \rangle$	Time-averaged measured variable
$\bar{u}$	Time or spatially averaged variable, e.g. $u$
$\infty$	Subscript designating quantity outside a boundary layer
'	Superscript designating fluctuating variable, or indicating a derivative
$A$	Cross-sectional area ( $\text{m}^2$ )
$a$	Duct height (m)
$B$	Law of the wall constant
$B_e$	Experimentally measured cylinder bore diameter (m),
$b$	Duct width (m)
$C_f$	Friction coefficient
$c$	Film length, inset length, and inset width (m)
$c_i$	Concentration of species $i$ ( $\text{mol m}^{-3}$ )
$c_p$	Specific heat with respect to constant pressure ( $\text{kJ kg}^{-1} \text{K}^{-1}$ )
$D_h$	Hydraulic diameter (m)
$D_1, D_2$	Equivalent contraction inlet and outlet diameters (m)
$D, D_m$	Molecular diffusivity ( $\text{m}^2 \text{s}^{-1}$ )
$D_{t,y}$	Turbulent molecular diffusivity ( $\text{m}^2 \text{s}^{-1}$ )
$d$	Wire diameter (m)
$Gr$	Grashof number
$g_m$	Mass convection coefficient ( $\text{kg m}^{-2} \text{s}^{-1}$ )
$H$	Shape factor
$h$	Cylinder liner oil film thickness (m)
$h_f$	Film thickness in two-phase flow (m)
$h_{min}$	Minimum oil film thickness (m)
$K$	Static pressure drop coefficient
$k$	Thermal conductivity ( $\text{W m}^{-2} \text{K}$ )
$L$	Total length (m)
$L_e$	Duct entrance length (m)
$l, m$	Wavenumbers
$M$	Mesh wire spacing (centre to centre) (m)
$m_A$	Mass of air (kg)
$m_{\text{evap}}$	Evaporated mass per initial film area ( $\text{kg m}^{-2}$ )
$m_{\text{evap},t=0}$	Evaporated mass per initial film area prior to $t = 0$ ( $\text{kg m}^{-2}$ )
$m_F$	Mass of fuel (kg)
$m_f$	Final film mass (kg)

$m_i$	Initial film mass (kg)
$m_o$	Sample holder mass (kg)
$m_1$	Initial mass of sample holder and film (kg)
$m_2$	Final mass sample holder and film (kg)
$\dot{m}, \dot{m}_f$	Evaporation rate (mass flux) from film ( $\text{kg m}^{-2} \text{s}^{-1}$ )
$\dot{m}_n$	Evaporation rate from film under natural convection ( $\text{kg m}^{-2} \text{s}^{-1}$ )
$N$	Number of samples
$Nu$	Nusselt number
$n_i$	Number of molecules or species $i$ (mol), or a constant
$n_{\text{tot}}$	Total number of molecules
$P$	Wetted perimeter of duct (m)
$Pr$	Prandtl number
$p$	Pressure (Pa)
$p_i$	Vapour pressure of species $i$ in solution (Pa)
$p_i^*$	Vapour pressure of pure species $i$ (Pa)
$Re$	Reynolds number
$Sc$	Schmidt number
$Sh$	Sherwood number
$St$	Stanton number
$s$	Musker profile constant
$T_b$	Base temperature ( $^{\circ}\text{C}$ )
$T_f$	Film temperature ( $^{\circ}\text{C}$ )
$T_g$	Gas temperature ( $^{\circ}\text{C}$ )
$T_s$	Surface temperature ( $^{\circ}\text{C}$ )
$t$	Time, or exposure time (s)
$t_0$	Preheat time (s)
$U$	Characteristic velocity ( $\text{m s}^{-1}$ )
$u$	Streamwise ( $x$ ) velocity component ( $\text{m s}^{-1}$ )
$u_0$	Incoming perturbation (across $y, z$ ) of axial velocity to a screen ( $\text{m s}^{-1}$ )
$u_N$	Outgoing perturbation (across $y, z$ ) of axial velocity from a screen ( $\text{m s}^{-1}$ )
$u_{\tau}$	Shear velocity ( $\text{m s}^{-1}$ )
$u^+$	Streamwise velocity, wall scaling
$u_m^+$	Musker profile for velocity within inner region
$\mathbf{V}$	Velocity vector ( $\text{m s}^{-1}$ )
$\dot{V}_f/B$	Film volume flux per unit breadth in two-phase flow ( $\text{m}^2 \text{s}^{-1}$ )
$v$	Wall-normal ( $y$ ) velocity component ( $\text{m s}^{-1}$ )
$v$	Hot-wire voltage (V)

$w$	Cross-stream ( $z$ ) velocity component ( $\text{m s}^{-1}$ )
$w_e$	Average cylinder gas velocity, empirical function ( $\text{m}^2 \text{s}^{-1}$ )
$X$	Settling chamber screen spacing (m)
$x$	Streamwise/axial coordinate (m)
$x_i$	Mole fraction of species $i$
$x_m$	Location of contraction cubic match point (m)
$x_{\min}$	Location of minimum velocity wall pressure coefficient (m)
$x_o$	Virtual origin of contraction boundary layer (m)
$x'$	Axial coordinate from inset leading edge (m)
$Y$	Mass fraction
$y$	Wall normal coordinate (m)
$y_{vt}$	Smooth boundary layer viscous sublayer height (m)
$y_0$	Pool leading edge land roughness (m)
$y^+$	Wall-normal direction, wall scaling
$z$	Cross-stream coordinate (m)
$\alpha$	Thermal diffusivity ( $\text{m}^2 \text{s}^{-1}$ )
$\beta$	Mesh porosity
$\delta$	Boundary layer thickness (m)
$\delta^*$	Displacement thickness (m)
$\delta_d$	Mass boundary layer thickness (m)
$\epsilon$	Emissivity
$\zeta$	Contraction design parameter (m)
$\eta$	Similarity variable in Blasius solution
$\Theta$	Crank angle (degrees)
$\theta$	Momentum thickness (m)
$\theta_{i,j}$	Excess temperature at $i^{\text{th}}$ and $j^{\text{th}}$ location ( $^{\circ}\text{C}$ )
$\Phi$	Relative error function
$\phi$	Equivalence ratio
$\kappa$	von Kármán constant
$\mu$	Dynamic viscosity ( $\text{kg m s}^{-1}$ )
$\pi$	Ratio of a circles circumference to its diameter
$\rho$	Density ( $\text{kg m}^{-3}$ )
$\rho_o$	Oil density ( $\text{kg m}^{-3}$ )
$\sigma$	Standard deviation, or mesh solidity
$\tau_w$	Wall shear stress ( $\text{Pa s}$ )
$\nu$	Kinematic viscosity ( $\text{m}^2 \text{s}^{-1}$ )
$\psi$	Streamfunction
$\omega$	Engine speed ( $\text{s}^{-1}$ )

# 1 Introduction

The modern internal combustion (ICE) engine is ubiquitous in today's society, generating the mechanical power used by automobiles, aircraft, electric generators, and many other machines. Among the chief design concerns of an ICE are efficiency and the emission of combustion products. Climate change and air quality are paramount concerns, and as such controls have been placed on the emissions of several compounds found in ICE exhaust and are enforced by government regulation. Catalytic converters have been used for decades to limit the emission of pollutants such as carbon monoxide (CO), unburned hydrocarbons (HC), and nitrous oxides (NO<sub>x</sub>), although the emission of carbon dioxide (CO<sub>2</sub>) remains a challenge as a primary product of combustion and catalytic reactions. In addition, particulates (soot) are a significant product of diesel engines, although catalytic converters are capable of removing a large portion of the hydrocarbon species condensed on the solid carbon particles, known as the soluble organic fraction (SOF). Engine load, equivalence ratio (or fuel-air ratio), engine speed, and timing directly effect both cycle efficiency and the foregoing emissions. The equivalence ratio,  $\phi$ , is defined as,

$$\phi = \frac{m_F/m_A}{(m_F/m_A)_{st}} \quad (1-1)$$

which is a ratio of the actual fuel-to-air ratio and the stoichiometric fuel-air ratio, where there is sufficient air to react with all of the fuel. Lean combustion ( $\phi < 1$ ) increases engine efficiency, and reduces the emission of HC and CO, yet operates at near maximum production of NO<sub>x</sub> compounds and results in less power than richer combustion ( $\phi > 1$ ). The overall efficiency of an engine is also heavily impacted by the action of friction between components. Mechanical losses account for approximately 30% of the losses from power produced by the combustion cycle [1-3], and are mitigated by lubrication between the moving and stationary components.

Lubrication within the piston-cylinder tribosystem of a modern internal combustion engine is accomplished by liquid oil between the piston rings and cylinder liner. Thin, liquid lubricant films remain on the liner after the passage of the piston rings and are exposed to transient gas temperatures, liner temperatures, and turbulent airflow present in the cylinder



during operation. The lubricant used is almost always a liquid hydrocarbon mixture (oil), and due to the dynamics of the moving components within an ICE, and the heat generated, the hydrocarbons participate in the combustion cycle due to several different oil consumption mechanisms. Along with inertial loss mechanisms, evaporation from the cylinder liner is a significant contributor to engine oil consumption and consequently engine emissions [4, 5].

The hydrocarbon species composing the multicomponent lubricants, which are predominantly n-paraffins for synthetic and conventional oils, evaporate at varying rates governed by the vapour pressures of species at the liquid-gas interface, gas phase mass transfer conditions, and diffusion of species within the liquid phase. Especially in diesel engines, unburned lubricant present in the gas phase is a major contributor to the soluble organic fraction (SOF) of particulate emissions [6, 7]. In some cases, lubricant consumption can be the predominant source of n-paraffins and polycyclic aromatic hydrocarbons found in the SOF [7]. Therefore, the evaporation of oil films from the cylinder liner is of significant interest with respect to both engine performance and environmental considerations. The following sections provide context for the nature of engine lubricants and the conditions under which lubricant films are created and evaporate.

## 1.1 Automotive Lubricant Overview

In general, an automotive lubricant or oil is a mixture of liquid hydrocarbons components which facilitates lubrication between mechanical parts. The hydrocarbon mixtures which are combined to form the oil are referred to as *base stocks*. Automotive lubricants commonly fall into two categories which will be familiar to the layman: conventional and synthetic oils. The difference between the two is in how their base stocks are derived. For conventional oils, base stocks are distilled from crude oil (petroleum). Base stocks are defined as *paraffinic*, *naphthenic*, or *intermediate* based on the tendency of their composition, although each base stock is a combination of those compounds [1]. Synthetic oils are, generally, composed of base stocks which have been produced through chemical processes other than distillation from crude oil, including: synthesized hydrocarbons (from carbon monoxide and hydrogen), organic esters, and silicones, among others [1]. However, the practical definition of a synthetic oil is

very broad due to the varying degrees modern base stocks will include a blend of conventional and synthesized hydrocarbons [1]. SAE J357 [1] defines base stocks based on the following classifications, which provides a useful summary of the above: *refined petroleum base stocks*, *re-refined or recycled petroleum base stocks*, *synthetic base stocks*, and *partial synthetic base stocks*. Oil additives are also added in small quantities to increase a facet of the lubricants performance, including: pour point depressants, viscosity modifiers, anti-oxidants, detergents, detergent-inhibitors, and dispersants [1].

Since the primary goal of an engine oil is mechanical lubrication they are first and foremost classified based on their viscosities (rheological performance). SAE J300 [1] provides a classification method for engine oils based on viscosities measured at high and low temperatures via procedures outlined in several ASTM standards. This is necessary due to the decrease in viscosity with temperature experienced by liquid oils [1]. The classifications therein are represented by number and letter grades such as “5W-30”, and are the most common in North America. SAE J300 [1] uses two series of viscosity grades to classify single viscosity-grade oils, which are represented by a number with and without a ‘W’. The W designation means that the oil grade is based on both maximum low-temperature viscosity and minimum kinematic viscosity at 100°C, while no W indicates that the grade is based on a set of minimum and maximum kinematic viscosities at 100°C and a minimum high-shear ( $10^6 \text{ s}^{-1}$ ) viscosity at 150°C. Furthermore, multigrade oils are defined based on the maximum low-temperature viscosity of a W grade oil combined with the high-shear and kinematic viscosities of a non-W grade. An example of a multigrade oil would be the aforementioned “5W-30” oil. Many automotive oils are multigrade, which ensures predictable performance at both high and low temperatures. This is important because of the wide temperature conditions automotive engines are expected to operate under, from cold-start conditions during winter to the high engine load conditions where the cylinder temperature is highest.

## **1.2 Lubricant Contribution to Emissions**

Analysis of automotive engine exhaust shows that lubricating oil within the engine contributes directly to emissions. Engine emissions are the gaseous, solid, and liquid byproducts

of combustion that constitute engine exhaust. The common products of hydrocarbon combustion make up the majority of the engine exhaust: namely, nitrogen gas ( $\text{N}_2$ ), carbon dioxide ( $\text{CO}_2$ ), water vapour ( $\text{H}_2\text{O}$ ), and some oxygen gas ( $\text{O}_2$ ). However, more harmful compounds are also produced during and after the complexities of combustion within the cylinder, including: nitrous oxides ( $\text{NO}_x$ ), sulphur dioxide ( $\text{SO}_2$ ), and carbon monoxide ( $\text{CO}$ ). These gases are joined by unburned hydrocarbons, volatile organic compounds (VOCs), and solid particulate matter nucleated in the exhaust or formed on the cylinder/piston surfaces. In general these substances produce unwanted side-effects and therefore their production is limited by design, such as through catalytic converters and careful engine operation. Some prime examples of this would be the greenhouse effect caused by  $\text{CO}$  and  $\text{CO}_2$  and the adverse health affects of particulate matter, VOCs, and  $\text{SO}_2$ .

The role of lubricating oil in affecting emissions is primarily found in solid, particulate emissions. Due to loss mechanisms within the engine and fuel spray interaction with the engine surfaces, liquid oil and vaporized oil components are present among the cylinder gasses. Oil compounds can then become involved in the combustion process, or exhausted directly from the cylinder. Therefore, when particulate matter (soot) nucleates, organic compounds from the oil are adsorbed into the particle surfaces. These compounds, including paraffins and polycyclic aromatic hydrocarbons (PAH), are generally found in the soluble organic fraction (SOF) of the particles.

Several studies have determined that a significant portion of the particulate matter SOF found in diesel engine exhaust can be attributed to engine lubricants [6, 8], regardless of the fuel used except where low-quality fuels cause the particles to become saturated with fuel hydrocarbons [6]. In a study by P. T. Williams et al. [8] it was determined that lubricant contributes to 80 – 90% of the particulate SOF, and accounts for approximately 10% of the PAH found therein with fresh oil. Additionally, the lubricant contribution to polycyclic aromatic compounds (PAC) levels in the exhaust was found to be exacerbated by unburned diesel fuel “leaking” into the engine oil [8-10]. The PAH levels found in aged engine oil are also generally higher than that of diesel fuel [7], and can therefore be a more significant source of unburned PAH than the fuel itself. Paraffins from the engine oil are also a major part of its SOF contribution and account for 40% – 80% of emitted paraffins [7]. Higher contributions are

noticeable at higher mean “engine loads” [7], where engine load is the torque output of the engine (and proportional to power output). Similarly, lubricant makes significant contributions to the composition of nanoparticles (< 50 nm), where most of their mass composed of paraffins sourced in unburned fuel and engine oil [11].

The direct effect of engine oil on particulate emissions in general can also be considered, meaning the effect of lubricant properties such as viscosity and Noack volatility on the amount of particulates found in a DI diesel engine exhaust. Noack volatility is the result of a specification [10] for quantifying oil mixture volatility based on the percentage mass loss of the mixture when held at a given temperature (250°C). An increase in viscosity has been shown to result in decreased particulate emissions, with the effects of high and low-shear viscosities being similar [9, 12]. This is attributed to the formation of thicker films at lower viscosities, and encouragement of oil entrainment into reverse flow past the piston rings, which allows larger volumes of oil to enter the combustion chamber (higher consumption) [9]. Higher volatility was also shown to increase the amount of particulates present in the exhaust [12]. Additionally, the contribution of hydrocarbons from the engine oils to the particulate SOF was shown to increase with engine speed and decrease with engine load [6, 8, 12].

### **1.3 Engine Oil Consumption Mechanisms**

The consumption of oil within an IC engine is controlled by the motion and geometry of the piston-cylinder assembly as well as lubricant properties. Of particular importance to this study is the number and type of piston rings located in grooves around the circumference of the piston. These piston rings form the primary point of contact between the piston and the cylinder liner, and are where the lubricant acts to reduce friction and wear. These rings serve several purposes: forming a mechanical seal between the combustion chamber and crankcase; transporting lubricant along the cylinder liner; improving heat transfer from the piston to the cylinder liner; and scraping oil from the cylinder liner back to the piston skirt and sump. The top ring, or compression ring, provides the primary seal for the combustion chamber. The top ring groove is designed such that the high pressures within the combustion chamber act to press the ring against the cylinder liner, which improves the seal. The second ring, or wiper ring, is

intended to aid in removing excess oil from the cylinder liner while providing additional sealing. The last ring, or oil ring, is closest to the crankcase and is used to control the supply of oil to the upper regions of the piston. The most common number of rings found in four-stroke IC engines is three [2].

Oil consumption refers to the removal of liquid oil from the engine during operation. The mechanisms leading to oil consumption can be grouped into two categories: evaporative and inertial. Evaporative loss mechanisms are governed by convective mass transport of the oil components. One example is liner evaporation, where liquid oil present on the cylinder liner evaporates under high temperatures and airflow during the engine cycle. Similar evaporation occurs beneath the piston as well, where liquid oil can also be entrained into any blow-by gas flow (combustion gases which breach the piston rings and enter the crankcase). Oil constituents can therefore enter the combustion chamber if the blow-by gasses are vented into the intake manifold, and represent a loss mechanism regardless [2, 13].

Conversely, inertial loss mechanisms are controlled by the inertia of the piston-cylinder system. During operation liquid oil can accumulate at the piston top land [2, 13], and may be “thrown off” into the combustion chamber due to inertia donated by the piston during an upward stroke. A similar effect is created when pressures in the piston second land become higher than the combustion chamber pressure, creating a positive pressure gradient. Gas may then flow around the top ring groove, or through the gap in the compression ring, which can carry liquid and evaporated oil into the combustion chamber [2, 13]. In each case, the oil is most often removed from the cylinder via exhaust gases after liquid oil or evaporated constituents enter the bulk flow within the combustion chamber [2, 4, 13].

The contributions to oil consumption made by each mechanism have been explored extensively through bench and field testing with both test and production engines, respectively. In general, these tests were accomplished by subjecting oils with differing viscosities and volatilities to the same set of conditions and measuring the amount of oil consumption directly. While both viscosity and volatility are important characteristics to the rheological performance and longevity of an oil, they are also the most significant controllable parameters that relate to the consumption mechanisms. As such, relative differences in consumption can be related to differences in oil properties.

Volatility has been highlighted as one of the most important sources of oil consumption in both field tests [14, 15] and bench tests [14, 16]. Where the role of viscosity, and the contribution of inertial mechanisms to overall oil consumption, has been found to depend heavily on engine design [16], the role of evaporation and volatility is directly dependent on engine conditions and oil composition. In this case, volatility is the tendency for a liquid to form a vapour. Specifically, it can be defined as the standardized mass fraction lost when the mixture is held at a specific temperature (Noack volatility) [10], by mass or volume fraction lost based on a temperature range (distillation curve), or a similar boiling point distribution generated through a procedure such as in ASTM D2887 (gas chromatography) [17]. Test engine oil consumption has been found to increase by at least 1% for every 1% increase in species distilled at 371°C [14, 17] in test engines. However, consumption trends as high as 4.5% [14] and 3% [15] have been found in field tests. The contribution of volatility to consumption is also affected by engine temperature, where higher volatility oils (based on distillation curves) have been found to not only exhibit increasing oil consumption with increasing surface temperatures (piston and cylinder liner), but also a relatively larger increase for higher volatility oils [18]. This is expected based on how volatility is defined above, and the behaviour of vapour pressure with temperature [19], and serves to emphasize the importance of high temperature operation to evaporation within an engine.

The relative contribution from each loss mechanism is more difficult to measure than the role of bulk oil properties. However, a combination of modelling and experimental measurements can allow estimation of the relative contributions of each mechanism, as in the work of E. Yilmaz et al. [2, 13]. A sulphur-trace method was used to measure the transient oil consumption from a production engine concurrently with liner temperature, oil film thickness, and cylinder pressure. These measurements were conducted for various engine loads and speeds, and blow-by gas venting conditions. Combined with a cylinder liner evaporation model [4], the relative effects of liner evaporation, blow-by entrainment, and inertial mechanisms (the remainder) were determined. While oil consumption was found to increase with engine speed, the contributions from each source remained relatively the same [2, 13]. However, at low engine load, the inertial mechanisms were found to be the highest contributors to consumption (> 90%), while higher engine load was dominated by liner evaporation (> 40%) [2, 13]. Blow-

by entrainment was found to increase with engine load as well, but was relatively insignificant (< 15%). These results are supported by additional consumption modelling based on measured engine operating conditions [20, 21].

One key conclusion is that liner evaporation is the predominant source of evaporation within the cylinder, which is itself a major contributor to oil consumption (and thus emissions) at high engine-loads. Cylinder liner evaporation occurs primarily from the film of oil deposited onto the liner surface by the piston rings. Numerous models have been created to estimate the liner evaporation, and are affected by a number of factors: oil film thickness, distribution of liquid oil along the cylinder [22], oil composition, oil and gas temperatures (heat transfer to the film), and the gas phase velocity field. The gas phase flow within the cylinder is therefore particularly important, as it controls the convective mass transport from the film [19], and is largely responsible for the heat transfer at the liner.

## 1.4 Boundary Layer Flow

The heat and mass transfer between the liquid film and the gas phase within an engine cylinder is governed primarily by thin regions above the liquid surface known as *boundary layers*. In each case a quantity such as velocity, temperature, or species concentration varies from a bulk value in the gas phase to its value at the liquid surface or wall; the nature and degree of these gradients controls the transport of momentum, heat, and mass within the gas phase. In each case, there exists a quantity which governs the transport; kinematic viscosity ( $\nu$ ), thermal diffusivity ( $\alpha$ ), and molecular diffusivity ( $D$ ), respectively. The momentum boundary layer is of paramount importance in this case, as it jointly governs the rate at which heat and vaporized species are convected to and from the film.

With respect to the momentum (velocity) boundary layer, viscous fluid flow over a surface interacts via friction. Generally, fluid particles near a surface will tend to match the velocity of the surface because the force of cohesion between fluid particles is weaker than the adhesion force between the particles and the wall; this is known as the “no-slip” condition. This results in a boundary layer, a region where the relative velocity varies from zero at the surface to some relative velocity farther from the wall ( $U_\infty$ ). This smooth variation is governed by viscosity,

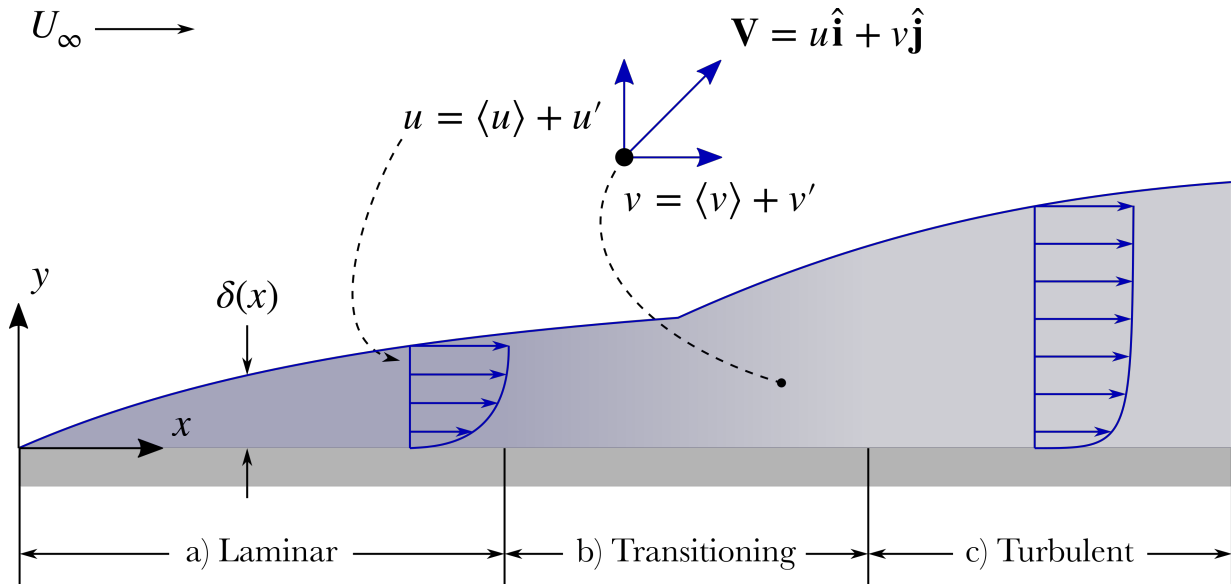


**Figure 1-1. Schematic of a typical, two-dimensional boundary layer flow over a flat plate where the flow transitions from laminar to turbulent.**

which causes a shear stress between fluid moving at different speeds, decelerating the faster fluid. An increase in thickness ( $\delta$ ) of the region of decelerated fluid is normally evident as the fluid flows downstream, as fluid near the edge of the boundary layer is in turn decelerated.

The simplest form of boundary layer flow is over a planar surface, shown schematically in Figure 1-1. In this case, the fluid velocity field is described in cartesian coordinates  $(x, y, z)$  as,

$$\mathbf{V} = u\hat{\mathbf{i}} + v\hat{\mathbf{j}} + w\hat{\mathbf{k}} \quad (1-2)$$

with each component given in terms of time-averaged and fluctuating components:

$$u(x, y, z, t) = \langle u \rangle(x, y, z) + u'(x, y, z, t) \quad (1-3)$$

A time-averaged quantity such as  $\langle u \rangle$  is given in terms of a sample of size  $N$  as,

$$\langle u \rangle = \frac{\sum_{i=1}^N u_i}{N} \quad (1-4)$$

Together, the time-averaged and fluctuating velocity components serve to describe the fluid flow both spatially and in time, which is relevant for unsteady or turbulent flows where the velocity might vary rapidly at a single point. A useful statistic for describing the level of



turbulence at a specific point in space is the root mean square (rms) of the fluctuating velocity component, given by:

$$u'_{rms} = \sqrt{\frac{\sum_{i=1}^N (u_i - \langle u \rangle)^2}{N}} \quad (1-5)$$

While Figure 1-1 demonstrates two-dimensional flow over a flat plate, boundary layer flows exist in the vicinity of all surfaces (liquid or solid) and need not be described in cartesian coordinates. The geometry of an engine cylinder is complex, although the airflow is generally described in cylindrical coordinates [23]. Similarly, the boundary layer flow over curved surfaces such as an aerofoil can be described in terms of cartesian coordinates or in terms of tangential, normal, and parallel components relative to the local surface.

Like all fluid flows, boundary layer flow may be laminar or turbulent. For a given set of flow conditions and geometry, the state of a boundary layer is local and depends on Reynolds number, given for a velocity  $U$  as:

$$\text{Re}_x = \frac{Ux}{\nu} \quad (1-6)$$

While a boundary layer may begin laminar, downstream it may eventually transition to turbulence (Figure 1-1b) due to the onset of instabilities [24]. In terms of laminar flow, the Blasius laminar boundary layer solution is an excellent descriptor of steady, two-dimensional (as in Figure 1-1a). It provides a simple comparative tool for evaluating whether a given boundary layer flow is laminar, transitioning, (Figure 1-1b), or turbulent (Figure 1-1c). It is presented in terms of a similarity solution to simplified versions of the mass and momentum conservation equations (Navier-Stokes equations), which is given in Appendix A.

Several integral quantities are useful for describing boundary layers based on their shape. The displacement ( $\delta^*$ ) and momentum ( $\theta$ ) thicknesses, given by:

$$\delta^* = \int_0^{\delta} \left(1 - \frac{u}{U_{\infty}}\right) dy \quad (1-7)$$

$$\theta = \int_0^{\delta} \frac{u}{U_{\infty}} \left(1 - \frac{u}{U_{\infty}}\right) dy \quad (1-8)$$

together describe a boundary layer's shape factor:

$$H = \frac{\delta^*}{\theta} \quad (1-9)$$

The shape factor is a useful way of defining the state of a boundary layer in terms of laminar and turbulent flow. For laminar flow, a boundary layer will exhibit a shape factor of approximately 2.59 (as in the Blasius solution), while turbulent boundary layers have been shown experimentally to reach shape factors of 1.4 – 1.6 [25].

### 1.4.1 Developing Duct Flow

Internal boundary layer flow within a duct may be distinguished from external flow over a flat plate by both a pressure gradient and boundary layer growth which is limited by the duct walls. For an axisymmetric duct (circular) the boundary layer growth is also symmetric towards the centreline of the duct. Similarly, for rectangular ducts boundary layer growth occurs simultaneously at each wall. The boundary layer growth is accompanied by an acceleration in the inviscid core of the flow (outside the boundary layers) with boundary layer growth due to conservation of mass. This is further complicated by the advent of transition from laminar to turbulent flow, when the initial flow is laminar, which occurs at some downstream point depending on Reynolds number, similar to flat plate flow.

The boundary layer growth is limited in that, eventually, the boundary layer edges at each wall must meet. Transition aside, once this occurs the velocity field within the duct will become invariant with axial distance, which is known as “fully developed” flow. The centreline velocity also reaches a maximum at this point, although it may overshoot its final amplitude [25] prior to settling. The length from the duct inlet to the point where the flow is fully developed is known as the entrance length ( $L_e$ ) and defines the “developing region”. The boundary layer development for laminar flow within ducts of various cross-sections has been the subject of numerous experimental [26-28] and numerical studies [29-31]. The length of the development region has similarly been the subject of numerous studies [32-34] and is known to increase with Reynolds number, since with increasing Reynolds number the rate of boundary layer growth decreases [32-34].

The behaviour of flows transitioning from laminar to turbulent, either before or after the flow becomes fully developed, is less simple to predict. Flows will remain laminar for Reynolds numbers based on the duct hydraulic diameter less than approximately 2300 [35], where the hydraulic diameter is defined as:

$$D_h = \frac{4A}{P} \quad (1-10)$$

For  $2300 \leq \text{Re}_{D_h} \leq 10,000$ , flows are transitional, meaning they may change rapidly between laminar and turbulent flow randomly [35]. At higher Reynolds numbers ( $\geq 10,000$ ), transition to turbulent flow can occur within the development region [35-37]. However, locating and quantifying the precise point at which a flow begins transition is still an open question and has been the subject of numerous experimental and analytical studies [24, 36-47]. The degree of inlet turbulence has been found to have a significant effect on where transition begins and its duration [38-43]. Changes in small disturbances in the earlier stages of transition (Tollmien-Schlichting waves) have been shown to lead to more rapid transition [24, 44, 45] in flat plate flow. A similar effect has been found in duct flow, where higher inlet turbulence intensity has been shown to move transition towards the inlet of the duct [40, 46, 47].

Internal duct flow is convenient for experimental work as the flow conditions may be tightly controlled, as in a wind tunnel test section where flow conditioning produces an initially uniform, and quiet, velocity field. Further manipulation of the flow from that point produces the desired measurement conditions. Similarly, knowledge of the boundary layer development and turbulence generation along the length of any test section is required for producing the desired boundary layer conditions, especially when the duct boundary layers themselves are the subject of experimentation. Therefore, determining the sizing for an appropriate test section, and having adequate inlet conditions, is important.

## 1.4.2 Law of the Wall

Characterizing turbulent boundary layers is useful for establishing repeatable experimental conditions. Turbulent boundary layers have been found to match a universal

velocity profile when scaled by the wall shear stress, called the “law of the wall” [48, 49]. The wall scaling is normally presented in terms of a shear velocity, given by:

$$u_\tau = \sqrt{\frac{\tau_w}{\rho}} \quad (1-11)$$

The scaling of the streamwise velocity ( $u$ ) and wall-normal ( $y$ ) distance is then given by:

$$u^+ = \frac{u}{u_\tau} \quad (1-12)$$

$$y^+ = \frac{y u_\tau}{\nu} \quad (1-13)$$

Experimental measurements of turbulent flow over flat plates has shown that turbulence intensity increases from a minimum outside the boundary layer edge to a maximum near the wall, due to the high velocity gradient present across the boundary layer. However, the turbulent fluctuations then proceed to zero at the wall, where the velocity gradient is highest. It has also been shown that the shear stress within the flow remains constant and equivalent to the wall shear stress within a similar region close to the wall. This region is named the “laminar sublayer” where the influence of turbulence disappears (e.g.  $\overline{u'v'} \rightarrow 0$ ) and the velocity profile is essentially laminar and linear in terms of wall scaling [48, 49]:

$$u^+ = y^+ \quad (1-14)$$

This region has been found to occur for  $y^+ \leq 5$ . The region within  $30 \leq y^+ \leq 200$  also tends to follow a universal profile, given by [48, 49],

$$u^+ = \frac{1}{\kappa} \ln(y^+) + B \quad (1-15)$$

over which the viscous shear stress wanes (e.g.  $\mu \partial \bar{u} / \partial y \rightarrow 0$ ). However, experimental studies disagree on an exact value for both the von Kármán constant ( $\kappa \cong 0.39 - 0.41$ ) and  $B$  ( $5 - 5.5$ ) [49]. This region is known as the “logarithmic region”, while the region for  $5 \leq y^+ \leq 30$  where both viscous and turbulent stresses are significant is known as the “buffer region”. Together they compose the “inner region”, with which experimental studies for duct flow also tend to agree [43].

### 1.4.3 Airflow Within an Engine Cylinder

As opposed to boundary layer flow over a flat plate, or within ducts, the gas phase flow within an engine cylinder is highly complex. Boundary layers which form at the cylinder liner are influenced by the three-dimensional and transient nature of the airflow, which varies cycle-to-cycle (intake through exhaust) as the piston and valves move. Due to this, experimental studies generally present the velocities and turbulence statistics in terms of the mean piston velocity ( $\bar{V}_p$ ) and crank angle ( $\Theta$ ) [23, 50, 51]. While the exact airflow behaviour is unique to each engine design and operating conditions, in general engine flows are characterized in terms of *tumble*, *swirl*, and *squish* flows [23, 50]. The charge (volume of air), which begins as jet flow from the intake valves, has a rotational character with an axis of rotation at a relative angle to the cylinder axis. During intake, tumble flow occurs when this angle is approximately  $90^\circ$ , while swirl flow occurs at  $0^\circ$ . The exact nature of this flow depends on the valve geometry and the interaction between the valve jet flow and the cylinder liner [23, 50]. Squish flow occurs during compression, where the cylinder volume decreases and the general direction of airflow is rotationally inwards (depending on piston geometry) [23, 50].

In-cylinder velocities are generally several times higher than the mean piston velocity. For example, ensemble velocities (averaged over numerous cycles) near the cylinder head (within 2 mm) exhibit velocities well within  $\pm\bar{V}_p$  ( $\bar{V}_p \approx 2.3 \text{ ms}^{-1}$ ) [23, 50]. These velocity measurements were shown to have good agreement with the law of the wall within the laminar sublayer. Farther from the cylinder head, ensemble velocities may reach values within  $\pm 4\bar{V}_p$  ( $\bar{V}_p \approx 2.8 \text{ ms}^{-1}$ ) [51]. However, measurements near the cylinder liner of ensemble tangential velocities at half the clearance height were found to reach between  $4\bar{V}_p - 6\bar{V}_p$  ( $\bar{V}_p \approx 4.6 \text{ ms}^{-1}$ ) at 90% of the bore radius (4 mm from the liner), tapering to zero at the cylinder axis and reaching zero at the cylinder liner [52]. The clearance height is between the piston top and cylinder head once the piston reaches top dead centre (TDC), where TDC is the position of the piston when it is highest in the cylinder. TDC is therefore also when the piston is farthest from the crankshaft, at the end of an upwards stroke. The turbulence intensities near the wall were found to reach between  $0.2\bar{V}_p - 0.4\bar{V}_p$  in the same region (10% of the maximum) [52].

## 1.5 Lubricant Films on the Cylinder Liner

Lubrication via engine oil reduces the friction between the piston rings and the cylinder liner. In the process, a film of oil is deposited on the cylinder surface as the compression ring (top ring) sweeps along it from top to bottom dead centre. A minimum oil film thickness ( $h_{min}$ ) is present between the top ring and the liner, and is ultimately responsible for controlling the thickness of the deposited film,  $h$  [53]. The minimum oil film thickness is also directly related to the frictional forces acting between the piston and liner, and is therefore critical to engine performance [3, 54, 55]. The geometry of each ring, the circumferential difference in ring pressure (between the thrust and anti-thrust sides of the piston), and varying engine conditions each have an impact on the oil available stroke-to-stroke at the top ring, and results in an oil film of nonuniform thickness [53, 56, 57]. The oil film thickness is relevant to its evaporation because of the fundamental impact on mass diffusion through the liquid to the surface where evaporation occurs [19, 35]. The height of the film also affects the relative scale of waves at its surface under shear flow, which may significantly impact the boundary layer flows above it [58, 59].

Measurements of  $h$  or  $h_{min}$  are accomplished in-situ by means of capacitance [60, 61] and ultrasonic [3, 55] sensors which incorporate the piston rings (measuring  $h_{min}$ ) or optical measurements through the cylinder liner leveraging laser fluorescence [54, 56]. Measurements by Furuhashi et al. [60] via top ring capacitance sensors give a range of  $h_{min} \leq 8 \mu\text{m}$  for a 139.7 mm  $\times$  152.4 mm (bore  $\times$  stroke) cylinder. Similarly, measurements using local capacitance sensors by Söchtig and Sherrington [61] yielded  $h_{min} \leq 10 \mu\text{m}$  for a 95 mm  $\times$  127 mm cylinder. However, measurements by ultrasonic sensors in an experimental rig simulating the contact between the liner and piston rings for various loads found a lower limit of  $h_{min} \leq 3 \mu\text{m}$  [3, 55]. In addition, laser fluorescence measurements by Dearlove and Cheng [54] in a similar reciprocating test rig found  $h_{min} \leq 3 \mu\text{m}$  for various engine speeds and loads. Similar measurements at an elevated liner temperature (80°C versus 30°C) by Takiguchi et al. [56] determined  $h_{min} \leq 2 \mu\text{m}$  at both the thrust and anti-thrust sides of the piston, with a resulting  $h < 1 \mu\text{m}$  after each stroke. These measurements serve more as typical values than deterministic ones due to the variability in lubricants, part geometries, conditions, and measurement techniques.

Models which directly model the heat transfer and oil film dynamics between the piston ring and cylinder liner provide values for both the oil film temperature and thickness. For example, Harigaya et al. reported values of  $h \leq 12 \mu\text{m}$  depending on temperature and lubricant viscosities [53, 57] for liner temperatures between  $80^\circ\text{C} < T_s < 120^\circ\text{C}$  depending on engine speed and decreasing with distance from TDC. Markedly higher values for  $h$  ( $5 \mu\text{m} < h < 22.5 \mu\text{m}$ ) were calculated at low film temperatures ( $T_s = 30^\circ\text{C}$ ) [57], which emphasizes its importance to the rheological performance of the oil aside from its importance to evaporation. The cylinder liner temperature cover a large range, with a familiar variation with engine design and operating conditions. Direct measurements of the cylinder liner temperature provides a range of  $90^\circ\text{C} < T_s < 200^\circ\text{C}$  [5, 18, 60] with calculated values from liner film evaporation models falling within the same range.

## 1.6 Scope and Outline of Thesis

The focus of the present work is to establish the evaporation rates of a common engine lubricant (5W-30) under engine-like conditions, and in a form similar to that of a wall-film found on a cylinder liner. The evaporation of the lubricant is studied as a thin film under various boundary layer conditions at an elevated temperature ( $150^\circ\text{C}$ ). In particular, the bulk velocity of the flow is varied while the shape of the boundary layer is controlled. The effect of near-wall turbulence is also explored by varying the turbulence intensity within the boundary layer. The required gas flow is generated through use of a wind tunnel designed for this study. The evaporation measurements are conducted within the test section of the wind tunnel, where the geometry of the test section is adjusted in order to produce the varying boundary layer conditions. The gas flow conditions are validated through the use of particle image velocimetry and hot-wire velocimetry measurements.

The following are the objectives of the work presented in this thesis:

- i. To validate the flow conditions through the use of PIV and hot-wire measurements.
- ii. To study the effect of gas velocity and boundary layer shape on the evaporation of a discrete thin liquid film of engine lubricant at an elevated temperature.

iii. To study the effect of near-wall turbulence on the evaporation of the same.

Chapter 1 of this thesis has established the context for the evaporation of thin liquid oil films, including: the impact of oil consumption on engine emissions; the relative contribution of wall-film evaporation to oil consumption; typical engine conditions; and the generation of the film at the cylinder liner. Chapter 2 will present a review of literature relating to the evaporation of hydrocarbon liquids, including the evaporation of bulk volatile liquids under atmospheric conditions and the implications of direct modelling of the wall-film. Chapter 3 discusses the validation of the wind tunnel and channel flow, which includes the validation of the flow within the evaporation test section (incident upon the film). Chapter 4 explores the evaporation results. Finally, Chapters 5 and 6 will discuss the conclusions drawn from this study, and recommendations for any future work, respectively.

Several appendices are also included which contain additional relevant material. Appendix A provides an overview of the Blasius laminar boundary layer solution for flow over a flat plate. Appendix B shows technical drawings detailing the geometry of the designed wind tunnel flow conditioner. Lastly, Appendix C compiles the full results of the PIV measurements within the evaporation test section described in Chapter 3



## 2 Literature Review

The following section contains details of the literature reviewed with respect to the evaporation of engine lubricant films under airflow. This includes a review of experimental studies for both the evaporation of volatile, liquid species under turbulent boundary layers and the behaviour of liquid films in two-phase flow, both of which are relevant to the evaporation of engine liner films. Experimental studies relating to the evaporation of multi-component hydrocarbon mixtures are also reviewed, which differ in behaviour compared to single component substances. Finally, modelling studies of the evaporation of cylinder wall films are reviewed, which are generally informed by both experimental and nominal engine conditions.

### 2.1 Evaporation under Boundary Layer Flow

The evaporation of single species liquids in air, including pure hydrocarbons, is a relatively simple phenomena limited by diffusion above the liquid surface. In general, mass transfer is governed by a concentration gradient present above the liquid. This process is in turn affected by convection, which in boundary layer flow (forced convection) acts to increase the concentration gradient by carrying vaporized species downstream; in this way, a mass or concentration boundary layer forms [19, 35]. In 1983, J. Schröppel and F. Thiele [62] provided an excellent example of the familiar, fundamental problem of boundary layer flow over a wetted flat plate, calculating the momentum, mass, and temperature boundary layers numerically. In contrast with forced convection, under natural convection – where the inertial movement of the fluid is governed by buoyancy – the evaporation rates for pure hydrocarbon liquids are well-defined by one-dimensional diffusion models, as in a 2009 study by P. L. Kelly-Zion et al. [19, 63].

Among the first experimental considerations of this model problem was conducted by F. Pasquill [64] in 1943 to extend the theory proposed earlier by O. G. Sutton [65]. In 1934, Sutton [65] proposed an evaporation model from free liquid surfaces of discrete length under turbulent boundary layers based on vapour transport through momentum transfer. Pasquill [64] extended Sutton's theory by introducing molecular diffusivity as opposed to purely the

mechanical action of eddies. This provided a revised theory with much better agreement to Pasquill's wind tunnel evaporation measurements, and explained the disparity between previous measurements for different pure substances where no consideration was given to the aerodynamics [64]. For a given pure substance, it was shown that evaporation rate increases with increasing mean air velocity. A 1952 study by Davies and Walters [66] further extended Pasquill's experiments further for longer aspect ratio plane areas, and showed good agreement with Pasquill and Sutton's two-dimensional solution [64, 65]. In 1997, C. H. Huang [67] provided an overview of the Pasquill-Sutton theory's applicability, showing that the evaporation in these problems is dependent on the  $-2/3$  power of the Schmidt number as opposed to simply the kinematic viscosity,  $\nu$  or molecular diffusivity,  $D$ :

$$\text{Sc} = \frac{\nu}{D} \quad (2-1)$$

Pasquill [64] alluded to this dependence on both the molecular diffusivities and viscosity, although the molecular diffusivity was considered dominant. This is a well known result, as correlations for mass transfer coefficients, or the Sherwood number (Sh), for convective mass transfer are known to follow Sc and Re, similar to how Nusselt number (Nu) correlations with the Prandtl number (Pr) instead of Sc [19]. However, Huang [67] also suggests a model which accounts for an "interfacial sublayer" (i.e. the viscous sublayer), where there exists a linear velocity profile directly above the liquid surface and molecular diffusivity dominates.

While the evaporation rate dependence on the vapour's molecular diffusivity and the mean air velocity was shown by Pasquill [64], the notion that the evaporation rate depends more fully on molecular diffusion within the laminar region as suggested by Huang [67] was also explored by R. Reijnhart et al. [68]. In 1980, Reijnhart et al. [68] presented a theoretical approach to modelling free surface evaporation under smooth boundary layers. The simplified, two-dimensional model for the vapour concentration,  $c_i$ , was given as:

$$\langle u \rangle \frac{\partial \langle c_i \rangle}{\partial x} = \frac{\partial}{\partial y} \left\{ \left( D_m + D_{t,y} \right) \frac{\partial \langle c_i \rangle}{\partial y} \right\} \quad (2-2)$$

$$D_m = \begin{cases} \frac{\nu_m}{\text{Sc}_m} & \text{if } y \leq y_{vt} \\ 0 & \text{if } y > y_{vt} \end{cases} \quad (2-3)$$

$$D_{t,y} = \begin{cases} 0 & \text{if } y \leq y_{vt} \\ u_\tau \kappa y & \text{if } y > y_{vt} \end{cases} \quad (2-4)$$

where  $D_m$  is the molecular diffusivity and  $D_{t,y}$  is the turbulent diffusivity normal to the surface. Furthermore, the velocity profiles for the smooth boundary layer case were given as,

$$\langle u \rangle = \begin{cases} \frac{u_\tau^2 y}{\nu} & \text{if } y \leq y_{vt} \\ \frac{u_\tau}{\kappa} \ln \left( \frac{u_\tau y}{\nu} \right) + 5.1 u_\tau & \text{if } y > y_{vt} \end{cases} \quad (2-5)$$

which is equivalent to equations (1-13) and (1-14) given in §1.4.2 where the viscous sublayer extends to a height  $y_{vt}$  and the buffer region is neglected. The goal of Reijnhart et al. [68] was to provide an improved model for where the wall prior to the liquid leading edge has significant roughness ( $y_0$ ). Future experimental measurements by R. Reijnhart and R. Rose [69] meant to verify the applicability of the previous model [68] showed that the roughness transition cannot be neglected, as artificially higher evaporation rates for a given shear velocity result. In addition, where the evaporation rate was found to be lower with increasing roughness, while neglecting the transition yields the opposite trend. However, excellent agreement to the smooth boundary layer model was found in a smooth wall case ( $y_0 \approx 22 \mu\text{m}$  for a  $25 \times 25 \times 5 \text{ cm}$  pool), which implied that the evaporation was governed significantly by molecular diffusion in the laminar sublayer, near the gas-fluid interface. In each case, evaporation rate was shown to increase with increasing  $u_\tau$ , and also to increase rapidly as the liquid temperature approached its boiling point and the interfacial vapour pressure increased [69].

While the above studies generally considered plane (or smooth) liquid surfaces, in reality surface waves form on a liquid pool or film under shear from turbulent boundary layer flow. The wavy nature of liquid films along a flat plate under turbulent flow was investigated by S. Wittig et al. in 1992 [58]. The goal of Wittig et al. [58] was to model the heat, mass and momentum transfer of the two-phase flow within pre-filming airblast atomizers, which was modelled and experimentally verified using water flow along a flat-plate ( $60 \text{ mm} \times 340 \text{ mm}$ ) within a duct (wide  $60 \text{ mm} \times 4 \text{ mm}$ ) at environmental temperatures ( $T_g \leq 40^\circ\text{C}$ ), high gas phase velocities ( $U \leq 120 \text{ ms}^{-1}$ ), and low film volume fluxes per unit breadth,  $B$  ( $\dot{V}_f/B \leq 1 \text{ cm}^2\text{s}^{-1}$ ). When laminar liquid flow was assumed the model matched experimental data well under fully

developed turbulent flow, resulting in low average film surface velocities ( $\langle u_f \rangle < 2 \text{ ms}^{-1}$ ) and average film thicknesses ( $\langle h_f \rangle$ ) less than 150  $\mu\text{m}$ , depending on gas phase Reynolds number. Wittig et al. [58] posited that the film remains laminar for the velocity ranges studied, and that the waviness of the film surface does not increase the turbulence levels of the gas phase flow.

The laminar nature of the liquid phase flow was tested in 1994 by Himmelsbach et al. [59], which extended the previous study by Wittig et al. [58] with the same apparatus for higher gas temperatures. Himmelsbach et al. determined similar behaviour, where the film flow was predominantly laminar. Interestingly, this was despite the average film height being larger than the laminar sublayer for most liquid flow rates [59]. However, in both studies the laminar nature of the film was questionable at higher  $\dot{V}_f/B$ , and it was observed that for those measurements the film became unstable, meaning droplets begin to tear from the film surface [58, 59]. This occurred for Reynolds numbers based on the local film height within  $\text{Re}_f = \langle u_f \rangle \langle h_f \rangle / \nu_f \approx 200 - 250$ .

## 2.2 Multicomponent Mixture Evaporation

The evaporation of multi-component hydrocarbon mixtures is significantly more complex than for pure substances. For pure liquids, the equilibrium vapour mole fraction at the liquid-air interface is governed by its vapour pressure at a given temperature [19, 35]. However, for multi-component mixtures each species is evaporating simultaneously while their vapour pressures ( $p_i$ ) depend directly on the mole fraction ( $x_i = n_i/n_{tot}$ ) of each species in solution, as in Raoult's Law for ideal liquid mixtures:

$$p_i = x_i p_i^* \quad (2-6)$$

where  $p_i^*$  is the vapour pressure for the  $i^{\text{th}}$  pure species. While the mixture may be initially homogenous, each species may have different rates of evaporation, depending on their initial proportions and  $p_i^*$ . Consequently, the concentrations of each species at the interface will vary with the progress of evaporation, leading to concentration gradients within the liquid phase and finally transport of species to the surface via diffusion (in the case where the liquid is static) [19]. The resulting variation in evaporation rate (of each species) with time was demonstrated

effectively by Okamoto et al. [70] for several hydrocarbon mixtures with two, three, and five components. In 2010, Okamoto et al. [70] determined that the varying vapour pressures and evaporation rates of each mixture were predicted well by a model based on Raoult's law with activity coefficients, which account molecular interactions in the liquid phase which leads to non-ideal behaviour. The evaporated mass for the five-component mixture increased logarithmically with time, while the overall evaporation rate was exponentially decreasing; similar behaviour was demonstrated by each other mixture [70]. The evaporation rates in each case increased with temperature [70], primarily due to the increase in vapour pressure with temperature. This was demonstrated in an earlier study by Okamoto et al. [71] in 2009 for gasoline, in a similar study where the evaporation rate of gasoline was shown to also decrease exponentially with weight loss fraction [71].

The evaporation of multicomponent hydrocarbons has also been studied under convective mass transfer conditions. Specifically, several studies focus on establishing evaporation behaviour under environmental conditions, meaning moderate gas phase velocities and temperatures. In 1973, Mackay and Matsugu [72] provided an evaporation model for shallow pools (19 mm) based on a mass transfer coefficient calibrated by the evaporation of water and cumene. The resulting correlation was given in terms of bulk velocity, pool size, and Schmidt number. The evaporation of gasoline was also considered, each under the same simplified, atmospheric velocity conditions given by:

$$\langle u \rangle = U_1 y^{\frac{n}{2-n}} \quad (2-7)$$

with  $U_1$  being the velocity at 1 m of height and  $n = 0.25 - 1.0$ , where  $n = 0.25$  yields the 1/7 power law profile for fully developed turbulent pipe flow. The evaporation rate of the mixtures was found highly dependent on "liquid mass transfer resistance" (diffusion) and the species vapour pressures, consistent with the work of Okamoto et al. [70]. Mackay and Matsugu [72] also posited that the higher evaporation rates relative to flat plate correlations is due to waves at the liquid surface [58, 59], where their correlation predicted evaporation similar to smooth flat plate correlations under turbulent flow.

An additional study by M. Gerendas and S. Wittig [73] in 2001 further explored the behaviour of a multi-component mixture of ethanol and water (for 1:0, 1:1, 1:4, and 1:3 mass

ratios, respectively) in the same apparatus for an elevated gas temperature ( $T_g = 200^\circ\text{C}$ ). In this case the film thickness decreased markedly with axial distance due to evaporation (for each  $\dot{V}_f/B$  case). While “partially turbulent” velocity profiles were required to match the experimental results for higher film thicknesses, a laminar profile ( $u^+ = y^+$ ) was sufficient at lower film thicknesses (unspecified). Also, for the same gas phase velocity, cases with higher  $\dot{V}_f/B$  maintained nearer the initial concentration of ethanol over the length of the plate. This implies that for the cases where the film thickness decreased rapidly the ethanol evaporated in higher proportion than water, indicating an expected lower resistance to the more volatile component’s diffusion [19]. Additionally, a reduced concentration gradient of ethanol in the gas phase was observed for an elevated pressure ( $p_o = 260$  kPa versus 110 kPa). In each of the above studies by S. Wittig [58, 59, 73] the inlet turbulence intensity of the fully developed turbulent flow was measured to be 5% (centreline location assumed).

In 1997, M. Fingas [74, 75] conducted experimental evaporation studies for numerous hydrocarbon mixtures at low temperatures ( $21 - 25^\circ\text{C}$ ), stagnant gas or low bulk airflow conditions ( $0 - 2.5$  m/s), and large pool sizes. Logarithmic or hyperbolic evaporation behaviour was observed, roughly depending on the number of major species; as the concentrations of more volatile species depleted, the overall evaporation rate dropped. Higher rates of evaporation were observed under airflow while differing little with velocity [74, 75]. This led to the conclusion that the evaporation was not boundary layer regulated [74, 75]. Boundary regulation is where the downstream evaporation would be limited by the increasing mass fraction of hydrocarbons at the liquid-gas interface. Fingas [74-76] posited that boundary layer regulated evaporation would increase with air velocity and turbulence, while non-regulated flows would be reasonable for high vapour pressures (low temperatures). In 2004, Fingas [76] presented empirical models with respect to temperature and time for the evaporation of many hydrocarbon mixtures (oils) based on previous results [68, 69] each demonstrating logarithmic or square root behaviour. As expected, the evaporated mass was shown to increase with temperature, although the experimental temperature range was low ( $T \leq 60^\circ\text{C}$ ).

## 2.3 Cylinder Liner Evaporation Modelling

The evaporation of engine oil from the cylinder liner has been the subject of several modelling studies. Modelling is a useful tool for studying an otherwise complex problem; the liner evaporation process incorporates not only a vaporizing multicomponent film under shear flow but also the transient behaviours of engine temperature, pressure, airflow, and oil film generation. Each study [5, 20, 77-80] generally includes some empirical formulae or experimental engine data to simplify or verify the modelling process. Simplified cylinder geometry is also used, although wall film sub-models are employed as part of numerical engine simulation codes such as KIVA [81, 82].

The convective mass transfer from the liquid phase is predominantly solved one-dimensionally through a heat and mass balance at the liquid-gas interface. In 1992, S. Wahiduzzaman et al. [83] proposed a one-dimensional method whereby a mass boundary layer thickness ( $\delta_d$ ) is calculated based on a heat-mass transfer analogy ( $Sc = (\delta/\delta_d)^3 = 2.5$ ). This length is then used in a solution to the diffusion equation [19], given as:

$$\dot{m} = \frac{D\rho_g}{\delta_d} \log \left( 1 + \frac{Y_s - Y_\infty}{1 - Y_s} \right) \quad (2-8)$$

The temperatures and pressures required to calculate the thermodynamic properties for each species were then determined via a one-dimensional heat transfer model based on a separate engine simulation code for the gas phase velocity, temperature, and heat flux to the liner. A separate “ring pack” simulation code was used to provide the film thickness distribution in conjunction with an engine simulation code, allowing computation for each part of the engine cycle along an axial discretization of the liner. A similar procedure was employed by Audette and Wong [79, 80] in 1999, again using an external engine simulation code and film thickness distribution model. Distillation curves for two 15W40 oils were used to determine the virtual distribution of n-paraffins composing the modelled liquid. A Sherwood number correlation was used to calculate the relevant mass transfer parameters of the form:

$$Sh = \frac{g_m L}{\rho D} = 0.035 Re^{0.8} Sc^{0.667} \quad (2-9)$$

where  $g_m$  is the mass convection coefficient ( $\text{kg m}^{-2} \text{s}^{-1}$ ).

In 1997, De Petris et al. [78] presented an approach similar to Wahiduzzaman et al. [83], yet limited to single component liquid films ( $\text{C}_{24}\text{H}_{50}$ ,  $\text{C}_{27}\text{H}_{56}$ ,  $\text{C}_{30}\text{H}_{62}$ ). In relatively simplistic approach, an instantaneous convective heat transfer coefficient ( $h$ ) at the liquid-gas interface was provided by a correlation given by G. Woschini [77] in 1967. Woschini’s correlation, which empirically includes radiative heat transfer, is given by:

$$h(\Theta) = 3.26B_e^{-0.2} p_e(\Theta)^{0.8} T_g(\Theta)^{-0.55} w_e(\Theta)^{0.8} \quad (2-10)$$

where  $p_e$  is the in-cylinder gas pressure and  $w_e$  is the average cylinder gas velocity. Both  $p_e$  and  $T_g$  are provided by De Petris et al. [78] with respect to crank angle ( $\Theta$ ), while  $w_e$  is an empirical function. In 2009, Harigaya et al. [20] performed another study on the evaporation of single-component hydrocarbons using a model which employed both Woschini’s [77] correlation and experimentally measured engine conditions. In addition, the model’s predictions were verified by measured oil consumption data. A “thermal-hydrodynamic lubrication model” [53, 57] was subsequently used to calculate the oil film thickness based on the model results. In 2017, Soejima et al. [5] extended Harigaya et al.’s [20] model to include multi-component liquid films. Measured oil consumption and engine condition data for a supercharged diesel engine was used to inform the model. The model was implemented for films composed of a distribution of n-paraffins estimated by comparing vapour pressures measured for test oils (SAE 10W30, SAE 30) with vapour pressure-temperature correlations for  $\text{C}_n\text{H}_{n+2}$  [5].

Each model agreed that the oil film evaporation rate depended strongly on the film temperature and oil composition, and weakly on the oil film thickness due to the time scale of each cycle [5, 20, 77-79, 83]. Soejima et al. [5] also conclude that evaporation rates decrease with increasing cylinder pressure, due to the phenomenon’s reliance on vapour pressure. Similarly, each model agreed that evaporative losses are highest during the intake stroke and lowest during the expansion stroke due to the elevated pressure [5, 20, 77-79, 83].

The evaporation of wall films is also considered by sub-models which model spray-wall interactions and film dynamics as part of numerical engine simulations, such as KIVA [81]. Modified wall functions are used to model the interaction between the vaporizing film and the



boundary layer flow, as part of modelling the near-wall region during simulation. O'Rourke and Amsden [81] employ a mass vaporization term as part of source terms in the gas phase conservation, momentum, and energy equations. This vaporization term incorporates separate functions for the laminar and turbulent regions within the boundary layer. Foucart et al. [82] use a similar method in their model which only considers evaporation with respect to a conservation source term. As opposed to O'Rourke and Amsden [81], Foucart et al. [82] do not consider turbulent kinetic energy or a turbulent Schmidt number. Instead, two source terms are employed depending on whether inertial or thermal effects are dominating mass transfer.

## 2.5 Gap In Literature

Studies which experimentally measure the evaporation of hydrocarbon mixtures under boundary layer conditions frequently do not include a rigorous description of their airflow conditions. Additionally, measurements do not consider boundary layer velocities similar in order of magnitude to those in-cylinder during typical engine operating conditions (§1.5.3). The effect of turbulence is also typically restricted to fully developed turbulent flow, or in modelling heat-mass transfer analogies. In realistic cylinder flow, turbulence is present in thin boundary layers near the liner [52], with turbulence generated by a combination of liner boundary layer generation and via the intake valve jet flows [23]. Since the mass transfer is predominantly controlled by the nature of these boundary layer flows, providing experimental measurements of the oil species evaporation for similar length scales and at an elevated temperature is valuable.

## 2.6 Approach

Evaporation of engine lubricant from a liquid film at the cylinder liner is synonymous with, if not equivalent to, evaporation from a plane liquid surface under boundary layer flow. In each case a free liquid surface is present beneath a boundary layer while the transport of the evaporating species is theoretically encouraged by any turbulence present within the concentration (mass) boundary layer, if it is of sufficient thickness [19]. Therefore, the film

evaporation rates can be characterized by subjecting discrete samples of oil to boundary layer flows for specific durations.

Based on the foregoing literature analysis the purpose of this study is therefore to determine the relative importance of boundary layer shape, near-wall turbulence intensity, and Reynolds number on the evaporation of discrete film samples. To fulfill this purpose the evaporation of lubricant films of a known initial thickness and temperature are measured after exposure to laminar and turbulent boundary layers with varying velocity and turbulence intensities. Evaporation measurements from liquid samples using an analytical microbalance under steady flow [68, 69] and for discrete samples [63, 70, 71, 74-76] have been successful. Since a microbalance was available, this gravimetric measurement technique was chosen. While cylinder film thicknesses are generally less than 10  $\mu\text{m}$  (§1.5) initial film thicknesses of 50  $\mu\text{m}$  were chosen to improve measurement accuracy. Finally, a constant oil temperature typical of liner temperatures near TDC was chosen for all experiments, where evaporation and cylinder temperatures are highest [81, 83].

It was decided that the evaporation measurements should be performed within a wind tunnel, which lends itself to the study of discrete liquid samples under boundary layer flow (§1.4.1). This necessitated designing, building, and validating an appropriate flow conditioner and test section, which is detailed in the following section along with the accompanying PIV and hot-wire analysis. Within the test section, a shallow ( $< 0.5$  mm) inset in a copper plate was chosen to hold the oil film samples. As Reijnhart and Rose [69] observed that change in evaporation rate with pool height (relative to vessel edge) was near negligible, this was considered reasonable. Despite the 50  $\mu\text{m}$  film samples being subjected to relatively high velocities, it was assumed that there would be no droplet tear-off from the film surface waves based on the expected film Reynolds number [58, 59]; no film instability was observed during the experiments.

# 3 Boundary Layer Measurements

The purpose of this work is to investigate the evaporation of thin lubricant films under various boundary layer flows, and particularly with varying levels of near-wall turbulence. Generating appropriate boundary layer flows was therefore necessary prior to conducting the evaporation measurements. A wind tunnel was designed and built for this purpose, including a flow conditioner and an extended channel (the test section). Hot-wire anemometry (hot-wire) was used to judge the performance of the wind tunnel for a range of applicable Reynolds numbers. The turbulence generated by a number of wire meshes placed at the inlet of the test section was also measured using hot-wire, to determine how the turbulence intensity might be controlled within the duct. PIV was then used to ascertain the development of the velocity and turbulence fields along the entire length of the duct at the plane of symmetry. An additional test section for holding and heating liquid film samples was also designed and built (evaporation test section). After post-processing the initial PIV results, two axial lengths within the duct were chosen which provide an acceptable range of boundary layer conditions. A second set of PIV measurements was taken at both locations to validate the flow field within the evaporation test section for the chosen range of Reynolds numbers and inlet conditions. Multiple planes were measured within the duct, from two directions, in order to measure each velocity component. These procedures are detailed further in the following sections.

## 3.1 Wind Tunnel Design

Traditionally, measurements within a wind tunnel test section are conducted within the inviscid region of the flow produced by the conditioner, meaning outside the boundary layer region where velocity gradients are present. This provides a predictable and uniform flow for many experiments. However, the boundary layers considered in this study are generated along the walls of the test section duct, with the intent that the lower wall of the duct will accommodate the liquid film surface coplanar with the lower wall. This is primarily due to space constraints; a long duct length is required to produce developing boundary layers and observe the generation and decay of inlet turbulence. Due to space constraints, and to match

preexisting apparatus, the test section cross section was chosen to be  $20 \times 40 \text{ mm}^2$ . This corresponds to a rectangular cross section with  $D_h = 26.67 \text{ mm}$ . For the initial flow validation, a duct length of  $37.5D_h$  was chosen to accommodate development length required for “fully developed” turbulent duct flow [19].

The goal of most wind tunnels is to deliver uniform flow to the inlet of the test section, both spatially and in time (minimum turbulence intensity). A flow conditioner is used to accomplish this, in that it attempts to remove any swirl and non-uniformity from the flow. The secondary purpose of the flow conditioner is to link the geometry of the flow from the air source to that of the test section. For this study a preinstalled centrifugal blower (APPL RB80-4BU) was employed as the air source, connected via a round hose ( $L = 3 \text{ m}$ ) from a separate room within the lab. The maximum bulk airflow to be delivered to the test section was defined as  $50 \text{ ms}^{-1}$  ( $\text{Re}_{D_h} = 89,000$ ) based on requirements separate from this study.

The requirements listed above lend themselves to an open-circuit tunnel, due to the length of the test section, space considerations, and cost [84, 85]. Flow conditioners for tunnels of this type are generally composed of some common components: a contraction; a settling chamber; and a diffuser or transition to accommodate the air source geometry. A contraction is used to increase the velocity of the flow to the desired velocity at the test section, which limits losses within the contraction. It is also a primary contributor to turbulence reduction and flow uniformity at the test section. The honeycomb and screens found within the settling chamber serve a similar purpose, with the primary purpose of the former being swirl reduction and the latter being reduction of non-uniformities. In this case, both a transition and diffuser were required to connect the air supply to the settling chamber. The settling chamber geometry and dimensions are set by the chosen contraction ratio and test section geometry, which both differed from the blower/hose outlet. Finally, the number, placement and dimensions of the honeycomb and screens is determined by the required amount of attenuation, and must perform robustly across the operating Reynolds number range. Drawings of the final wind tunnel components can be found in Appendix B, while an overall layout is shown in Figure 3-1.

The contraction ratio,  $C$ , was chosen to be 9 based on recommendations by Mehta [86] and Mehta and Bradshaw [84]. Large values of  $c$  are advantageous, as lower speeds within the settling chamber improves the pressure drop across the screens/honeycomb and lowers the

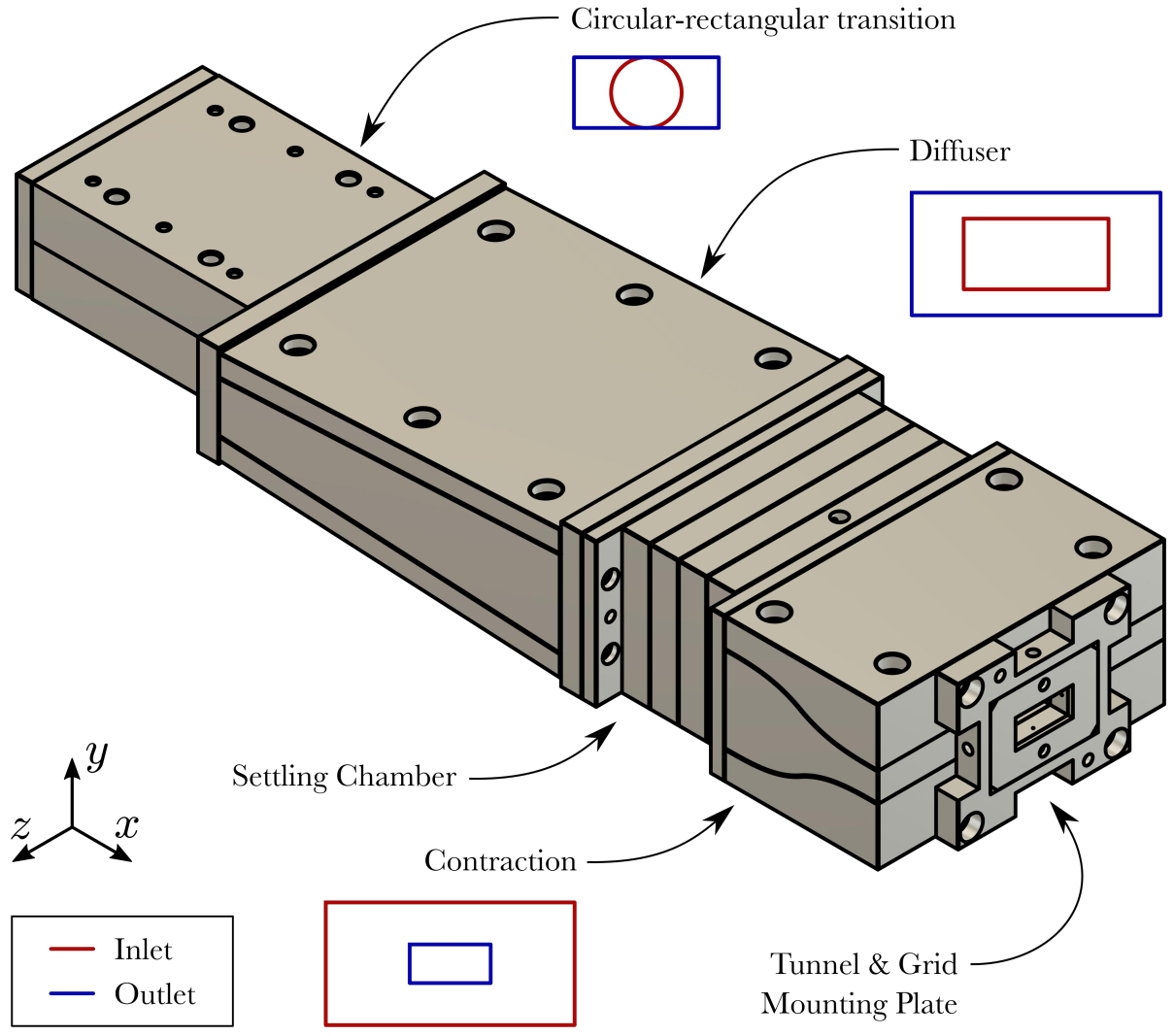


**Figure 3-1. Overall layout of the flow conditioner, including major changes between inlet and outlet cross-sections for different components.**

Reynolds number based on the wire diameter,  $Re_d$ , which is important to the design of the settling chamber. Additionally, with high  $C$  the contraction will be more tolerant of “irregularities” at its entrance due to the high acceleration [87]. However, a larger ratio also increases the length of the contraction required to avoid separation at the exit, increasing size and cost, although due to the scale of the equipment this was considered to be a negligible concern as most of the cost was associated with fabrication.

Due to the relatively high aspect ratio of the tunnel, three-dimensional geometry was chosen for the contraction. A two-dimensional contraction, with plane walls along one dimension, produces a very high aspect ratio settling chamber for large values of  $C$ . A high

aspect ratio settling chamber is problematic when designing the settling chamber, due to both boundary layer growth affecting uniformity and the required mesh wire diameters. The length of a two-dimensional contraction will also need to be excessively longer for the same performance, since it is only expanding in one plane. Morel [87, 88] suggests similar design techniques for axisymmetric and two-dimensional contractions which aim to produce wall geometries with minimum contraction length and exit boundary layer thickness while avoiding separation and ensuring flow uniformity in the test section. The guidelines in Morel's work produces wall geometries based on simple matched cubic curves. In both studies [87, 88] Morel concludes that while the design procedures cannot account for the complexities of the flow in three-dimensional, rectangular nozzles (with all four walls curved), the design of an axisymmetric contraction provides a good first estimate of the average conditions for an equivalent diameter given by  $D_{eq} = 2\sqrt{A_1/\pi}$  if the aspect ratio is not too high (unspecified) [87]. This is supported by a brief study of a rectangular nozzle of aspect ratio 1 which was designed using Morel's axisymmetric method, where the design wall pressure coefficient was reduced to account for the expected high pressure gradients in the corners [88]. Deviation from the design pressure coefficient was measured at the wall centreline along with variation from the centreline to the corners, as expected [88]. A region of constant pressure along the corners indicated some separation was occurring, but Morel comments that the effect is likely restricted to small bubbles at the corners; no low frequency fluctuations or non-uniformities were evident in the test section. Consequently, the design of the contraction was conducted using Morel's axisymmetric guidelines as a first estimate [87].

Yao-xi Su's [89] numerical, potential flow simulations of three-dimensional contractions further informed the design of the contraction. The flow analysis was conducted for a number of geometries, varying the inlet and exit aspect ratios, match-point, length, contraction ratio, and contour power factor. Each geometry was compared on the basis of inlet and exit flow uniformity (maximum variation), pressure coefficients, and crossflow amplitude (relative difference between the corner and wall velocities). As in Morel's guidelines [87, 88], increasing contraction ratio was found to improve exit uniformity. Similarly, increasing length was found to improve performance. Also, the contour match-point was found to be the parameter most

important in optimization due to an opposite effect on inlet and outlet performance (wall pressure coefficients), which is the case in Morel's work [87].

Importantly, the affect of test section aspect ratio has limited affect on exit uniformity and pressure coefficients, where the inlet (settling chamber) and exit (test section) aspect ratios are the same [89]. The major affect of increasing aspect ratio was shown to be an increase in Su's [89] crossflow parameter. An increase in the exit pressure coefficient was also evident, which is detrimental to performance as it increases the risk of separation. Concurrently, a considerable difference in crossflow was shown for contractions with different inlet and exit aspect ratios, with the best performance found for contractions where both ratios are 1. A small improvement to the exit pressure coefficient and flow uniformity at the inlet and exit was demonstrated for an inlet ratio of 1 and a narrow exit ( $\sim 2.5$ ). However, results were not presented exhaustively for this case (or the exit ratio 2 case), so the aspect ratio of the contraction was chosen to be constant between the inlet and exit.

The final length of the contraction was increased by 25% from the results of these axisymmetric calculations. This is based on a recommendation from Su [89], where it is noted that an increase of 20 – 25% is necessary to ensure similar pressure coefficients and uniformity compared to axisymmetric contractions. The increase of 25% was chosen due to the overall positive effect of increasing the contraction length. The final geometry is shown in Figure 3-2 along with the relevant parameters from Morel's procedure. The final length of the contraction was  $L = 107$  mm, with  $A_2 = 20 \times 40 = 800$  mm<sup>2</sup> and  $A_1 = 60 \times 120 = 7200$  mm<sup>2</sup>. The final cubic match point was calculated to be  $x_m = 52.89$  mm.

The chosen contraction ratio sets the cross-section dimensions for the settling chamber at 60 mm  $\times$  120 mm. The goal of the settling chamber is to make the incoming flow more uniform. The turbulence intensity of the flow should also be reduced [84], although the contraction accomplishes both goals [84]. The composition of the settling chamber is generally a segment of honeycomb followed by a series of mesh screens. The screens within the settling chamber serve to make the flow more uniform, as higher velocities are locally damped more than slower velocities as they flow over the mesh. A "honeycomb" in this case is composed of many cells aligned in the same direction and joined together into a sheet. The cells normally have the same cross-sectional shape, often hexagonal, and with a length several times their

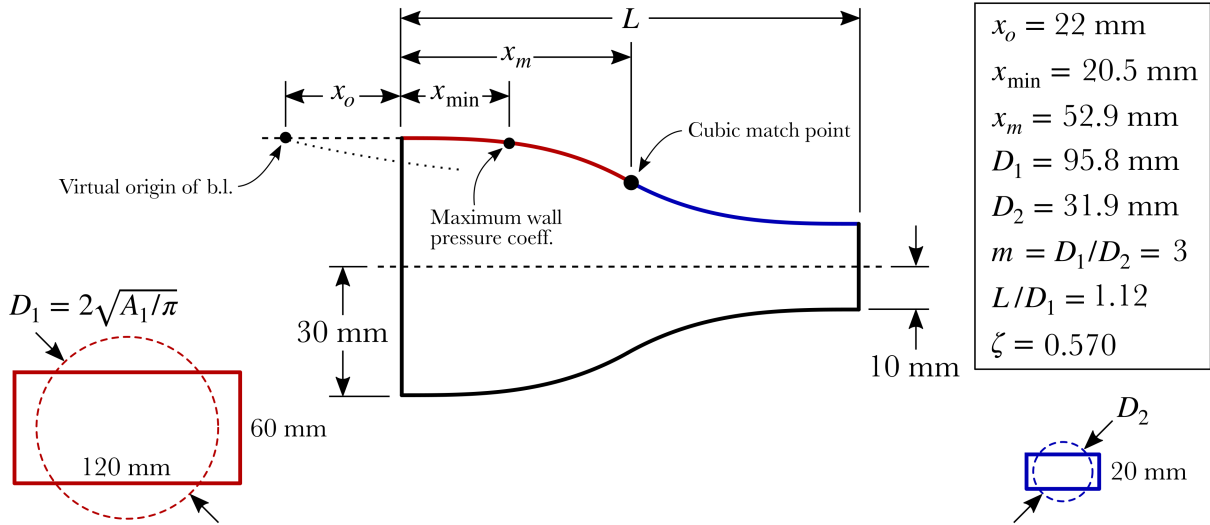


**Figure 3-2. Final contraction geometry resulting from the Morel axisymmetric design method, relevant design parameters, and equivalent inlet and outlet geometries.**

hydraulic diameter. The purpose of the honeycomb is to remove swirl and transverse lateral velocity from the incoming flow, which is accomplished by the extended length of each cell. Mehta [86] suggests that the honeycomb cell length be 7 – 10 times their diameter, with a more modern simulation study by V. Kulkarni et al. [90] suggesting 8 – 10 for screened honeycombs. Longer lengths are not recommended due to boundary layer growth and subsequent turbulence generation within the cells. Additionally, Mehta [86] recommends there be at least 150 cells per settling chamber diameter (smaller than the smallest lateral wavelength of the velocity variation) if the goal of the honeycomb is turbulence suppression. Since this equates to cell diameters of approximately 0.5 mm, which would be prohibitive to manufacture or purchase, it was initially decided to forgo including a honeycomb.

The screen parameters are a more challenging part of the settling chamber design. In general, each screen is composed of a mesh of wires and can be defined by its porosity,  $\beta$ , which is a ratio of its open area to the total area of the mesh. It follows that porosity is directly related to the wire diameter (for circular wires),  $d$ , and the centre-to-centre wire mesh spacing,  $M$ . For square meshes, porosity is defined as:

$$\beta = \left(1 - \frac{d}{M}\right)^2 \quad (3-1)$$



The critical dimensions for each screen is wire diameter and porosity. The Reynolds number based on the wire diameter,  $Re_d$ , should not exceed a critical number or excessive turbulence generation will occur due to shedding [84, 86]. Mehta and Hoffman [91] recommend  $Re_d = 50$  while Groth and Johansson [92] recommend  $Re_d = 40$ . Similarly, the porosity must be at least 0.57 to avoid instability [84, 86]. Based on continuity and contraction ratio the maximum velocity within the settling chamber is  $5.56 \text{ ms}^{-1}$ . For  $Re_{d,\text{max}} = 40$ , this corresponds to a maximum wire diameter of  $d_{\text{max}} = 0.112 \text{ mm}$ .

A series of screens of varying porosity and wire diameter are generally used to produce the required amount of attenuation of the incoming flow non-uniformities [93]. More simplistically, a series of equidistantly spaced, identical screens can be used. A method for determining the screen parameters and their spacing in this case is provided by a numerical and experimentally verified study by P. E. Hancock [94]. Hancock [94] considers a series of  $N$  screens with an upstream, streamwise velocity field defined as  $U = \bar{U} + u$ , where  $\bar{U}$  is the mean flow velocity and  $u$  is the spatial perturbation defined by:

$$u = \{u_0\}_{(l,m)} \sin(l y) \sin(m z) \quad (3-2)$$

Attenuation is defined for a given mode of this incoming flow (based on wavenumbers  $l$  and  $m$ ) by  $\{u_N\}_{(l,m)} / \{u_0\}_{(l,m)}$ , where  $u_0$  and  $u_N$  are the amplitudes of the incoming and outgoing flow perturbation. Hancock's study [94] requires specification of the static pressure drop coefficient,  $K$ , shared by the screens and provides the spacing,  $X$ , required for a given degree of attenuation. Estimating the static pressure drop coefficient of a screen may be accomplished by a number of correlations; in this case a relation given by Groth and Johansson [92] is used which is based on the solidity of each screen,  $\sigma = 1 - \beta$ , and an empirical function  $f(Re_d)$ :

$$K \equiv f(Re_d) \frac{1 - (1 - \sigma)^2}{(1 - \sigma)^2} \quad (3-3)$$

This correlation is used because Groth and Johansson [92] provide empirical measurements of  $f(Re_d)$  for a number of screens with wire diameters similar to the maximum determined above. An attenuation to at least 3% ( $\pm 0.03$ ) was deemed adequate, as any spacing of screens with  $\Sigma K > 2.5$  will provide an attenuation of at least 11% and 3% is the best attenuation supported by the studies experimental verification. For  $\Sigma K = NK > 4$ , Hancock [94] gives the attenuation

for  $\Sigma K$  and spacing parameter  $NX/H$ , where  $H$  is the duct height, and shows that for a given level of attenuation there is a minimum  $NX/H$  required to ensure at least that level regardless of  $\Sigma K$ . Choosing  $NX/H \approx 0.64$  therefore ensures that the attenuation for any given  $\Sigma K$  is theoretically better than 3%, regardless of changes to the screen pressure drop coefficient (due to variations in  $Re_d$  or  $K$ , for example). It is important to note that these results are given for the largest scale perturbation present in the flow, and an assumption is made that the highest amplitude perturbations belong to the lower wave numbers.

Based on the foregoing specifications of porosity and wire diameter, a wire mesh with  $d = 0.043$  inch (0.11 mm) and  $\beta = 62.7\%$  was chosen, considering availability. At  $Re_{d,max} = 40$ ,  $f(Re_d) \approx 0.9$  and  $K = 1.4$ .  $N = 4$  screens was chosen to ensure that  $\Sigma K > 4$  for the operating range of the wind tunnel. The final spacing for the screens was therefore determined to be  $X = 19.2$  mm, based on a tunnel height of 120 mm (the longest tunnel dimension). However, in the final design a honeycomb was included in order to aid in maintaining the flow direction. An aluminum honeycomb sheet with cell diameters of 3 mm and a depth of 14 mm was selected from available materials based on these requirements, and one of the four screen mounting plates was modified to accommodate the honeycomb. Table 3-1 summarizes the resulting parameters for different values of  $Re_d$ , from the minimum required flow to the design maximum, and considering the reduction to three screens. Although with three screens  $NX/H < 0.64$  the increased  $K$  of the screens with decreasing  $Re_d$  allows for similar attenuation to the maximum case with four screens. For higher velocities nearer the design maximum it would be beneficial to machine a replacement screen mounting plate and operate the wind tunnel with four screens.

A circular-rectangular transition was required to connect the circular hose outlet ( $1\frac{1}{8}$  inch, 28.575 mm inner diameter) of the flow source to the rectangular inlet of the diffuser. Good performance of both the diffuser and transition required avoiding transitory stall, where separation periodically occurs at any of the diverging walls. The key parameter for achieving this for a plane-wall diffuser was the larger half-angle between the diverging walls, and the area ratio [86]. For the transition, the area ratio and length are of similar importance [95, 96]. The design proceeded as follows: the outlet size of the diffuser was set by the settling chamber dimensions (60 mm  $\times$  120 mm) while the inlet dimensions needed to match those of the

transition outlet. The transition, changing from a circle to an aspect ratio 2 rectangle, provided some diffusion with the final height matching the inlet diameter in order to adhere to the design guidelines by Miller [95]. Based on design guidelines by Miller [95], circular-rectangular transitioning diffusers operate similarly to conical diffusers of equivalent half-angle, where the half-angle should be less than  $5^\circ$ . For steady, unseparated flow the inlet radius to length ratio was therefore set to 8.5 [95] yielding a length of 149 mm and outlet dimensions of 35.052 mm  $\times$  70.104 mm (equivalent half-angle of  $4^\circ$ ). The final design parameter was therefore the diffuser half-angle, chosen to be  $6^\circ$  again based on guidelines by Miller [95] as well as Mehta [86], where a wire mesh screen was assumed present at the inlet. Wire mesh screens have been found to have a favourable impact on the stall performance of wide-angle diffusers [97, 98]; based on design guidelines by Farell and Xia [97] the foregoing diffuser benefits from a screen of arbitrary pressure drop at the outlet. Therefore, screens equivalent to those chosen for the settling chamber were added to the inlet and outlet (Figure B-7), with no appreciable stall regime expected [98]. The final length of the diffuser was therefore set to 238.018 mm.

**Table 3-1. Screen design parameters for different  $Re_d$ .**

$\bar{U}$ (m/s)	$Re_d$	$f(Re_d)$	$K$	$N$	$\Sigma K$	$\frac{NX}{H}$	$X$ (mm)	$\frac{u_N}{u_0}$
5	4	3.1	4.79	3	14.36	0.48	19.2	< 1%
10	8	2.0	3.09	3	9.26	0.48	19.2	< 3%
20	16	1.5	2.32	3	6.95	0.48	19.2	< 5%
50	40	0.9	1.39	4	5.56	0.64	19.2	< 3%

Each component of the flow conditioner was CNC milled from 6061 aluminum alloy to the specifications outlined in Appendix A. Also, each interior surface of the flow conditioner was stoned smooth in the direction of flow to remove tool marks. The screen holders (Figure B-5), honeycomb holder (Figure B-5), and diffuser mounting plates (Figure B-7) were each designed to accommodate 0.060 in rubber gaskets in order to seal the screen against the facing surface. The depth of each inset (1.52 mm) is set to the thickness of these gaskets, where the thickness of the wire mesh (0.14 mm) is accommodated by 10% compression of the gasket.

Accounting for the wire mesh and a deformation tolerance of 0.5 mm, the screen mount thickness was machined to 19.84 mm in order to match the desired inter-screen spacing of 19.2 mm. Also, as opposed to maintaining the inlet aspect ratio, the width of the transition outlet was changed slightly to 69.967 mm in order to hold the smaller half-angle to  $3^\circ$ , which was more convenient to machine (Figures B-8 and B-9).

Finally, pressure taps were installed into the final screen mount (Figure B-5) and the turbulence grid holding plate (Figure B-2) in order to measure the pressure drop across the contraction. For the same outlet condition, the pressure drop across the contraction provides a measure of the flow rate to the test section, and is therefore useful in metering the flow without the use of other apparatus. Four pressure taps were included in both components and were positioned at the wall centrelines. At the outlet, the pressure taps are placed prior to any turbulence grid. Both the high and low pressure tap sets are measured in parallel through conjoined tubes of equal length by a differential pressure transducer (Omega PX653, 10 inH<sub>2</sub>O).

## 3.2 Experimental Setup

In order to validate the performance of the wind tunnel, and to characterize the flow fields for the desired experimental conditions, two flow measurement techniques were employed. The first of these is hot-wire anemometry, where the voltage required to heat a thin filament to a constant temperature is measured. When exposed to airflow the heat required changes with the velocity of the gas; after calibration the velocity may then be interpreted from the voltage measurements directly. The second technique is particle image velocimetry (PIV). This technique involves illuminating particles seeded into the gas flow, and rapidly imaging the particles with a known time delay. After image processing, the movement of the particles in the field of view between frames allows non-invasive measurement of the velocity field within the focus plane.

The flow conditions in each case were manipulated through a combination of the air supply, settling chamber, and turbulence grids placed at the contraction exit (or test section inlet). Air was supplied to the wind tunnel by a centrifugal blower equipped with a variable

frequency controller. The blower frequency was held constant at 20 Hz while the volume of airflow to the wind tunnel was controlled by two ball valves which opened to the ambient, with the remainder flowing to the flow conditioner. The conditioner then reduced the turbulence intensity and promoted uniformity in the airflow before it reached the test section (or duct) inlet. This provided a baseline flow at each Reynolds number (Baseline cases) with a minimum inlet turbulence intensity. However, the inlet turbulence intensity was finally varied by placing wire meshes (Grid cases) at the inlet of the duct, which increased the inlet turbulence intensity compared to the Baseline case where no grid was present. Together, this allowed variation of the flow Reynolds number and inlet turbulence intensity.

Three Grids were employed in addition to the open inlet case. Each Grid was mounted in an interchangeable plate (Figure B-2), with an empty plate serving as the Baseline case. These plates were then held in a machined inset in a separate plate (Figure B-2) attached between the exit of the contraction and the test section (Figure B-1). The wire mesh dimensions for each Grid, numbered 1 through 3, are detailed in Table 3-2. As with the settling chamber screens, each grid was composed of a square mesh of circular wires with diameter  $d$  and centre-to-centre wire spacing  $M$ . The wire spacing was chosen such that each grid was a unique combination of two diameters and two different porosities,  $\beta$ . The wire diameters were chosen based on criteria given by Roach [99] for generating near-isotropic turbulence, where the wire diameter should not exceed 10% of the duct cross-section dimensions. The largest wire diameter in this case was  $d = 0.4$  mm, yielding  $d/a = 2\%$ .

The test sections employed were also interchangeable, with a number of different ducts employed depending on the situation, as described below. Regardless of the experiment, the test section remained rectangular with a  $20 \times 40$  mm cross-section. Several aluminum ducts were employed, where each duct was CNC machined from 6061 aluminum and stoned in the axial direction to remove tool marks. A single-piece glass duct was also employed where ubiquitous optical access was required. A separate test section was also used for the evaporation measurements, which was designed to hold the evaporating lubricant samples. Mounting plates fixed at the ends of each duct allowed attachment to the contraction exit. Similarly, mounting plates at the end of the aluminum ducts allowed placement of the evaporation test section at a specific axial position.

**Table 3-2. Wire mesh dimensions for each turbulence grid.**

Case	$d$ (mm)	$M$ (mm)	$\beta$ (%)	$u'_{rms}/U$ ([25], $x/d = 30$ , $Re_{D_h} = 1.7 \times 10^4$ )	$u'_{rms}/U$ ([25], $x/d = 30$ , $Re_{D_h} = 3.5 \times 10^4$ )
Baseline	–	–	–	0.87	0.68
Grid 1	0.4	1.2	44	5.68	4.97
Grid 2	0.25	1.35	66	7.16	6.11
Grid 3	0.4	2.1	66	8.32	7.21

The major components of the evaporation test section are shown in Figure 3-3, including: borosilicate glass windows for optical access a copper heater block with two 150 W cartridge heaters installed, a copper film holder composed of a shallow inset and a reservoir which are 250  $\mu\text{m}$  and 2.5 mm deep, respectively, and a ceramic insulator plate which allowed contact between the film holder and heater block while insulating the remainder of the assembly. The film holder and windows were mounted flush with the walls of the duct. The inset of the film holder was square with a width of  $c = 25$  mm. During PIV measurements, the ceramic insulator plate and copper film holder were replaced with a black, non-reflective polycarbonate piece which replicates their geometry.

Three experimental setups were created, employing both hot-wire and PIV, in order to characterize the flow. The shared coordinate system used in each experiment is denoted in Figure 3-4; regardless of length or construction the test section was always a duct with a  $20 \times 40$  mm cross-section. The layout of each experiment is shown in Figure 3-5. First, hot-wire measurements were taken at the exit of the contraction in order to establish the flow uniformity and inlet turbulence (Figure 3-5a). A duct 200 mm in length was attached to allow access by the hot-wire probe from the duct exit without allowing the contraction to eject into ambient air. Measurements were also completed along the duct centreline to establish the variation in turbulence intensity with axial distance ( $x = 0 - 200$  mm) for each inlet condition. Second, a transparent glass duct 1 m in length was attached to allow optical access for PIV measurements along a significant duct length (Figure 3-5b). The purpose of these measurements was to

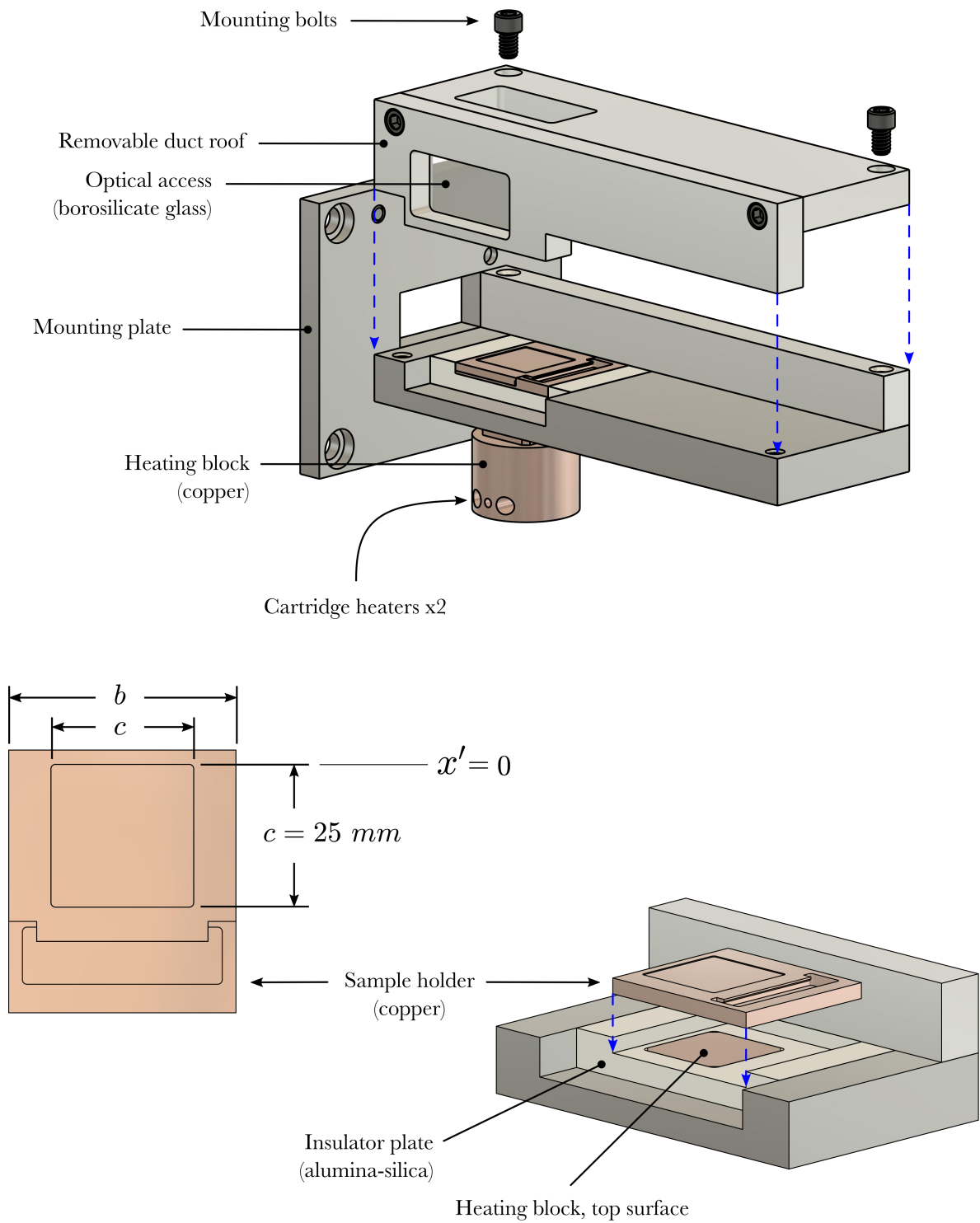


**Figure 3-3. Major components of the evaporation test section and their assembly. Also shown are the sample holder inset geometry and coordinate system based on the inset leading edge.**

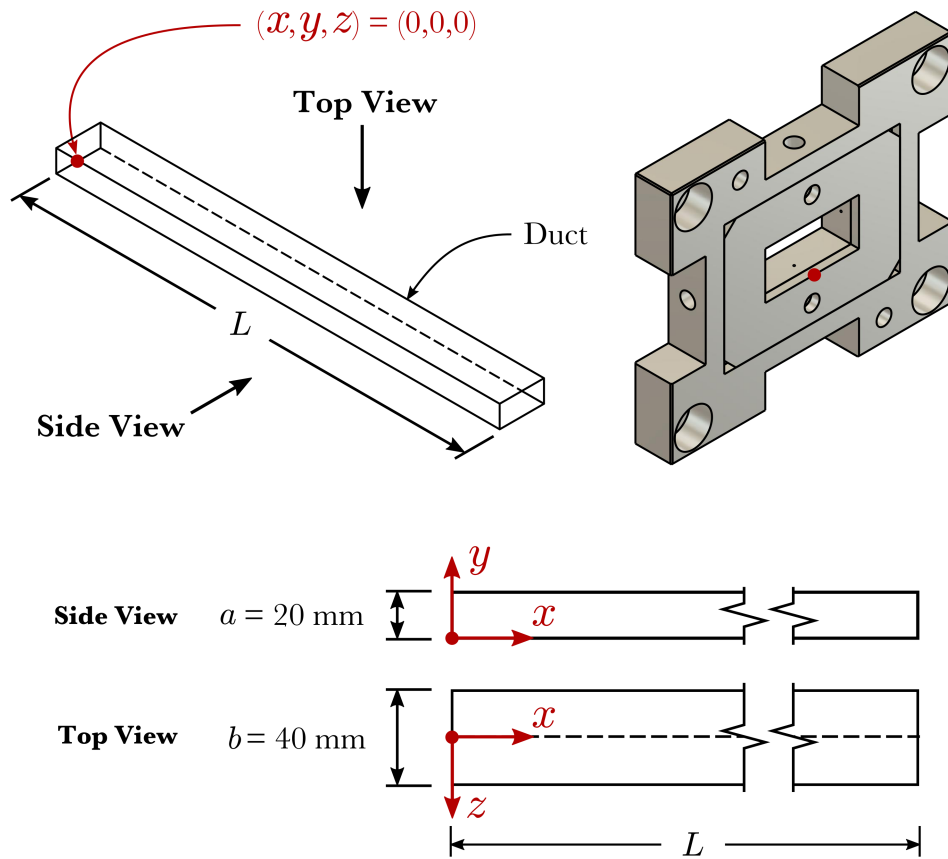


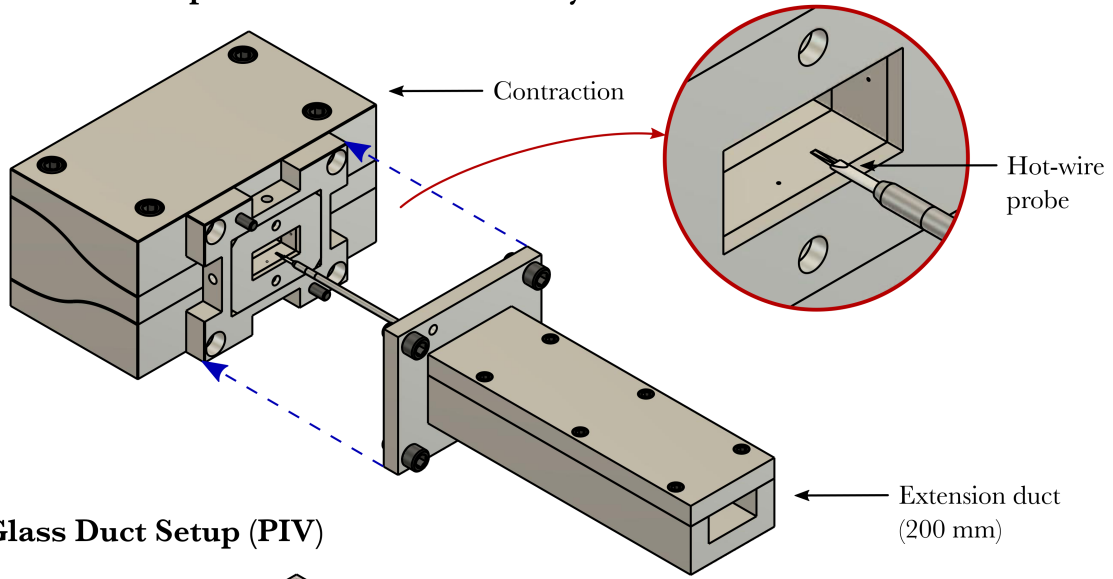
**Figure 3-4. General coordinate system and duct geometry implemented for the experimental fluids measurements.**

establish the development of the flow for a range of potential operating conditions. The goal of this work is to establish the effect of boundary layer conditions on the evaporation of engine lubricant films, and so a variety of boundary layer conditions (near wall turbulence intensity, shape factor, boundary layer thickness, etc.) was desired. Third, PIV measurements were completed within the evaporation test section shown in Figure 3-3 at axial locations along the duct where appropriate boundary layer properties were identified (Figure 3-5c). The purpose of these PIV measurements was to characterize the boundary layer flows incident on the evaporating liquid films.

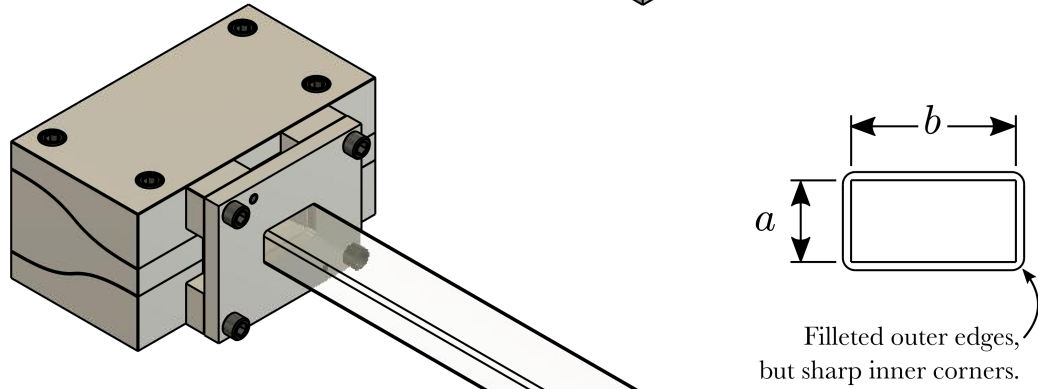
The hot-wire measurements were accomplished using a single-component, normal hot-wire probe (Dantec 55P11) and a constant temperature hot-wire anemometry system (Dantec Streamline Constant Temperature Anemometry System). The hot-wire voltage was sampled at 16 kHz and low pass filtered at 8 kHz. The corresponding velocities were inferred through



**a) Hot-wire Setup & Contraction Assembly**



**b) Glass Duct Setup (PIV)**



**c) Evaporation Test Section Setup (PIV)**

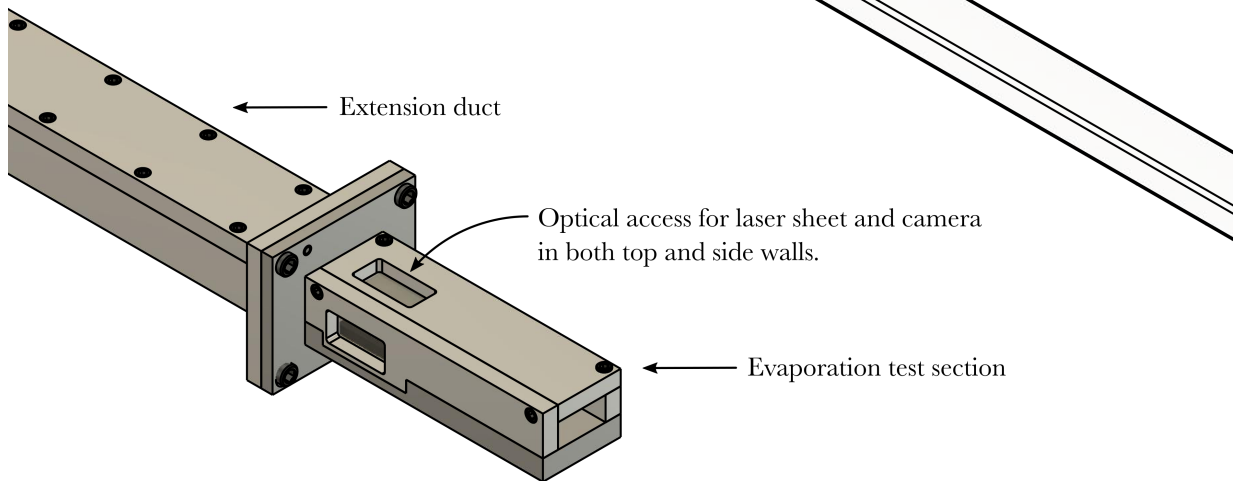


**Figure 3-5. Experimental setups for experimental fluids measurements.**

calibration. During calibration, static pressure measurements via a pitot tube and voltage measurements via the hot-wire probe were taken at symmetric locations within the test section at  $x = 0$  ( $y = a/2, z = \pm b/4$ ). A calibration for the hot-wire measurement was then produced by a fourth-order polynomial fit of the time-averaged velocity data with respect to the time-averaged voltage:

$$u(x) = 20.45v^4 - 129.94v^3 + 329.70v^2 - 381.85v + 166.45 \quad (3-4)$$

The system used to perform the PIV measurements for the experiments shown in Figure 3-5b and Figure 3-5c included a dual pulsed Nd:YAG laser with a maximum output of 70 mJ, a  $1600 \times 1200$  pixel 14-bit Imager Pro X CCD camera fitted with a Nikon 200 mm fixed focal length macro lens, and a programmable timing unit. The resulting combination of spherical lenses, a right-angle mirror, and a cylindrical lens produced a laser sheet approximately 1 mm thick at its waist. The laser sheet was then introduced into the test section through either the glass walls of the duct or the glass windows mounted in the evaporation test section. The camera and laser were mounted and aligned using a set of servo driven traverses which allowed simultaneous movement in the  $x$ ,  $y$ , and  $z$  directions. This ensured that the focus plane of the camera always remained aligned with the laser sheet, and together remained aligned to the tunnel geometry during repositioning. Flow seeding was accomplished using a fog machine located at the blower inlet. This resulted in a uniform seeding of particles 3  $\mu\text{m}$  in diameter.

Within the glass duct shown in Figure 3-5b, the velocity fields in the  $x$ - $y$  plane at  $z = 0$  were interrogated at 17 different axial duct locations through PIV:  $x/a = 1.5, 2, 2.5, 3.75, 5, 6.25, 7.5, 10, 12.5, 17.5, 22.5, 25, 27.5, 32.5, 35, 40,$  and 45. The particle images, and resulting velocity fields, at each location are referred to as lying within a field of view (FOV). For each FOV, 2000 image pairs were acquired at a rate of 14.7 Hz for statistical analysis of the velocity fields, which were computed through the cross-correlation of successive image pairs. The images in all cases were processed in DaVis 8 using an advanced multi-pass method where the initial and final correlation passes were  $64 \times 64$  pixels with 50% overlap and  $24 \times 24$  pixels with 75% overlap, respectively. Each FOV was  $13.1 \times 9.8 \text{ mm}^2$ , with an image magnification of 0.9, yielding 30,000 velocity vectors with a 0.076 mm vector pitch. The random errors in the PIV measurements were evaluated using the particle image disparity method [100], with the

associated average uncertainties in the velocity fields estimated to be less than 4.5% and 2% within the 95% confidence for the near-wall and inviscid core (outside the boundary layers) regions, respectively.

Detailed PIV measurements were taken in the volume above the film holder within the evaporation test section, as shown in Figure 3-5c. Two axial locations were chosen for the evaporation measurements:  $x/a = 2$  ( $x = 40$  mm) and  $x/a = 45$  ( $x = 900$  mm). These locations were chosen based on the flow development observed within the glass duct (Figure Bc), which are detailed in the following sections. With the evaporation test section attached the leading edge of the film holder was located at each position; for  $x/a = 2$  the test section was attached directly to the outlet of the contraction, whereas an aluminium extension duct was machined to locate the test section at  $x/a = 45$ . In both cases, FOVs in the  $x$ - $y$  plane were spaced across the film holder in 1 mm intervals within  $0 \text{ mm} \leq z \leq 9 \text{ mm}$  ( $0 \leq z/c \leq 0.36$ ). For  $x/a = 2$ , two FOVs were employed due to the presence of a thin boundary layer in the vicinity of duct inlet, with a scale factor of 120 pixels/mm for each FOV ( $13.3 \times 10 \text{ mm}^2$ ) and a 3.6 mm overlap between them in order to cover the length of the film,  $c = 25$  mm. For  $x/a = 45$ , a single FOV with a scale factor of 62 pixels/mm ( $25.8 \times 19.4 \text{ mm}^2$ ) was used. In each case, 1500 images were captured at 14.7 Hz in order to produce time-averaged vector fields and statistics. The resulting vector spacing was 76  $\mu\text{m}$  and 150  $\mu\text{m}$  for the  $x/a = 2$  and  $x/a = 45$  cases, respectively.

Similarly, PIV measurements were also taken for FOVs in the  $x$ - $z$  plane. For both  $x/a = 2$  and  $x/a = 45$  FOVs were spaced above the inset surface within  $0 \leq y/a \leq 0.5$ , each with a scale factor of 62 pixels/mm ( $25.8 \times 19.4 \text{ mm}^2$ ). Specifically, FOVs were located at  $y/a = 0.025, 0.05, 0.075, 0.1, 0.125, 0.175, 0.225, 0.3, 0.375, \text{ and } 0.45$ . As in the  $x$ - $y$  plane measurements, 1500 images were captured at 14.7 Hz and the resulting vector spacing was 150  $\mu\text{m}$  for both axial locations.

Additional measurements were taken in the  $x$ - $y$  plane to verify that boundary layer flow incoming to the film adhered to the law of the wall. An FOV at  $z = 0$  covering  $-0.1 \leq x'/c \leq 0$  was employed, where the bottom wall was unbroken by the sample holder inset. A scale factor of 120 pixels/mm was present for these measurements, resulting in an FOV 13.3 mm high in order to fully capture  $0 \leq y/a \leq 0.5$ . The camera was oriented  $90^\circ$  relative to the similar  $x/a =$

2 measurements in order to orient the longer FOV dimension in the  $y$  direction. The measurement and processing parameters were otherwise the same as in the other measurements.

### 3.3 Flow Characterization

The following section details the results of the PIV and hot-wire measurements described in foregoing chapters. A summary of the experimental conditions is followed by a validation of the flow conditioner performance through hot-wire measurements at the contraction outlet (Figure 3-5a). The PIV measurements within the full-length glass duct (Figure 3-5b) are then considered with respect to boundary layer development. Finally, the PIV measurements within the evaporation test section for the boundary layer flow incident on the film samples are explored (Figure 3-5c).

#### 3.3.1 Experimental Conditions

The foregoing experiments were conducted for three Reynolds numbers based on the duct hydraulic diameter,  $D_h = 26.67$  mm:  $Re_{D_h} = 10,650$  ( $1.0 \times 10^4$ ),  $17,750$  ( $1.7 \times 10^4$ ), and  $35,500$  ( $3.5 \times 10^4$ ). Measurements were taken for each combination of  $Re_{D_h}$  and inlet condition excepting the  $Re_{D_h} = 10,650$  cases under Grid 1 and 2, which were omitted. The flow rate through the duct was constant in each case, and corresponded to mean velocities of approximately 6, 10, and 20 m/s. An additional  $Re_{D_h} = 71,000$  ( $7.1 \times 10^4$ ) case is included to inspect the operation of the wind tunnel with three screens, outside of its original four screen design.

These velocities were considered suitable for the evaporation experiments based on their similarity to the range of velocities experienced near the cylinder wall during the compression and expansion strokes. Under typical engine operation (1000 – 3000 RPM, 80 mm stroke) the mean piston velocity,  $\bar{V}_p$ , is approximately 2.7 – 8 m/s, with the mean tangential velocity component near the liner falling in the range of  $\bar{V}_p - 6\bar{V}_p$  [52]. This conservatively places the

near-wall velocities within 3 – 50 m/s. The velocities in real engines obviously considerably, but for the above conditions these values are approximately representative.

Prior to running each experiment both the blower and wind tunnel were allowed to reach a steady temperature. In all cases, the test section wall and air temperatures were held at  $19 \pm 1^\circ\text{C}$ . Table 3-3 below tabulates the various air properties used during post-processing based on that temperature.

**Table 3-3. Dry air properties at  $19^\circ\text{C}$ .**

$T$	$\rho$	$\nu$	$\mu$	$k$	$c_p$	Pr
(K)	( $\text{kg}/\text{m}^3$ )	( $10^{-5} \text{ m}^2/\text{s}$ )	( $10^{-5} \text{ kg}/\text{ms}$ )	( $10^{-5} \text{ W}/\text{mK}$ )	( $\text{kJ}/\text{kgK}$ )	
292	1.211	1.496	1.807	2.561	1.0045	0.709

### 3.3.2 Flow Conditioner Performance

The hot-wire experiments described above and in Figure 3-5a measured the instantaneous velocity across the cross-section of the duct at the outlet of the contraction. The purpose of those measurements was to ascertain whether the flow conditioner produces airflow of sufficient uniformity and with low turbulence intensity at each Reynolds number under consideration. Figure 3-6 below shows the resulting velocity measurements at  $x/a = 0.5$ ,  $z = 0$ , from  $y/a = 0.05 - 0.65$ .

Figure 3-6 presents the difference between the measured velocity and the centreline velocity, with respect to the centreline velocity,  $U_c$ . This gives a quantitative measure of the non-uniformity in the streamwise velocity across the height of the channel. For each Reynolds number, the velocity varies between 0% and 0.5% of the centreline velocity from the centreline to  $y/a = 0.15$ . Nearer to the wall, between  $y/a = 0.05$  and 0.15, the existence of a boundary layer is evident. This is expected, since the boundary layer within the contraction will reach minimum thickness downstream of the *vena contracta* and will continue to grow from that point. The *vena contracta* is the point at which the flow cross-section is minimum, due to abrupt change in flow direction which exists at the outlet of the contraction. The location of this minimum

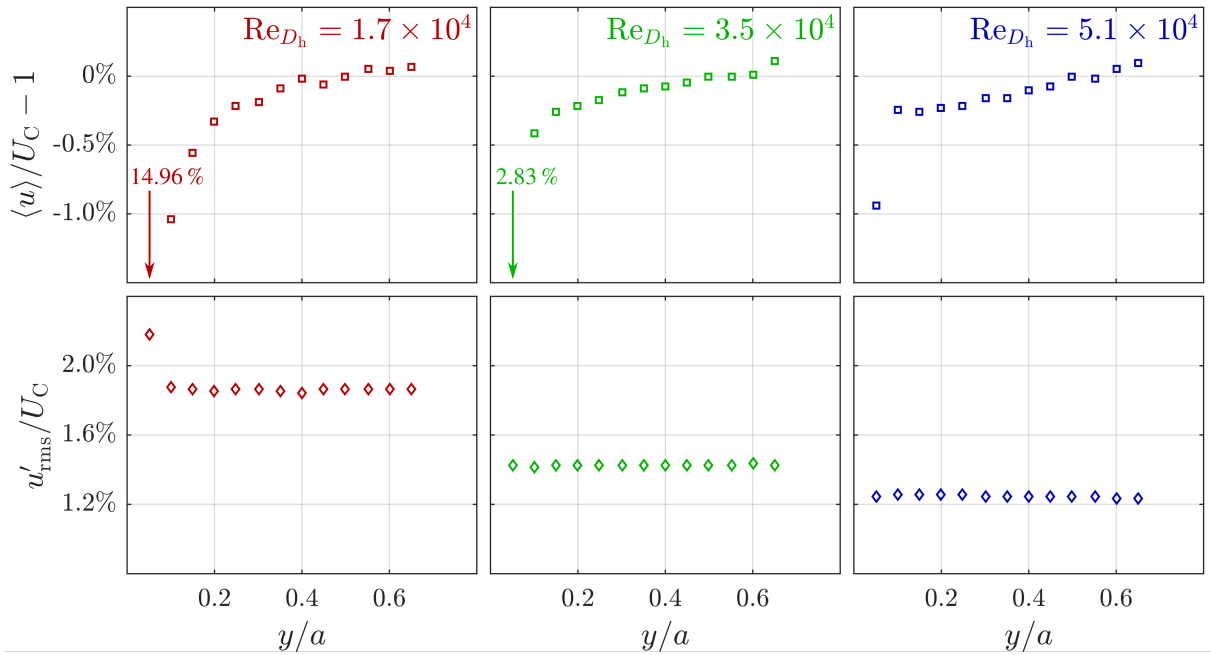


**Figure 3-6. Perturbation of the streamwise velocity and turbulence intensity for  $Re_{D_h} = 1.0 \times 10^4$ ,  $1.7 \times 10^4$ , and  $3.5 \times 10^4$  at the contraction exit.**

will change with  $Re_{D_h}$  as the *vena contracta* changes size [87, 95]; it is for this reason that the wind tunnel adaptor plate which holds the turbulence grids is 5/8 inches (15.875 mm) thick, and the origin of the duct is considered at the downstream edge of the same plate (Figure 3-2).

The baseline turbulence intensity for each  $Re_{D_h}$  case falls within 1.2 – 1.9% in the inviscid core flow, which is acceptable [84]. The magnitude of the turbulence intensity is shown to decrease with  $Re_{D_h}$ , which is expected [25]. In addition, the turbulence intensity shown in Figure 3-6 is uniform across the height of the tunnel for each  $Re_{D_h}$ , with a maximum deviation of  $\pm 0.02\%$ . No irregularities are present in the  $Re_{D_h} = 1.7 \times 10^4$  case, which implies either that operating the settling chamber with three screens instead of four provides adequate attenuation or any adverse effects are removed by the contraction.

The centreline turbulence intensity produced by each wire mesh Grid was established by Tuna et al. [25] through hot-wire measurement. The resulting values at  $x/d = 30$  are listed in Table 3-2 for  $Re_{D_h} = 1.7 \times 10^4$  and  $3.5 \times 10^4$ . This determined the relative magnitudes of inlet turbulence produced by each mesh and their numbering (1 – 3) in order of ascending centreline turbulence intensity. Tuna et al. [25] provide a more in-depth analysis of the  $Re_{D_h} =$

$1.7 \times 10^4$  and  $3.5 \times 10^4$  data-set referenced in this study, with a focus on the development of the duct flow and the influence of grid generated turbulence.

### 3.3.3 Duct Flow Measurements

The PIV measurements conducted using the glass tunnel (Figure 3-5b) describe the flow field within the  $x$ - $y$  plane at the duct centreline for the entire domain considered in this study ( $0 < x/a < 50$ ). The primary purpose of these measurements was to ascertain the development of the boundary layers which would interact with the oil films during the evaporation measurements. The goal of this study is to evaluate both the affect of near-wall turbulence, the affect of boundary layer shape (shear stress and velocity gradient), and Reynolds number on the lubricant film evaporation. Consequently, boundary layer conditions which allow comparison of different near-wall turbulence intensities for similar boundary layer shapes (thickness) as well as comparison of different boundary layer shapes for the same Reynolds number were required. Simultaneously, it was considered advantageous if no more than two measurement locations were chosen in order to limit cost and time.

The latter requirement was met by choosing locations within the domain in order to take advantage of the duct boundary layer growth. Figure 3-7 below demonstrates the evolution of the boundary layer shape factor with axial distance for the Baseline,  $Re_{D_h} = 1.7 \times 10^4$  and  $3.5 \times 10^4$  cases. For the Reynolds numbers chosen ( $Re_{D_h} > 10,000$ ) it was expected that fully developed turbulent flow would occur within the length of the duct ( $L = 37.5D_h$ ) for each of the Grid inlet cases [35]. This requires the flow to transition (or remain) turbulent and finally reach steady state with axial distance, where the boundary layer thickness reaches the centre of the duct. For the Baseline inlet condition cases, as in Figure 3-7, it was unknown whether transition would necessarily occur within the length of the duct. Figure 3-7 demonstrates that transition occurs for  $Re_{D_h} = 1.7 \times 10^4$  and  $3.5 \times 10^4$  under the Baseline condition, with the originally laminar flow condition ( $H \approx 2.59$ ) transitioning to turbulent flow ( $H \approx 1.4 - 1.6$ ) by  $x/a = 32.5$  and  $x/a = 25$  respectively. The Baseline,  $Re_{D_h} = 1.0 \times 10^4$  case did not transition within the length of the duct. However, each Grid case was found to be turbulent for the majority of the duct length, including the  $Re_{D_h} = 1.0 \times 10^4$  cases; while only the Grid 3 case is

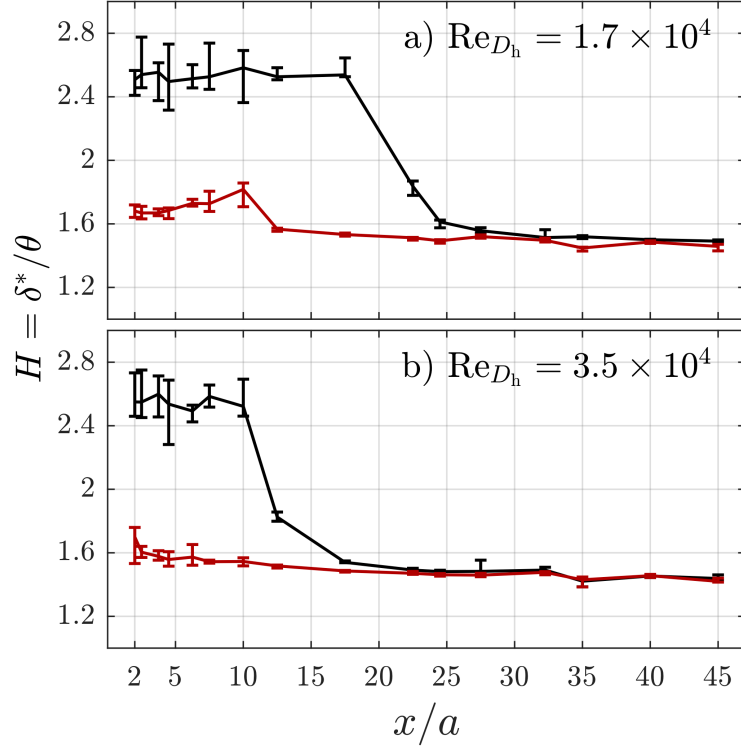


**Figure 3-7. Shape factor variation of the boundary layer within the  $x$ - $y$  plane at the duct centreline ( $z = 0$ ) for Grid 3 (red) and Baseline (black) inlet conditions.**

shown in Figure 3-7 (red) the Grid 1 and 2 cases can be seen in the work of Tuna et al. [25] for  $Re_{D_h} = 1.7 \times 10^4$  and  $3.5 \times 10^4$ . The shape factor uncertainties are the result of random error estimates from the post-processed PIV results. The error is proportionally higher when calculating the integral boundary layer properties over smaller distances (nearer to the error magnitude).

Based on these results,  $x/a = 45$  was chosen to contrast the fully developed turbulent flows, and a single developed laminar case, with the thinner boundary layers present at an upstream location. In each turbulent case the boundary layer thicknesses (within the  $x$ - $y$  plane) reached the centre of the duct prior to  $x/a = 45$ . However, after that point, the centreline velocity in duct flow have been shown to overshoot their fully developed values prior to settling, [25]. This also occurs for each of the foregoing turbulent conditions [25], and so the choice of  $x/a = 45$  provides the greatest leeway for each case to reach a true fully developed condition where the centreline velocity is invariant with axial distance.



Finally, to provide comparison between different levels of turbulence intensities near the film surface, a second measurement location at  $x/a = 2$  was chosen. This location provided different levels of turbulence intensity in each Grid case, as well as a minimum intensity case in the Baseline cases, for each Reynolds number. The boundary layer thickness was also at minimum closest to the inlet, which provided the greatest contrast in terms of boundary layer shape to the  $x/a = 45$  location. However, while the inlet flow was perturbed by the wire meshes in each Grid case, the flow became more homogeneous after  $x/a = 1$  [25]. Therefore,  $x/a = 2$  was chosen, and together with  $x/a = 45$  satisfied each of the requirements stated above.

### 3.3.4 Evaporation Test Section PIV Measurements

The PIV measurements above the sample holder at both  $x/a = 2$  and  $x/a = 45$  were conducted primarily to characterize the boundary layer conditions for future evaporation measurements. In all FOVs the velocity vector fields and statistics were determined through post-processing of the PIV images, which included the streamwise ( $u$ ) and wall-normal ( $v, w$ ) velocities. This in turn allowed calculation of the boundary layer parameters and near-wall turbulence intensities, which are the differentiating features of each convective mass transfer case considered during the evaporation measurements. A representation of the full PIV results for both locations is found in Appendix C, while results relevant to each evaporation measurement are shown in §4.2.

The main differentiating factor between the upstream ( $x/a = 2$ ) and downstream ( $x/a = 45$ ) boundary layers was the degree of development over the intervening length of duct; each case save the Baseline,  $Re_{D_h} = 1.0 \times 10^4$  case was found to attain a similar shape factor by  $x/a = 45$ , which indicated that the boundary layers had transitioned or remained turbulent ( $H = 1.4 - 1.6$ ). As shown in Figure 3-8, this also translated to a common boundary layer profile for the turbulent cases when scaled by the displacement thickness,  $\delta^*$ . The laminar boundary layer exhibited in the Baseline,  $Re_{D_h} = 1.0 \times 10^4$  case is shown in Figure 3-8a, where each other case (Figures 3-8a – 3-8c) demonstrated velocity profiles with shape factors and boundary layer thicknesses of fully developed, turbulent boundary layers. Similarly, the turbulence intensities reached similar values for those cases [25], as shown in Figure C-12d – C-20d.

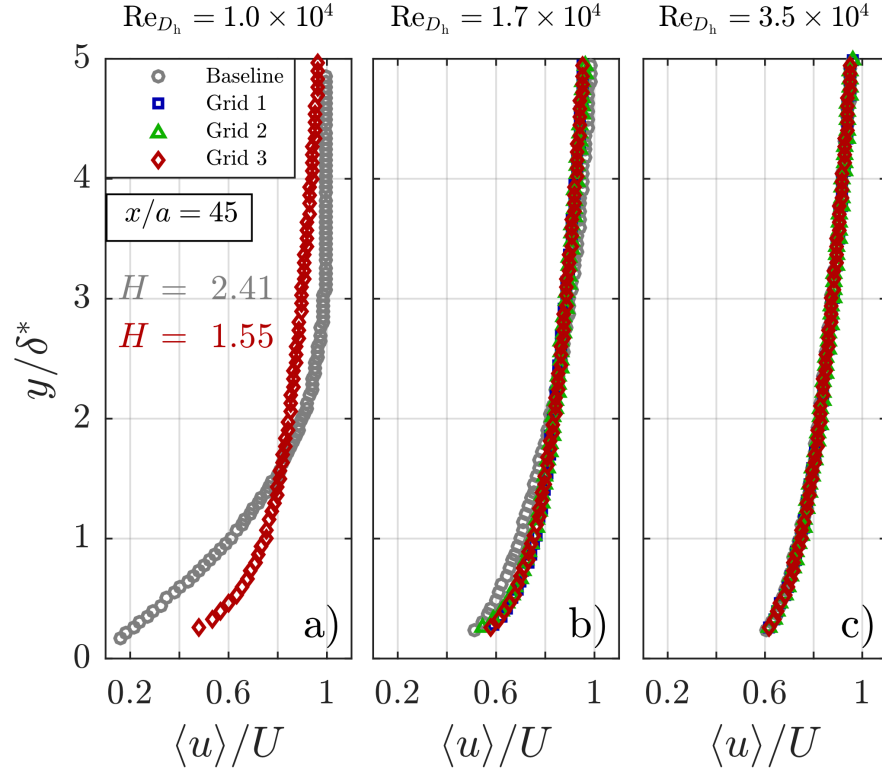


**Figure 3-8. Convergence of downstream velocity profiles for each Reynolds number and inlet condition. Grid 1 and 2 cases omitted for clarity in a).**

In Figure 3-8, and in each velocity profile presented in §4.2, the full results from the sideview measurements are abbreviated to only the  $z = 0$  plane. However, the velocity fields were found to vary little over the volume above the sample holder (within  $0 \leq x'/c \leq 1$ ,  $0 \leq z/c \leq 0.36$ ) in the region near the wall ( $y/a \leq 0.15$ ), although under the Grid inlet conditions significant differences near the boundary layer edges were observed due to the presence of the wire meshes. Figure 3-9 shows the  $\langle u \rangle$  velocity profiles above the sample holder inset for the Baseline,  $Re_{D_h} = 1.7 \times 10^4$  case, which demonstrates the small variation for the same condition at each axial location. In the upstream cases, the small variation in the  $x$ -direction (Figure 3-9a) were due to the relatively small length of the inset versus the entry length at each  $Re_{D_h}$ , whereas for  $x/a = 45$  the duct flow was fully developed and mostly invariant with axial distance (Figures C-12 – C-20). In the  $z$ -direction (Figure 3-9b), small variation was expected due to the similar growth rate of the side-wall boundary layers and the aspect ratio of the duct. However, the effect of the growing side wall boundary layers is evident in the downstream cases as a small

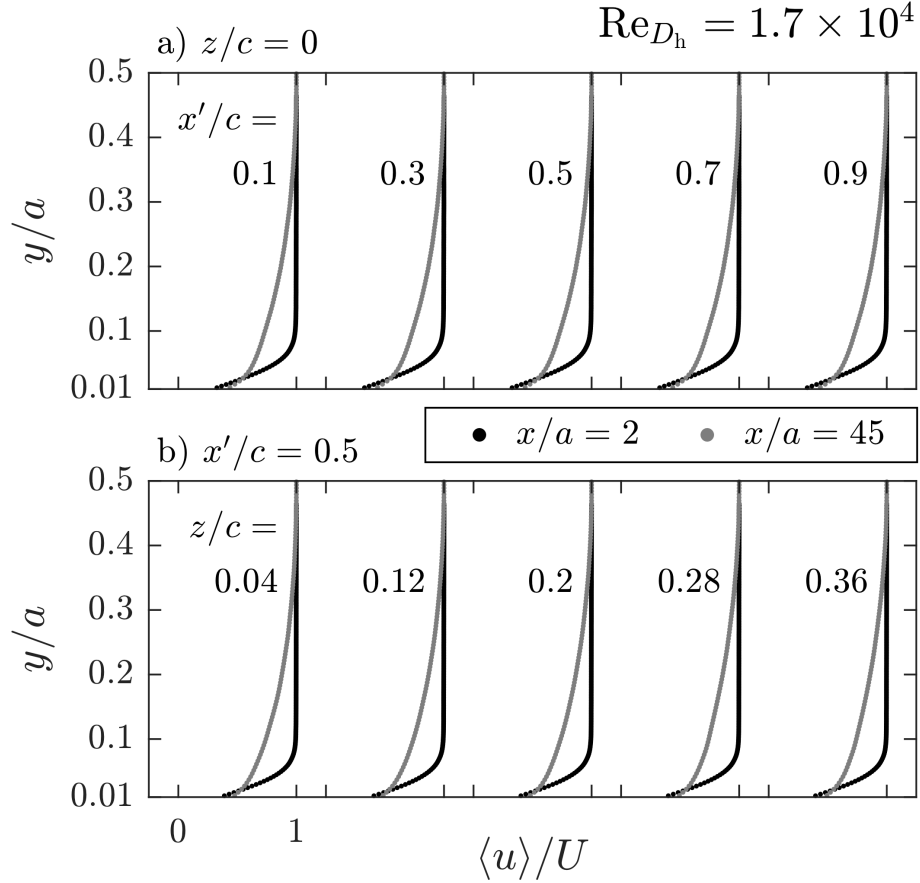


**Figure 3-9. Velocity profiles above the sample holder at each axial location ( $x/a = 2$  and  $45$ ), shown over the length of inset ( $z = 0$ ) and across its half-width ( $x'/a = 0.5$ ).**

decrease in velocity, relative to the  $z = 0$  case, with increasing distance from the centreline (Figures C12b – C20b).

### 3.3.5 Law of the Wall

The additional PIV measurements conducted within the  $x$ - $y$  plane at  $z = 0$ , for  $x/a = 45$  just prior to the sample holder were completed in order to determine if the turbulent boundary layers adhered to the “law of the wall”. Turbulent boundary layers typically follow a linear relationship under wall scaling within the viscous sublayer ( $y^+ \leq 5$ ) and a logarithmic relationship within the logarithmic region ( $30 \leq y^+ \leq 200$ ), as stated in §1.4.2. As the behaviour of turbulent boundary layers within these regimes is supported by numerous experimental

measurements, showing that the “law of the wall” applies to the measured velocity profiles is an indicator that the boundary layer flow is typical and repeatable.

However, accurately scaling velocity measurements is difficult since this requires an accurate measurement or estimation of the wall shear,  $\tau_w$ , in order to calculate the friction velocity,  $u_\tau$ . Measurement of the wall shear directly is difficult, generally requiring invasive methods such as oil film interferometry. Measuring the wall shear from pressure gradient measurements was also inconvenient, requiring minute pressure taps, small tap spacing, and an accurate pressure transducer within the expected range of differential pressures. Alternatively, the wall shear could be calculated by establishing the velocity gradient at the wall from measurements within the viscous sublayer. This in turn is also difficult, as for high  $\text{Re}_{D_h}$  the thickness of this laminar region is prohibitively small ( $y^+ = 5 \rightarrow y = 75 \text{ }\mu\text{m}$  for  $u_\tau = 1 \text{ ms}^{-1}$ ) so obtaining measurements (if any) within this region is not guaranteed.

A common indirect method for determining the shear velocity is to find a best fit for the velocity measurements within the logarithmic region, known as the Clauser method [49]. This method is problematic because of the uncertainty of which measurements lay within the logarithmic region and the choice of von Kármán constant,  $\kappa$  [49]. A similar method is to fit the data to a model mean velocity profile which incorporates the logarithmic region, buffer region, and viscous sublayer such as the method suggested by Kendall and Koochesfahani [49]. Kendall and Koochesfahani [49] recommend fitting both zero pressure gradient and favourable pressure gradient boundary layer measurements to the Musker profile, based on the eddy viscosity model, given by the solution of:

$$\frac{\partial u^+}{\partial y^+} = \frac{\frac{(y^+)^2}{\kappa} + \frac{1}{s}}{(y^+)^3 + \frac{(y^+)^2}{\kappa} + \frac{1}{s}} \quad (3-5)$$

In implementing this method, Kendall and Koochesfahani [49] recommend fitting to the Musker profile through an iterative method which minimizes an aggregate error function,  $\Phi$ , based on a fractional difference between the  $N$  data points ( $u_i^+$ ) and the model ( $u_{m,i}^+$ ) at the same  $y^+$ :

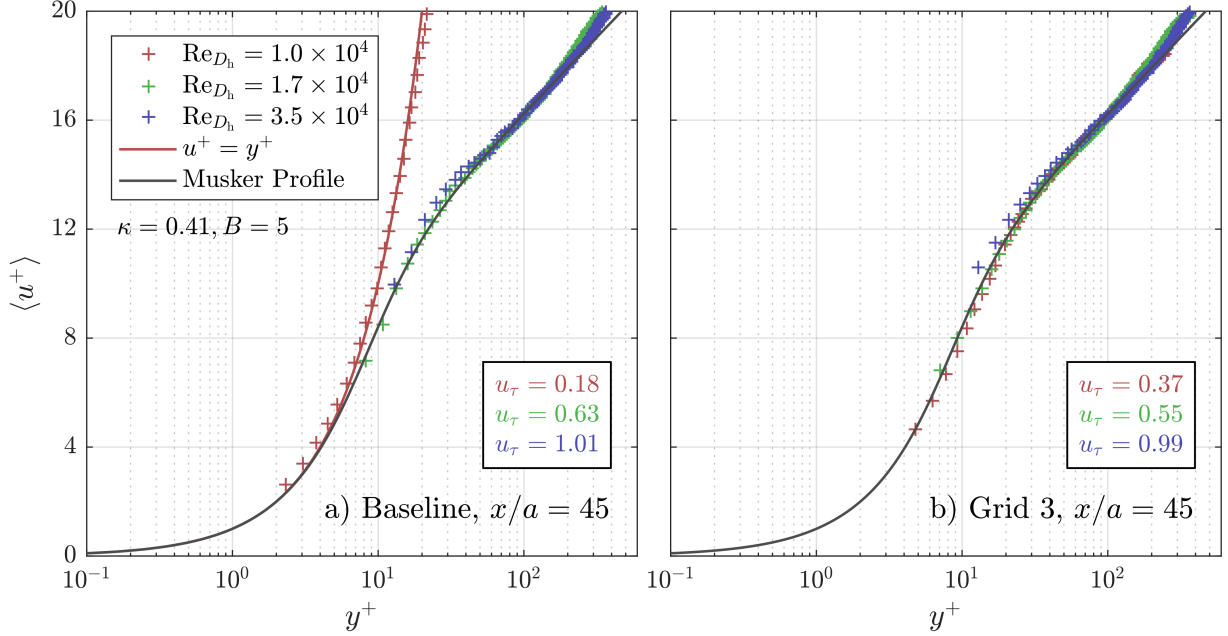


**Figure 3-10.  $u^+$  profiles within the  $x$ - $y$  plane at  $x'/a = -0.1$  ( $x'/a = 45$ ) for each Reynolds number case under the a) Baseline and b) Grid 3 inlet conditions. Profiles are compared to either the Musker profile (black) or  $u^+ = y^+$  (red).**

$$\Phi = \frac{1}{N} \sum_{i=0}^N \frac{|u_i^+ - u_{m,i}^+|}{u_{m,i}^+} \quad (3-6)$$

Another, less accurate method is to approximate the wall shear using a correlation for the friction coefficient [49], such as the first Petukhov equation:

$$C_f = \frac{\tau_w}{\frac{1}{2}\rho U^2} = \frac{1}{4}(0.790 \ln Re_{D_h} - 1.64)^{-2} \quad (3-7)$$

given by Petukhov [35, 101] for smooth, fully developed turbulent flow within ducts ( $10^4 < Re_{D_h} < 10^6$ ).

Figure 3-10 shows the results of fitting the Baseline (Figure 3-10a) and Grid 3 (Figure 3-10b) velocity measurements for each  $Re_{D_h}$  to the Musker profile for  $\kappa = 0.41$  and  $B = 5$ , and in the laminar Baseline,  $Re_{D_h} = 1.0 \times 10^4$  case to  $u^+ = y^+$ . The values of  $\kappa$  and  $B$  were chosen based on common values in each case [38, 43, 49]. In each case, the iterative approach was limited to data falling under  $y^+ \leq 200$  in order to limit the influence of measurements which are close to the outer region nearer to the duct centreline, which is expected to deviate from

logarithmic behaviour [38, 43]. In each turbulent case, the measurements closely adhere to the Musker profile (or linear curve in the laminar case) for their respective shear velocity estimations, up to the edge of the viscous sublayer ( $y^+ = 5$ ) at the limit of the PIV FOV. In addition, the shear velocities given in Figure 3-10 are within 5% of the values given by equation (3-7) for fully developed turbulent flow.

## 4 Evaporation Measurements

The evaporation behaviour of thin lubricant films under airflow was investigated by directly measuring the evaporated mass under differing boundary layer conditions with the liquid oil at an elevated temperature. The evaporation rates in each case were determined by exposing oil film samples to the measurement conditions for several intervals, which demonstrated the evaporation behaviour of the oil with time. The evaporation results for the chosen conditions are explored below, following an outline of the experimental setup and measurement procedure.

### 4.1 Experimental Setup

Each film evaporation measurement was conducted within the evaporation test section described in §3.2. The relevant components are reiterated here along with a more complete explanation of their functions. These components are also shown below in Figure 4-1, along with notes on the clearances between parts for thermal insulation. Each oil film sample was generated within the inset of the sample holder in order to facilitate weighing the oil before and after exposure to airflow. The sample holder itself was constructed in two parts so that a fin overhanging the downstream reservoir could be machined. Both parts together are referred to, here, as the “sample holder”. Any weight measurements and cleaning operations always included both parts. The removable roof and front wall allowed access to the test section so that each prepared sample could be quickly and repeatably positioned.

While positioned within the test section the ceramic insulator plate provided both thermal insulation and mechanical support for the sample holder, preventing it from moving under airflow and ensuring contact with the copper heating block (heater). The top surface of the heating block was raised partially above the lower surface of the insulator plate such that the sample holder contacted the heater while its upper surface was flush with the duct bottom. The vertical position of the heater was adjusted to account for thermal expansion; once at temperature, the desired position was verified by a depth micrometer. In addition, the heater block was wrapped in ceramic-fibre insulation in order to limit heat loss. Two 150 W cylindrical

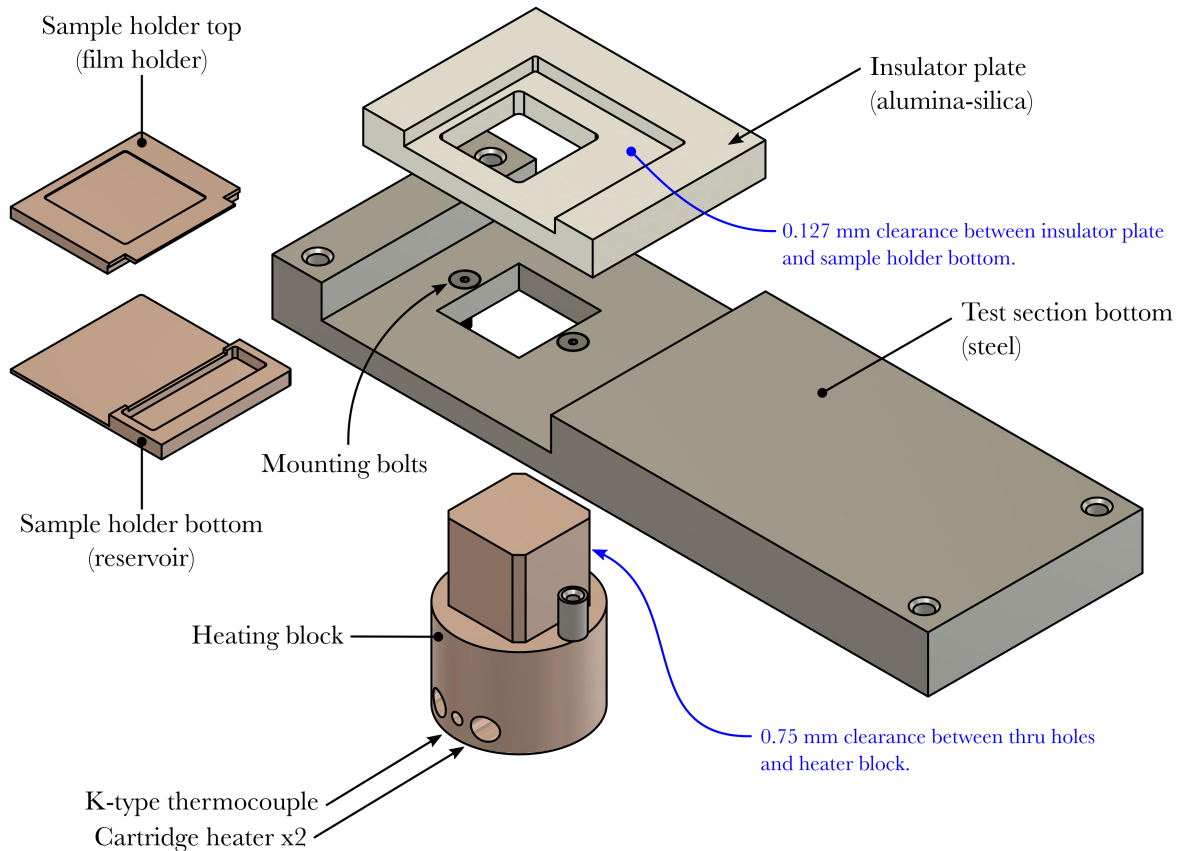


**Figure 4-1. Main components of heated parts within the evaporation test section and the clearances between them.**

cartridge heaters (Omega CIR-1014/120V) inserted into the heater block were used as heat sources. A stainless-steel sheathed K-type thermocouple (Omega KTSS-116) was also inserted equidistantly between the two cartridge heaters to measure the heater base temperature,  $T_b$  (the maximum temperature). Finally, an enclosure was used to safely contain the heater and the associated electrical wiring; the enclosure is not shown in Figure 4-3.

In order to perform constant surface temperature measurements the heat flux from the heating block to the sample holder surface had to be equivalent to the heat lost to convection. To approximate these conditions the heater base temperature was controlled through a tuned PID controller which was informed by the thermocouple installed at its base. With the base held at a constant temperature, and under a single set of boundary layer conditions (convective heat transfer conditions), the surface temperature,  $T_s$ , was expected to assume a single, steady-state temperature. Calibration of  $T_s$  relative to  $T_b$  was accomplished using a K-type surface



mounted thermocouple (Omega SA3-K-SRTC) attached to the inset surface of a sample holder clone, which allowed direct measurement of  $T_s$ . The surface thermocouple was mounted at  $x'/c = 0.5$ ,  $y/c = 0$ . These calibrations were performed prior to the evaporation measurements for each set of airflow conditions, the choice of which is explored below. Each thermocouple was self-calibrated through an NI 9214 module which provides an estimated uncertainty of  $\pm 0.5^\circ\text{C}$ . The temperature control system itself was composed of an FPGA (NI cRIO-9074) a digital IO module (NI 9375), a 20 mA variable current supply module (NI 9265), the multi-channel NI 9214 module, and separate relays for each cartridge heater. Each calibration was composed of two procedures: first, the required base temperature at steady-state was identified; second, the time required to heat the cold sample holder to the desired surface temperature at that base temperature was measured. For the latter, the cold sample holder was placed on the heater and allowed to heat to the desired surface temperature without airflow. Once the surface temperature was reached the airflow was applied and any deviation from the surface temperature was observed. The resulting heating time and base temperature were then used for each measurement in order to approximate a constant film temperature during the measurement duration (under airflow).

The oil film mass loss due to evaporation was measured to investigate the evaporation rate of the oil under specific boundary layer conditions. For each case, oil film samples were prepared, heated to the measurement temperature, and then exposed to the airflow conditions. Each sample was exposed to airflow for a specific duration, with a fresh oil sample being prepared for each measurement from a single, reserved volume of 5W-30 synthetic engine lubricant ( $\rho_o = 8.3 \text{ g/mL}$ ). In order to determine the evaporated mass loss each sample was weighed before and after exposure. The entire measurement procedure was as follows: First, the sample holder was flushed and cleaned with isopropyl alcohol. Next, the sample holder was weighed to establish the non-oil mass of future measurements,  $m_o$ . Handling and cleaning the sample holder, even with sterile gloves, removes oxides at the metal surface and therefore causes sample-to-sample variation of the copper mass. Weight measurements were accomplished via a Sartorius analytical balance (MSE125P-100-DU) with a resolution of  $10 \mu\text{g}$  and repeatability of  $15 \mu\text{g}$ . A draft shield prevented ambient air movement from interfering with the measurements while care was taken to ensure no other vibrations affected each weight

measurement. Each weighing was repeated 3 times, with the measurement taken only once the readout was stable for at least 1 minute, with the final weight taken as the average. The MSE125P self-calibrates upon startup or if the ambient temperature deviates by  $\pm 1^\circ\text{C}$ . If auto-calibration occurred prior to evaporation the measurement process was repeated; if it occurred post-evaporation the current sample was rejected. Next, a volume of oil was deposited onto the sample holder using a syringe. The volume of oil deposited corresponded roughly to the film volume at the desired initial thickness over the  $25\text{ mm} \times 25\text{ mm}$  inset. A ground, stainless steel pin was then used to spread the oil over the inset. After spreading, the film sample was weighed to establish the initial weight of the sample,  $m_1$ . The initial weight of the oil film was then given by:

$$m_i = m_1 - m_o \quad (4-1)$$

Next, the film was placed into the pre-heated evaporation test section (at the correct base temperature) and allowed to heat for the time required for the surface to reach the target measurement temperature. The film was then exposed to airflow by actuating a valve at the entrance of the flow conditioning unit. After the measurement duration the airflow was stopped. The sample was then removed and immediately cooled via contact with a large aluminum block to await re-measurement. Finally, to eliminate bias in the weight due to buoyancy the final weights of the films,  $m_2$ , were measured once the samples reached the initial measurement temperature. The final mass of the oil film was then given by,

$$m_f = m_2 - m_o \quad (4-2)$$

with the evaporated mass of the oil film being,

$$m_{evap} = m_f - m_i = m_2 - m_1 \quad (4-3)$$

During the measurement process, gravity caused each sample to settle into an approximately even film, excepting a meniscus around the inset edge; pre-heating within the evaporation test section also contributed to this due to the reduction in viscosity with temperature [53]. Additionally, the MSE125P remained in the same location for the entirety of the study and in a separate room from the blower and other apparatus to minimize vibrations.

Prior to any calibrations or measurements the blower was allowed to run for 1 hour at its operating frequency (20 Hz) with the flow conditioning valve open so that the system could reach a stable operating temperature (and blower output). Similarly, post-calibration the heating block and evaporation test section were allowed to heat to the required base temperature with flow conditioner open for at least 1 hour. In addition, the ambient temperature of the scale room where each weight measurement was conducted remained at  $19 \pm 2^\circ\text{C}$ , which is similar to the air temperature at the test section inlet since both the blower and room were supplied by the same dedicated air conditioning unit.

Each evaporation measurement was conducted for an initial film temperature,  $T_f$ , of  $150 \pm 2.5^\circ\text{C}$ , which is typical of regions nearer to TDC on the cylinder liner at high engine loads [4, 5, 22]. Measurements for each forced convection case were conducted for  $t = 0, 25, 50,$  and  $150$  s, where  $t = 0$  s is the point at which airflow begins after heating. Although the oil species are stable at low temperatures ( $< 90^\circ\text{C}$ ) [5], evaporation occurred during preheating from the ambient temperature to  $T_f$ . This initial mass loss during heating,  $m_{evap,t=0}$ , was established for each case naturally by performing measurements for  $t = 0$ . However, the evaporation results in the following section are presented corrected such that  $m'_{evap,t=0} = 0$ :

$$m'_{evap} = m_{evap} - m_{evap,t=0} \quad (4-4)$$

The prime is omitted from the notation in the next section. The maximum time exceeds common exposure times within IC engines (e.g. 30 ms at 2000 RPM) but was necessary to vaporize a significant amount of liquid and produce reliable estimations of evaporation rates. In addition, a relatively high film thickness (50  $\mu\text{m}$  versus 5  $\mu\text{m}$ ) mitigates the difference in diffusion times compared to engine timings. An average film thickness of 50  $\mu\text{m}$  was chosen for all experiments based on the repeatability of the balance, corresponding to a volume of 31.25  $\text{mm}^3$  (26.14 mg) within the film holder inset. Consequently, the film mass was constrained to  $26.64 \pm 0.5$  mg during preparation. Table 4-3 below summarizes the boundary layer conditions chosen from among the characterizations described in §3.6. For each set of conditions, each evaporation experiment was repeated five times to prevent possible outliers and reduce random errors in the reported data. Five measurements was deemed an appropriate compromise

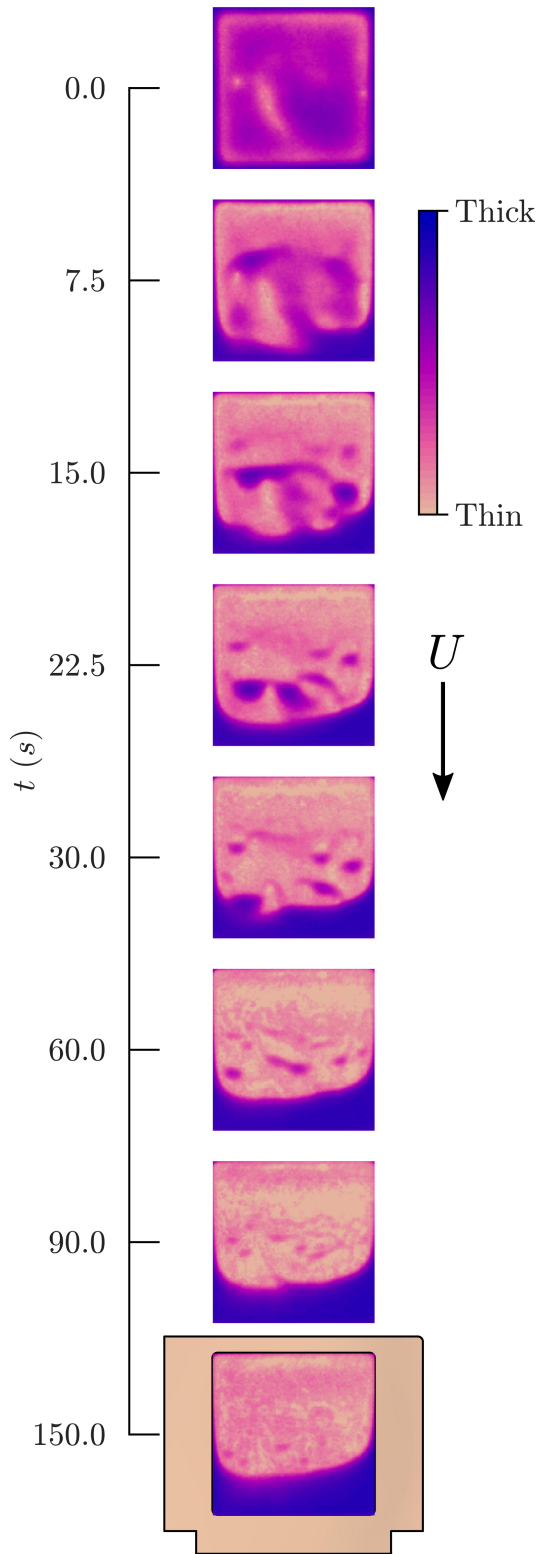
between accuracy and time based on an extended study of 10 measurements producing similar repeatability for the Baseline,  $Re_{D_h} = 1.0 \times 10^4$  case.

The results of the calibrations for each set of conditions are also summarized in Table 4-1, including the heater base temperature and preheat time. Infrared (IR) imaging of the sample holder was used to both measure the temperature variation at the sample holder inset surface and visualize the oil film motion as it shears under airflow. An optris® PI 640 camera (640 × 120 pixels, 32 Hz) was used to capture the required radiometric data. Due to the reflective properties of copper a clone of the sample holder was coated in an emissive, high-temperature paint to provide surfaces with consistent emissivity and low reflectance. The emissivity of the surface ( $\epsilon = 0.85$ ) was determined by mounting a surface thermocouple and matching the measured temperature to the PI 640 measurements. Figure 4-2 demonstrates the experimental setup (Figure 4-2b) used to image the sample holder, with the camera oriented above the test section with the top and borosilicate glass window removed due to its absorption in the IR spectrum.

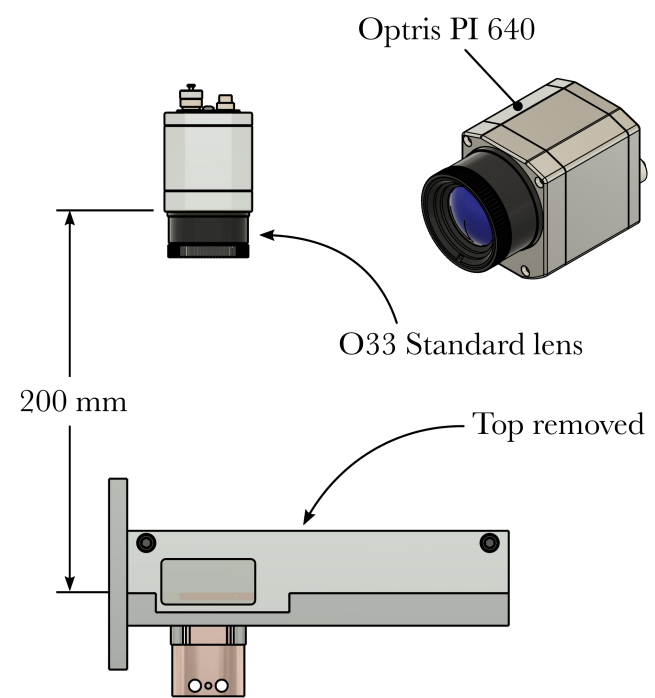
**Table 4-1. Experimental conditions for film evaporation measurements.**

$x/a$	Inlet Case	$Re_{D_h}$	$T_b$ (°C)	$t_o$ (s)	$m_{evap,t=0}$ ( $10^{-4}$ kg/m <sup>2</sup> )
2	Baseline	10,650 ( $1.0 \times 10^4$ )	194	60	2.72
		17,750 ( $1.7 \times 10^4$ )	208	50	2.72
		35,500 ( $3.5 \times 10^4$ )	216	40	2.72
45	Grid 1	17,750	204	45	2.40
	Grid 2	17,750	204	45	2.40
	Grid 3	10,650	194	55	2.88
		17,750	204	45	2.40
	Baseline	10,650	188	56	1.76
		17,750	209	42	2.24

a) Film thickness change under airflow.



b) Experimental setup for infrared imaging.



c) Surface temperature distribution of inset.

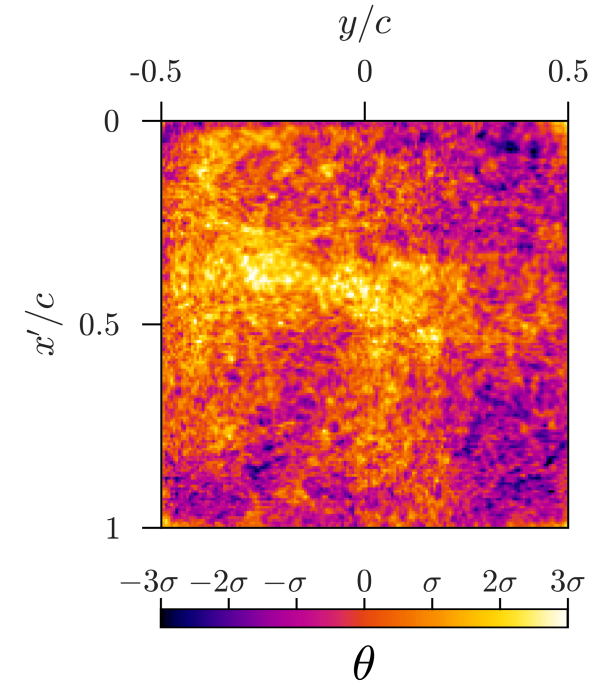


Figure 4-2. IR measurements demonstrating a) the change in film thickness with time, b) the associated experimental setup, and c) temperature distribution over the sample holder inset for  $\bar{T} = 150^{\circ}\text{C}$  ( $\sigma = 1.1^{\circ}\text{C}$ ).

Figure 4-2a shows a visualization of the oil film under the Baseline,  $Re_{D_h} = 1.0 \times 10^4$  condition. Due to variation in the film surface, the reflectance/transmissivity of the liquid oil, and small differences in surface temperature, the IR data reveals the changes in surface profile as the oil shears over the maximum measurement duration. This is a qualitative, while typical, measure of the film thickness with time, with the thicker regions coloured in blue. Initially, a thicker region of oil is found within a meniscus at the film edge while a thinner region is present at the centre of the holder. As the film shears under airflow it begins to pool at the downstream edge of the inset, with significant surface deformations reflected in the images (Figure 4-2a). It can be inferred from the results that the scale and magnitude of surface waves subside progressively as the film thickness reduces over the majority of the surface, with the main film volume collected in the aft part of the holder.

Finally, Figure 4-2c demonstrates the even temperature distribution of the clean inset at steady-state without airflow. The inset surface was imaged with the PI 640 at its minimum measurement distance (200 mm) with its standard  $33^\circ \times 25^\circ$  lens ( $f = 18.7$  mm), resulting in a  $125 \times 125$  pixel image where each pixel represents a temperature measurement. Once an average, steady-state temperature of  $\bar{T} = 150^\circ\text{C}$  was reached 150 measurements were gathered at 32 Hz. The resulting time-averaged temperature field is shown in Figure 4-2c, shown in the form of an excess temperature,

$$\theta_{i,j} = \langle T \rangle_{i,j} - \bar{T} \quad (4-5)$$

where  $i$  and  $j$  represent pixel locations in the  $x$  and  $y$  locations respectively and  $\langle T \rangle_{i,j}$  represents the time-averaged temperature at each location. The mean temperature is in turn given by,

$$\bar{T} = \frac{\sum_i^n \sum_j^m \langle T \rangle_{i,j}}{nm} \quad (4-6)$$

with a standard deviation of  $\sigma = 1.1^\circ\text{C}$ . The distribution shows that the majority of the sample holder lies within  $\pm 2\sigma = 2.2^\circ\text{C}$ , while the accuracy of the PI 640 is reported to be  $\pm 2^\circ\text{C}$ .

## 4.2 Evaporation Results

In this section, the results of the oil film evaporation measurements are presented. Specifically, the evaporation is compared and contrasted with respect to the flow characterization for each measurement case detailed in the foregoing section, including evaporation at ambient conditions under natural convection. The effects of Reynolds number, near-wall turbulence intensity, flow regime, and boundary layer shape are discussed.

The evaporated masses with time for each case listed in Table 4-1 are shown in Figure 4-3. Furthermore, a full tabulated list of the evaporation results may be found in Appendix D. Firstly, vaporization under free convection (natural convection) at 150°C ( $Gr_c = 3,838$ ) was completed to provide a baseline for the oil film evaporation measurements. Figure 4-3a shows the resulting evaporation within  $t = 0 - 600$  s. An approximately linear evaporation rate with time is observed, with  $\dot{m}_n = 3.06 \times 10^{-6}$  kg m<sup>-2</sup> s<sup>-1</sup>. This is expected given the low evaporation rate, where species concentrations within the film will not decrease substantially such that the mass transport is limited by liquid-phase diffusion, or dominated by heavier hydrocarbons with lower vapour pressures [71]. A similar linear regression is performed to approximate the evaporation rate for each other evaporation case in Figure 4-3. An increase with Reynolds number is evident for the Baseline cases (Figure 4-3b – 4-3d). This trend is mimicked by the Grid cases (Figure 4-3e – 4-3h) and downstream baseline cases (Figure 4-3i and 4-3j). Little variation is evident in the evaporation between Grid and Baseline cases for  $Re_{D_h} = 10,650$  and 17,750. Error bars are present in Figure 4-3 and subsequent figures which denotes  $\pm\sigma$ , which is the standard deviation of the mass measurements. The error bars tend to be smaller than the symbology used.

Comparisons of evaporation results with respect to their boundary layer conditions are presented in Figures 4-4 – 4-7. In each case, the evaporation and airflow results are presented non-dimensionally to assess the relative effects of different parameters. The exposure times ( $t$ ) are scaled by the characteristic velocity ( $U$ ), and film length ( $c$ ), representing exposure in terms of mean transit across the inset length. For duct flows,  $U$  is equivalent to the centreline velocity. The evaporated mass ( $m_{\text{evap}}$ ) is given with respect to the initial film mass ( $m_i$ ) for contextual purposes, as the initial film masses are within  $26.64 \pm 0.5$  mg. The boundary layer profiles

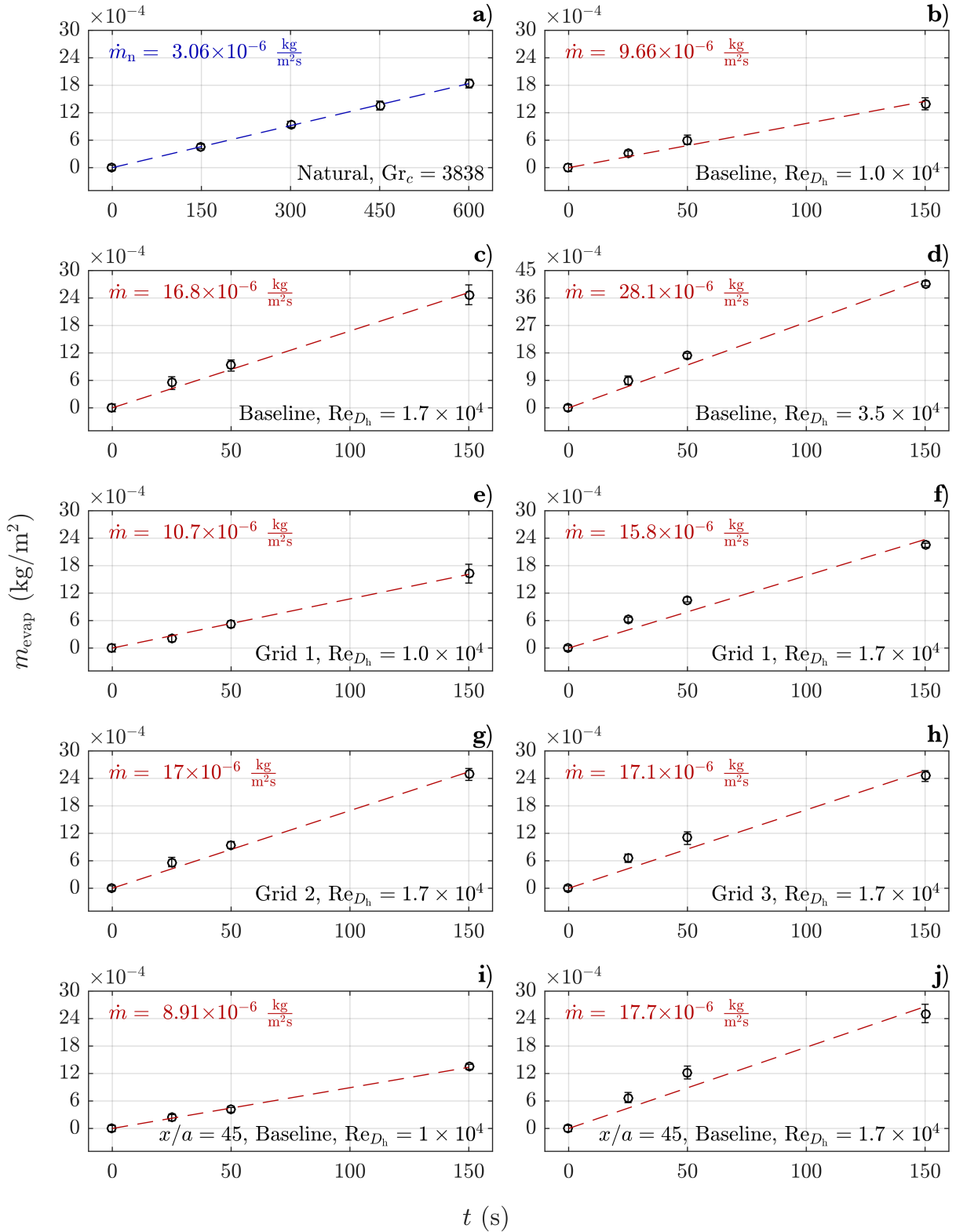


**Figure 4-3. Evaporation results and estimated evaporation rates for oil films initially at 50  $\mu\text{m}$  and held at 150°C for each airflow case, including the natural evaporation case.**



velocities are scaled with respect to ( $U$ ), while the wall-normal distance ( $y$ ) is scaled by both the tunnel height ( $a$ ) and the displacement thickness ( $\delta^*$ ). The exposure time is also scaled by  $\delta^*$  in addition to  $c$ , with both the mass and velocity  $\delta^*$  scaling shown inset in their respective subfigures. Theoretically, laminar boundary layers in two-dimensional flow have similar shape when scaled by the  $\delta^*$ , described by the Blasius laminar boundary layer solution (Appendix A). Comparison to the Blasius profile allows evaluation of the boundary layer shape, and so it is included as a solid black line in the inset of each velocity subfigure. The exposure time scaled by  $\delta^*$  ( $U/\delta^*$ ) is relatable to the shearing rate within the boundary layer and is therefore proportionate to the shearing rate within the film ( $\sim \langle u_{f,o} \rangle / \langle h_f \rangle$ ) for laminar boundary layers. The same velocity scalings are used in a similar fashion for the presented turbulence statistics ( $u_{\text{rms}}$ ) in Figures 4-5 – 4-7 and the PIV results in Appendix C.

A comparison of the evaporated masses under laminar boundary layers with similar thicknesses serves to demonstrate the effect of shear velocity on the film evaporation. Figure 4-4 provides this comparison, showing the evaporation data (Figure 4-4a) and boundary layer profiles (Figure 4-4b) for each case under the Baseline inlet condition at the upstream location,  $x/a = 2$ . In this case the boundary layers are obviously laminar, demonstrated by each profile collapsing to the Blasius profile (Figure 4-4b). The results in Figure 4-4a show a collapse of the scaled evaporated masses, implying a dependence on  $U$ . This also reflects the increase in evaporation rate with increasing  $U$  and  $\text{Re}_{D_h}$  demonstrated in Figure 4-3b – 4-3d. Here, an increase in  $U$  is associated with a proportional increase in the local wall shear stress (and shear velocity) due to the laminar nature of the boundary layers. This trend matches with the results of Reijnhart and Rose [69], where the evaporation rate of a single component liquid phase increased with increasing shear velocity under turbulent flow.

A different comparison between boundary layer cases with differing levels of near-wall turbulence intensity demonstrates its effect on the film evaporation. This is shown in Figures 4-5 and 4-6, which show thin boundary layer cases at the upstream location ( $x/a = 2$ ) with varying turbulence intensity maxima due to the wire-meshes (Grids) present at the inlet [25]. Firstly, Figure 4-5 shows a comparison between the evaporation data (Figure 4-5a) and boundary layer profiles (Figure 4-5b and 4-5c) for the Baseline and Grid 3,  $\text{Re}_{D_h} = 10,650$  cases. Some perturbations in the core velocity profile are evident for the single Grid case (Figure

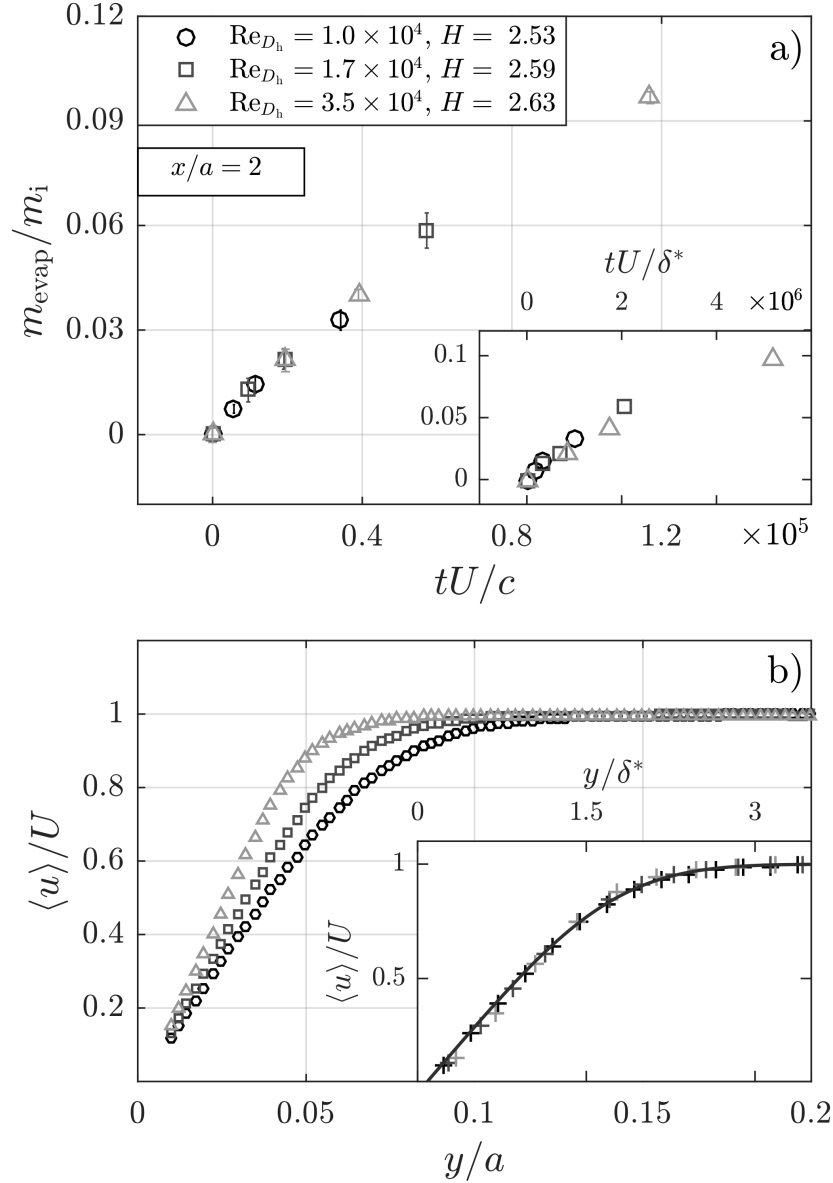


**Figure 4-4. Comparison of Baseline,  $Re_{D_h} = 10,650, 17,750,$  and  $35,500$  evaporation cases at  $x/a = 2$ . Showing a) film evaporation and b) velocity profiles. Subfigures show same properties with relevant parameters scaled by  $\delta^*$ . Solid black line in b) denotes the Blasius laminar boundary layer.**

4-5a) due to the proximity of the wire mesh, and so the core velocity  $U$  is estimated as an average in the core flow region for each Grid case. This estimation is also used in the scaling of Figure 4-6 and elsewhere. Despite the difference in  $u_{rms}$  profiles (maximum of 13% vs. 1.5% for the Baseline case), Figure 4-5a shows no significant differences in the evaporation between the Baseline and Grid cases (relative to the measurement uncertainty). This is possibly due to the similarity in  $\delta^*$  and  $U$  between the two cases, with the mass transfer being dependent primarily

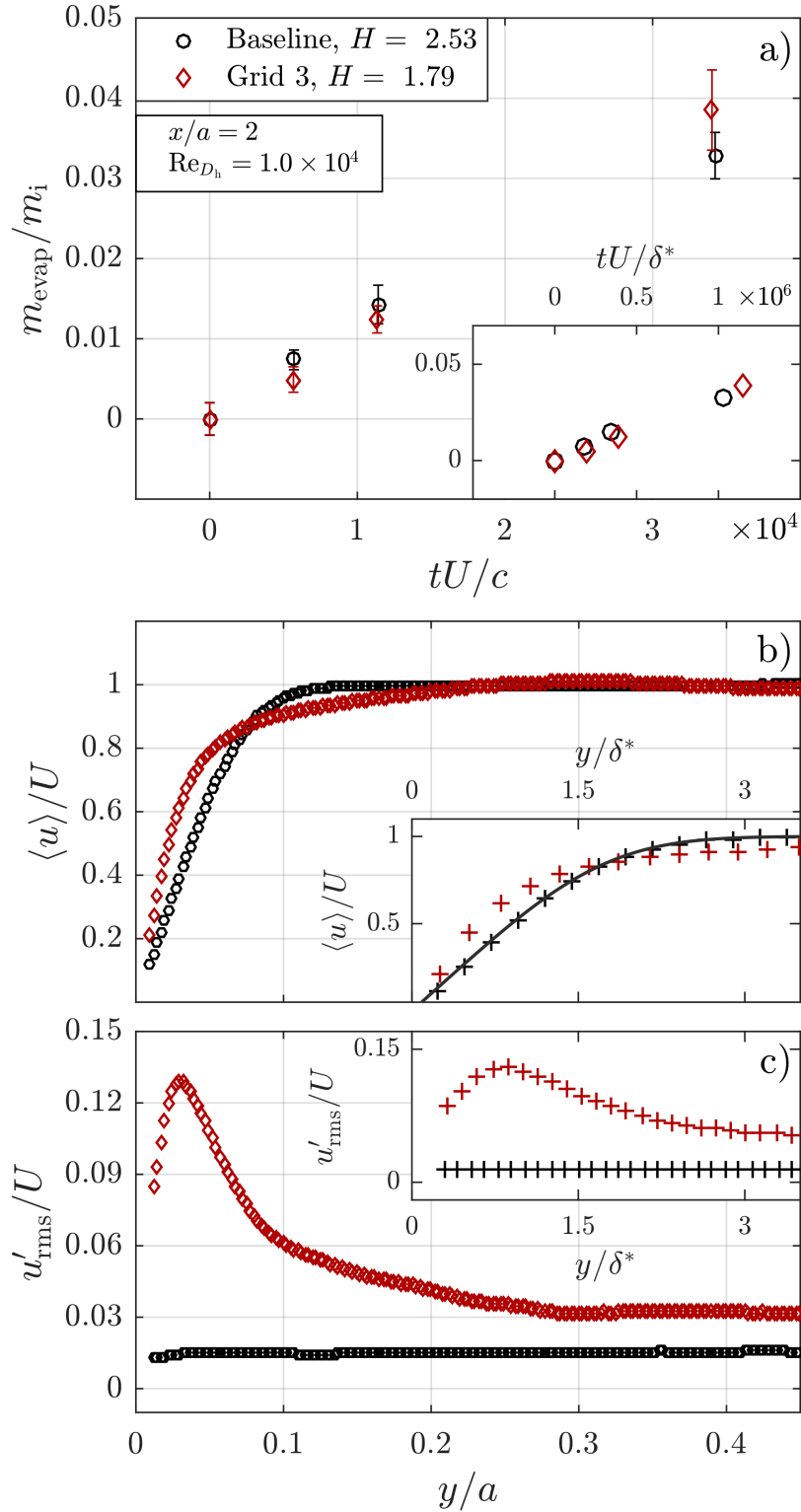


Figure 4-5. Comparison of Baseline and Grid 3 cases for  $\text{Re}_{D_h} = 10,650$  at  $x/a = 2$ . Showing a) film evaporation, b) velocity profiles, and c) turbulence intensities.

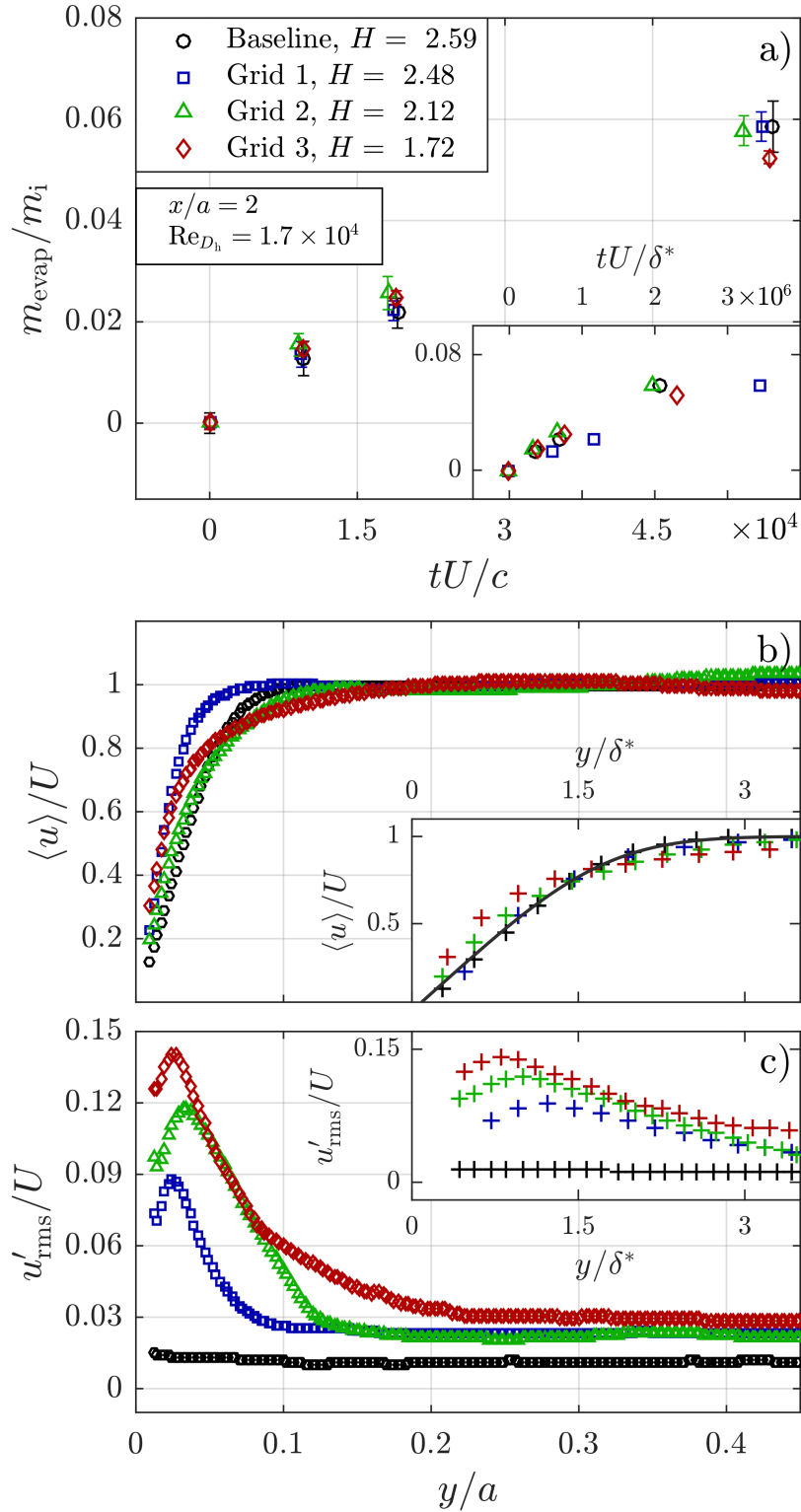


Figure 4-6. Comparison of Baseline and Grid 1 – 3 cases for  $Re_{D_h} = 17,750$  at  $x/a = 2$ . Showing a) film evaporation, b) velocity profiles, and c) turbulence intensities.

on the mean wall shear as in Figure 4-4. Therefore, a significant increase in flow fluctuations produces a minimal impact on the gas-phase mass transport in the entrance region as long as the mean boundary layer characteristics are not remarkably different.

This trend is also evident in Figure 4-6, which displays similar conditions of varying near-wall turbulence for  $Re_{D_h} = 17,750$ . Here, each of the three Grid cases are considered. Similar to the  $Re_{D_h} = 10,650$  case, no significant change in evaporation is evident despite notably higher near-wall  $u_{rms}$  (9%, 12%, and 14% maxima for Grids 1 – 3 respectively). Again, this implies that the level of velocity fluctuations in the boundary layer plays a less significant role compared to the mean boundary layer characteristics. Based on the results in Figures 4-5 and 4-6 it is likely that the influence of near-wall turbulence can be neglected when modelling convective mass transfer from the evaporating oil film surface for similar length scales.

The dominant effect of mean boundary layer characteristics are demonstrated further through comparison between the thin upstream ( $x/a = 2$ ) boundary layers and more developed, downstream ( $x/a = 45$ ) boundary layers. Figure 4-7 presents a comparison between the Baseline,  $Re_{D_h} = 10,650$  and  $17,750$  cases at  $x/a = 45$ , where the  $Re_{D_h} = 17,750$  case has transitioned (see Figure 4-7b inset) and generated significant near wall turbulence (Figure 4-7c). Concurrently, the  $Re_{D_h} = 10,650$  case has remained laminar yet increased in thickness. As in Figure 4-3 and 4-4, notably higher evaporation rate is seen for the  $Re_{D_h} = 17,750$  case. A similar evaporation rate under  $\delta^*$  time scaling (Figure 4-7a inset) is demonstrated in both cases. However, the nondimensional evaporation rate based on  $\delta^*$  is higher than in the upstream laminar cases shown in Figure 4-4a or the turbulent cases shown in Figures 4-5a and 4-6a by approximately 100% (0.06 versus 0.03). This implies that similarity in this scaling is dependent on displacement thickness (which is greater in Figure 4-7), and therefore that the evaporation over the discrete samples is dependent primarily on Reynolds number and mean wall shear (which is ill-described by  $\delta^*$  in thick, turbulent boundary layers).

The dependence on bulk flow properties over the length of the film is demonstrated further by Figure 4-8, which summarizes the effects of flow parameters on film evaporation. In both Figure 4-8a and 4-8b the forced convection evaporation rates ( $\dot{m}_f$ ) from Figures 4-3b – 4-3i are scaled by the natural convection evaporation rate ( $\dot{m}_n$ ) derived from the data in Figure 4-3a.

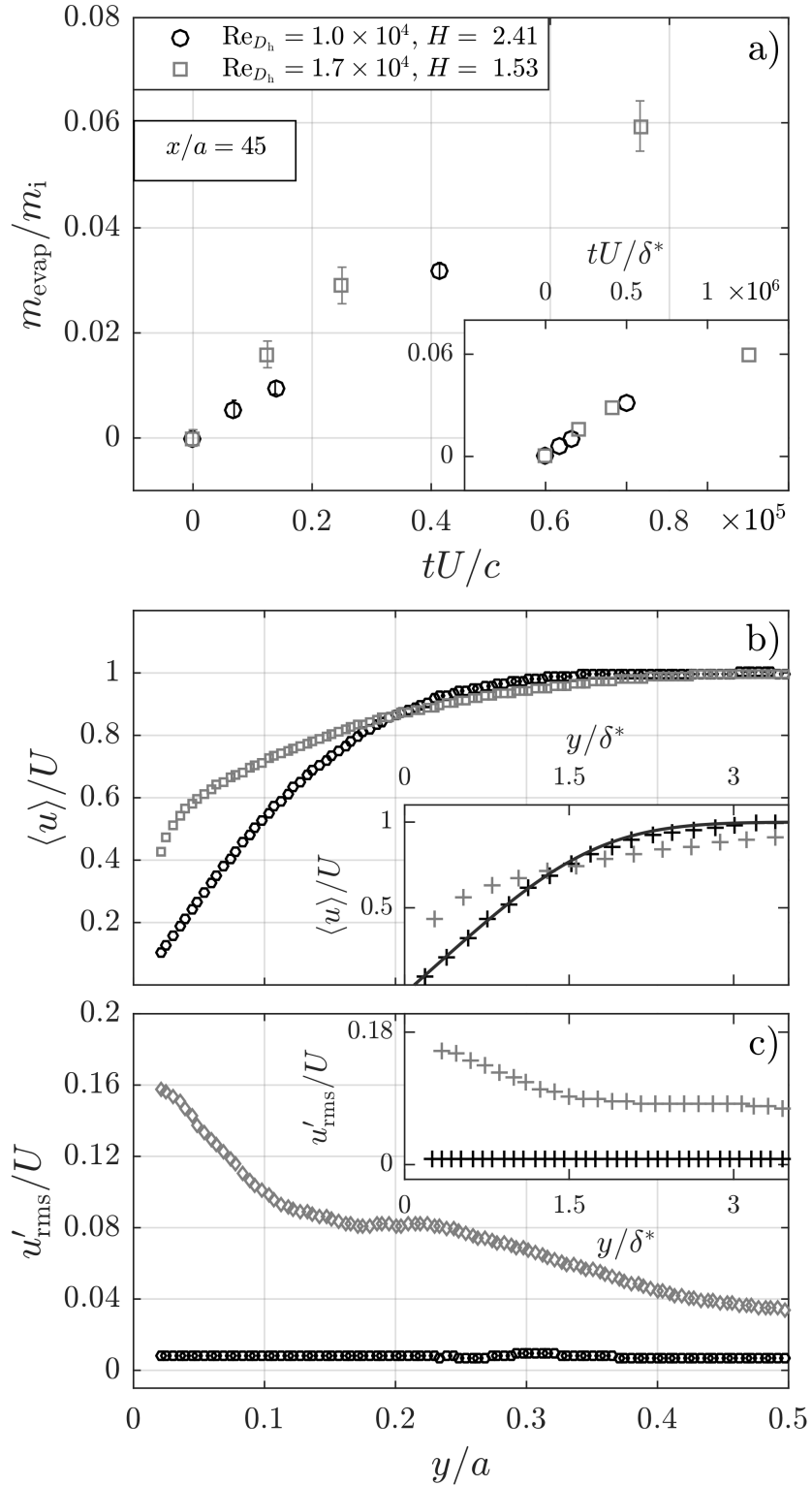


**Figure 4-7. Comparison of Baseline,  $Re_{D_h} = 10,650$  and  $17,750$  cases at  $x/a = 45$ . Showing a) film evaporation, b) velocity profiles, and c) turbulence intensities.**

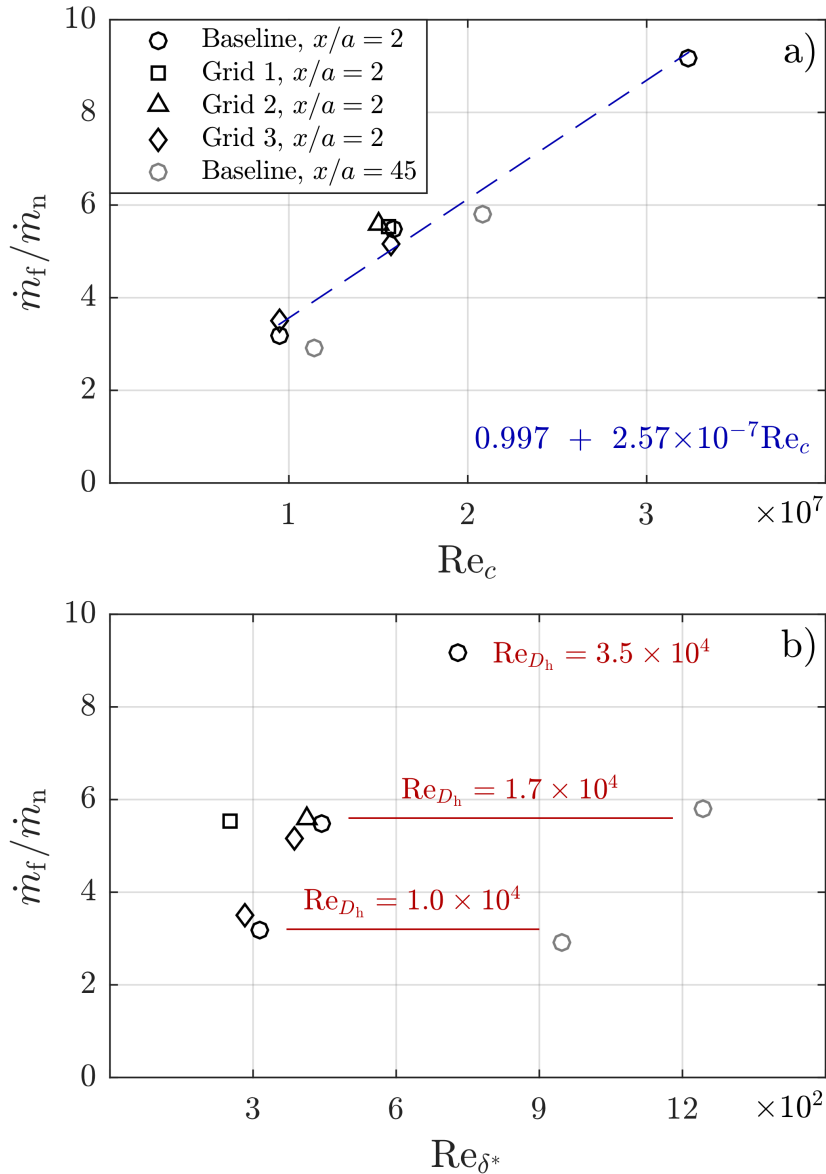


**Figure 4-8. Evaporation rates from linear regression of forced convection data ( $\dot{m}_f$ ) relative to natural evaporation rate ( $\dot{m}_n$ ). Shown with respect to a)  $Re_c$  and b)  $Re_{\delta^*}$  for each Baseline and Grid case.**

In Figure 4-8a the evaporation rates are plotted with respect to Reynolds number based on the film length ( $Re_c$ ) which is the characteristic length based on the film area. As expected, the evaporation rate increases with  $Re_c$ , approximately decreasing towards  $\dot{m}_n$  as  $Re_c$  approaches zero. Conversely, in Figure 4-8b, the relative evaporation rates are plotted with respect to the Reynolds number based on the local boundary layer displacement thickness ( $Re_{\delta^*}$ ). In this case, the downstream cases have significantly different behaviour compared to the upstream cases, as

in Figure 4-7. The results in Figure 4-8a highlight the prominent dependence of the evaporation rate on bulk flow parameters ( $Re_{D_h}$ ) or mean wall shear for the appropriate length scales.

These results agree with the similarity of evaporation rates observed earlier, where those rates are well defined with respect to convective time scales based on length scales and characteristic velocities (inset in Figure 4-4a) which better describe the wall shear stress. For turbulent flows, this is likely the velocity gradient within the laminar sublayer ( $y^+ = yu_\tau/\nu < 5$ ), as opposed to the displacement thickness. This is further supported by the apparently negligible effect of turbulence above the film. The thinness of the concentration boundary layer over the short, discrete samples is likely the culprit for these cases: once diffusion through the sublayer has proceeded it is expected the near-wall turbulence will encourage the convective mass transfer of hydrocarbons from the film. Therefore, for the length scales and conditions studied, it is likely the effect of gas phase transport on the evaporation may be restricted to the viscous sublayer.



## 5 Conclusions

In this study the evaporation of thin, liquid oil films was investigated experimentally. The oil films 50  $\mu\text{m}$  in thickness were raised to an elevated temperature of 150°C and subjected to constant temperature evaporation under laminar and turbulent boundary layers. Oil films which are deposited onto a cylinder liner by the compression ring as a piston reciprocates are subjected to similar conditions; the goal of this study was to evaluate the effects different boundary layer parameters have on the evaporation under representative circumstances.

Characterization of boundary layer flows within a duct ( $2a \times a$ ) was completed successfully through a combination of PIV and hot-wire measurements. Several sets of boundary layer conditions were chosen therein, for  $\text{Re}_{D_h} = 10,650, 17,750, \text{ and } 35,500$ . Three different inlet turbulence conditions were also employed which varied the initial levels of turbulence within the boundary layers. Evaporation measurements were conducted for two separate locations within the duct ( $x/a = 2$  and 45) to take advantage of the boundary layer development and high inlet turbulence. This allowed comparison between laminar, turbulent, and transitional boundary layers of similar and different thicknesses. PIV measurements at both the upstream and downstream locations showed that the boundary layers remain predominantly two-dimensional (negligible variation in  $z$ ) across the film inset with little variation in the axial direction due to the inset's short length. Additionally, the fully-developed, turbulent boundary layers at the downstream location were found to abide by the law of the wall.

The evaporation of the oil hydrocarbons was found to be highly dependent on bulk Reynolds number, and demonstrated a linear increase in evaporation with velocity. The evaporation rate was also found to not depend directly on the boundary layer shape, but rather on the mean wall shear based on comparison between thin and developed boundary layers. Near-wall turbulence intensity (maxima of 1.5%, 9%, 12%, 14%, and 16%) were found to have negligible impact on the evaporation rate for the length scales studied. Consequently, it was concluded that when modelling cylinder liner evaporation under similar conditions the effect of convective mass transfer on the evaporation may be restricted to the laminar sublayer.

A wind tunnel was designed to provide a quiet, uniform airflow source at the inlet of the test section. Hot-wire measurements at the outlet of the contraction showed that the settling chamber and contraction were operating adequately, with mean streamwise velocity  $\langle u \rangle / U$  remaining within 1% of the centreline velocity ( $U$ ) for 90% of the test section height ( $x$ - $y$  plane,  $z = 0$ ) for the lowest  $\text{Re}_{D_h}$  case. Likewise, no instabilities or noise indicative of separation within the flow conditioner components was detected for the  $\text{Re}_{D_h}$  range considered. The baseline inlet turbulence intensity remained less than 2% for each  $\text{Re}_{D_h}$  case.

## 6 Future Work

The foregoing study presented conclusions with respect to the evaporation of thin, lubricant films that is by no means comprehensive. Specifically, the actual engine conditions which cylinder wall films are subjected to are highly transient, variable, and three-dimensional. Therefore, the following are some suggestions for future work which could follow this work.

Firstly, while this study considered flow tangent to a wall film it would be beneficial to experimentally study the effect of impinging jet flow on the film evaporation. This is synonymous to the flow from the intake valve which both generates a considerable amount of the in-cylinder turbulence and is incident on or near the hottest portion of the cylinder liner film.

Secondly, the foregoing experiments could be completed for both a longer film lengths ( $c$ ). This would allow for mass boundary layer growth. It is expected that the effect of turbulence would be evident for the mean evaporation for longer  $c$  where the concentration boundary layer significantly exceeds the laminar sublayer.

Thirdly, thinner initial film thicknesses ( $h_{f,i} \ll 10 \mu\text{m}$ ) could be considered for the same or higher Reynolds numbers ( $\text{Re}_{D_h}$ ). Where the rate of evaporation would be similar, this would allow for the depletion of species within the film and relatively significant changes in thickness with evaporation [73]. When combined with longer film lengths, a true study of boundary layer regulation could be conducted relative to the chosen hydrocarbon mixture. Where thinner films are considered, higher Reynolds numbers could also be considered more conveniently for discrete liquid samples (to avoid overflow under shear). Where the increase in  $c$  is not proportionate to the decrease in film thickness a more sensitive analytical microbalance would be required. Another method of measurement entirely could also be explored, if necessary.

Lastly, lubricants of vastly different viscosity and volatility could be considered under similar conditions. Where surrogate oils could be tailored with species of different, known molecular diffusivities, the above mass transfer conditions could be evaluated with respect to the individual components.

# References

- [1] Caines, A. J. and Haycock, R. F., 1996, *Automotive Lubricants Reference Book*, Society of Automotive Engineers Inc.
- [2] Yilmaz, E., 1997, “Sources and Characteristics of Oil Consumption in a Spark-Ignition Engine,” Ph. D dissertation, Massachusetts Institute of Technology, Cambridge, MA.
- [3] Spencer, A., Avan, Almqvist, A., E. Y., Dwyer-Joyce, R. S., and Larsson, R., 2013, “An experimental and numerical investigation of frictional losses and film thickness for four cylinder liner variants for a heavy duty diesel engine,” *Proc. IMechE Part J: J. Engineering Tribology*, 227(12), pp. 1319 – 1333
- [4] Yilmaz, E., Tian, T., Wong, V. W., and Heywood, J. B., 2002, “An Experimental and Theoretical Study of the Contribution of Oil Evaporation to Oil Consumption,” SAE Technical Paper No. 2002-01-2684
- [5] Soejima, M., Harigaya, Y., Hamatake, T., and Wakuri, Y., 2017, “Study on Lubricating Oil Consumption from Evaporation of Oil-Film on Cylinder Wall for Diesel Engine,” *SAE Int. J. Fuels Lubr.*, 10(2), pp. 487 – 501
- [6] Lapuerta, M., Hernández, J. J., Ballesteros, R., and Durán, A., 2003, “Composition and size of diesel particulate emissions from a commercial European engine tested with present and future fuels,” *Proc. Instn Mech. Engrs*, 217(D), pp. 907 – 919
- [7] Brandenberger, S., Mohr, M., Grob, K., and Neukom, H. P., 2005, “Contribution of unburned lubricating oil and diesel fuel to particulate emission from passenger cars,” *Atmospheric Environment*, 39, pp. 6985 – 6994
- [8] Williams, P. T., Abbass, M. K., Andrews, G. E., and Bartle, K. D., 1989, “Diesel Particulate Emissions: The Role of Unburned Fuel,” *Combustion and Flame*, 75, pp. 1 – 24
- [9] Laurence, R. B., Wong, V. W., and Brown, A. J., 1996, “Effects of Lubrication System Parameters on Diesel Particulate Emission Characteristics,” SAE Technical Paper No. 960318
- [10] ASTM D5800-18, 2018, “Standard Test Method for Evaporation Loss of Lubricating Oils by the Noack Method”, ASTM International, West Conshohocken, PA
- [11] Tobias, H. J., Beving, D. E., Ziemann, Sakurai, H., Zuk, M., McMurry, P. H., Zarling, D., Waytulonis, R., and Kittelson, D. B., 2001, “Chemical Analysis of Diesel Engine Nanoparticles Using a Nano-DMA/ Thermal Desorption Particle Beam Mass Spectrometer,” *Environ. Sci. Technol.*, 35, pp. 2233 – 2243
- [12] Dowling, M., 1992, “The Impact of Oil Formulation on Emissions from Diesel Engines,” SAE Technical Paper No. 922198
- [13] Yilmaz, E., Tian, T., Wong, V. W., and Heywood, J. B., 2004, “The Contribution of Different Oil Consumption Sources to Total Oil Consumption in a Spark Ignition Engine,” SAE Technical Paper No. 2004-01-2909
- [14] Didot, F. E., Green, E., and Johnson, R. H., 1987, “Volatility and Oil Consumption of SAE 5W-30 Engine Oil,” SAE Technical Paper No. 872126

- [15] Carey, L. R., Roberts, D. C., and Shaub, H., 1989, “Factors Influencing Engine Oil Consumption in Today’s Automotive Engines,” SAE Technical Paper No. 892159
- [16] Manni, M., and Ciocci, G., 1992, “An Experimental Study of Oil Consumption in Gasoline Engines,” SAE Technical Paper No. 922374
- [17] ASTM D2887-16a, 2016, “Standard Test Method for Boiling Range Distribution of Petroleum Fractions by Gas Chromatography”, ASTM International, West Conshohocken, PA
- [18] Furuhashi, S., Hiruma, M., and Yoshida, H., 1981, “An Increase of Engine Oil Consumption at High Temperature of Piston and Cylinder” SAE Technical Paper No. 810976
- [19] Carey, V. P., 1992, *Liquid – Vapor Phase-Change Phenomena: An Introduction to the Thermophysics of Vaporization and Condensation Processes In Heat Transfer Equipment*, 1st ed., CRC Press
- [20] Harigaya, Y., Yamasuga, K., Suzuki, M., Iijima, N., Takiguchi, M., and Shimada, A., 2009, “The Effect of Oil Evaporation From the Cylinder Wall on Oil Consumption of a Gasoline Engine,” Proceedings of the ASME 2009 Internal Combustion Engine Division Fall Technical Conference, Lucerne, Switzerland, September 20 – 24, 2009, ASME Paper No. ICEF2009-14051, pp. 523 – 531
- [21] Zhang, J., Zhang, G., He, Z., Lin, J., and Liu, H., 2013, “Analysis of Oil Consumption in Cylinder of Diesel Engine for Optimization of Piston Rings,” Chinese Journal of Mechanical Engineering, 26(1), pp. 207 – 216
- [22] Liu, L., Tian, T., and Yilmaz, E., 2005, “Modelling Oil Evaporation From the Engine Cylinder Liner With Consideration of the Transport of Oil Species Along Liner,” Proceedings of World Tribology Conference III, Washington, D.C., September 12 – 16, 2005, ASME Paper No. WTC2005-63984, 2, pp. 579 – 580
- [23] Park, D., 2005, “The Influence of Different In-Cylinder Flows on Combustion in an SI Engine,” Ph.D. dissertation, University of Toronto, Toronto, ON
- [24] Amitay, M., Tuna, B. A., and Dell’Orso, H., 2016, “Identification and mitigation of TS waves using localized dynamic surface modification,” Physics of Fluids, 28(6), 064103
- [25] Tuna, B. A., Li, X., and Yarusevych, S., 2017, “Investigation of the Effect of Inlet Turbulence on Transitional Wall-Bounded Flows,” Proceedings of the ASME 2017 Fluids Engineering Division Summer Meeting, Waikoloa, Hawai’i, July 31 – August 3, 2017, ASME Paper No. FEDSM2017-69321
- [26] Patel, V. C., and Head, M. R., 1969, “Some observations on skin friction and velocity profiles in fully developed pipe and channel flows,” Journal of Fluid Mechanics, 38(1), pp. 181 – 201
- [27] Westerweel, J., Draad, A. A., Van der Hoeven, J. T., and Van Oord, J., 1996, “Measurement of fully developed turbulent pipe flow with digital particle image velocimetry,” Experiments in Fluids, 20(3), pp. 165 – 177
- [28] Hellström, L. H., Ganapathisubramani, B., and Smits, A. J., 2015 “The evolution of large-scale motions in turbulent pipe flow,” Journal of Fluid Mechanics, 779, pp. 701 – 715
- [29] Kim, J., Moin, P., and Moser, R., 1987, “Turbulence statistics in fully developed channel flow at low Reynolds number,” Journal of fluid mechanics, 177, pp. 133 – 166

- [30] Jiménez, J., Hoyas, S., Simens, M. P., and Mizuno, Y., 2010, “Turbulent boundary layers and channels at moderate Reynolds numbers,” *Journal of Fluid Mechanics*, 657, p. 335
- [31] El Khoury, G. K., Schlatter, P., Noorani, A., Fischer, P. F., Brethouwer, G., and Johansson, A. V., 2013, “Direct numerical simulation of turbulent pipe flow at moderately high Reynolds numbers,” *Flow, turbulence and combustion*, 91(3), pp. 475 – 495
- [32] McComas, S. T., 1967, “Hydrodynamic entrance lengths for ducts of arbitrary cross section,” *Journal of Basic Engineering*, 89(4), pp. 847 – 850
- [33] Shah, R. K., 1978, “A correlation for laminar hydrodynamic entry length solutions for circular and noncircular ducts,” *Journal of Fluids Engineering*, 100(2), pp. 177 – 179
- [34] Durst, F., Ray, S., Ünsal, B., and Bayoumi, O. A. 2005, “The development lengths of laminar pipe and channel flows,” *Journal of fluids engineering*, 127(6), pp. 1154 – 1160
- [35] Bergman, T. L., Lavine, A. S., Incropera, F. P., and DeWitt, D. P., 2011, *Fundamentals of Heat and Mass Transfer*, 8th ed., John Wiley and Sons
- [36] Darbyshire, A. G., and Mullin, T., 1995, “Transition to turbulence in constant-mass-flux pipe flow,” *Journal of Fluid Mechanics*, 289, pp. 83 – 114
- [37] Mullin, T., 2011, “Experimental studies of transition to turbulence in a pipe,” *Annual Review of Fluid Mechanics*, 43, pp. 1 – 24
- [38] Patel, R. P., 1974, “A note on fully developed turbulent flow down a circular pipe,” *The Aeronautical Journal*, Vol. 78, pp. 93 – 97
- [39] Barr, D. I. H., 1980, “Technical note. The transition from laminar to turbulent flow,” *Proceedings of the Institution of Civil Engineers*, 69(2), pp. 555 – 562
- [40] Klein, A., 1981, “Review: Turbulent Developing Pipe Flow,” *Journal of Fluids Engineering*, 103, pp. 243 – 249
- [41] Da Silva, D. F., and Moss, E. A., 1994, “The stability of pipe entrance flows subjected to axisymmetric disturbances,” *Journal of Fluids Engineering*, 116, pp. 61 – 65
- [42] Sharp, K. V., and Adrian, R. J., 2004, “Transition from laminar to turbulent flow in liquid filled micro tubes,” *Experiments in fluids*, 36(5), pp. 741 – 747
- [43] Zanon, E. S., Durst, F., Bayoumy, O., and Al-Salaymeh, A., 2007, “Wall skin friction and mean velocity profiles of fully developed turbulent pipe flows,” *Experimental Thermal and Fluid Science*, 32(1), pp. 249 – 261
- [44] Thomas, A. S., 1983, “The control of boundary-layer transition using a wave-superposition principle,” *Journal of Fluid Mechanics*, 137, pp. 233 – 250
- [45] Widmann, A., Kurz, A., Simon, B., Grundmann, S., and Tropea, C. (2013). “Characterization of the interaction between Tollmien-Schlichting waves and a DBD plasma actuator using phase-locked PIV,” In PIV13; 10th International Symposium on Particle Image Velocimetry, Delft, The Netherlands, July 1-3, 2013

- [46] Eckhardt, B., Schneider, T. M., Hof, B., and Westerweel, J., 2007, "Turbulence transition in pipe flow," *Annu. Rev. Fluid Mech.*, 39, pp. 447 – 468
- [47] Lee, Y., and Goel, K. C., 1972, "Free stream turbulence and transition in a circular duct," *Fluid machinery and fluidics*, pp. 11 – 20
- [48] Musker, A. J., 1979, "Explicit expression for the smooth wall velocity distribution in a turbulent boundary layer," *AIAA J.*, 17, pp. 655 – 657
- [49] Kendall, A., and Koochesfahani, M., 2008, "A method for estimating wall friction in turbulent wall-bounded flows," *Exp Fluids*, 40, pp. 773 – 780
- [50] Alharbi, A., 2010, "High Speed High Resolution Vector Field Measurements and Analysis of Boundary Layer Flows In An Internal Combustion Engine," Ph.D. dissertation, University of Michigan, Ann Arbor, MI.
- [51] Alharbi, A. and Sick, V., 2010, "Investigation of boundary layers in internal combustion engines using a hybrid algorithm of high speed micro-PIV and PTV," *Exp. Fluids*, 49, pp. 949 – 959
- [52] Hall, M. J. and Bracco, F. V., 1986, "Cycle-Resolved Velocity and Turbulence Measurements Near the Cylinder Wall of a Firing S.I. Engine," *SAE Transactions*, 95(6), pp. 526 – 539
- [53] Harigaya, Y., Suzuki, M., and Takiguchi, M., 2003, "Analysis of Oil Film Thickness and Heat Transfer on a Piston Ring of a Diesel Engine: Effect of Oil Film Temperature," *Journal of Engineering for Gas Turbines and Power*, 125, pp. 596 – 603
- [54] Dearlove, J. and Cheng, W. K., 1995, "Simultaneous Piston Ring Friction and Oil Film Thickness Measurements in a Reciprocating Test Rig," *SAE Technical Paper No. 952470*
- [55] Avan, E. Y., Spencer, A., Dwyer-Joyce, R. S., Almqvist, A., and Larsson, R., 2012, "Experimental and numerical investigations of oil film formation and friction in a piston ring – liner contact," *Proc. IMechE Part J: J. Engineering Tribology*, 227(2), pp. 126 – 140
- [56] Takiguchi, M., Nakayama, K., Furuhashi, S., and Yoshida, H., 1998, "Variation of Piston Ring Oil Film Thickness in an Internal Combustion Engine – Comparison Between Thrust and Anti-Thrust Sides," *SAE Technical Paper No. 980563*
- [57] Harigaya, Y., Suzuki, M., Toda, F., and Takiguchi, M., 2006, "Analysis of Oil Film Thickness and Heat Transfer on a Piston Ring of a Diesel Engine: Effect of Lubricant Viscosity," *Journal of Engineering for Gas Turbines and Power*, 128, pp. 685 – 693
- [58] Wittig, S., Himmelsbach, J., Noll, B., Feld, H. J., and Samenfink, W., 1992, "Motion and Evaporation of Shear-Driven Liquid Films in Turbulent Gases," *Journal of Engineering for Gas Turbines and Power*, 114, pp. 395 – 400
- [59] Himmelsbach, J., Noll, B., and Wittig, S., 1994, "Experimental and numerical studies of evaporating wavy fuel films in turbulent air flow," *Int. J. Heat Mass Transfer*, 37(8), pp. 1217 – 1226
- [60] Furuhashi, S., Asahi, C., and Hiruma, M., 1983, "Measurement of Piston Ring Oil Film Thickness in an Operating Engine," *ASLE Transactions*, 26(3), pp 325 – 332

- [61] Söchting, S. J., and Sherrington, I., 2009, "The effect of load and viscosity on the minimum operating oil film thickness of piston-rings in internal combustion engines," *Proc. IMechE Part J: J. Engineering Tribology*, 223, pp. 383 – 391
- [62] Schröppel, J. and Thiele, F., 1983, "On the calculation of momentum, heat, and mass transfer in laminar and turbulent boundary layer flows along a vaporizing liquid film," *Numerical Heat Transfer*, 6(4), 475 – 496
- [63] Kelly-Zion, P. L., Pursell, C. J., Booth, R. S., and VanTilburg, A. N., 2009, "Evaporation rates of pure hydrocarbon liquids under the influences of natural convection and diffusion," *International Journal of Heat and Mass Transfer*, 52, pp. 3305 – 3313
- [64] Pasquill, F., 1943, "Evaporation from a plane, free-liquid surface into a turbulent air stream," *Proc. R. Soc. Lond. A*, 182, pp. 75 – 95
- [65] Sutton, O. G., 1934, "Wind structure and evaporation in a turbulent atmosphere," *Proc. R. Soc. Lond. A*, 146, pp. 701 – 722
- [66] Davies, D. R. and Walters, T. S., 1952, "Further Experiments on Evaporation from Small, Saturated, Plane Areas into a Turbulent Boundary Layer," *Proc. Phys. Soc. B*, 65(8), pp. 640 – 645
- [67] Huang, C. H., 1997, "Pasquill's Influence: On the Evaporation from Various Liquids into the Atmosphere," *Journal of Applied Meteorology*, 36, pp. 1021 – 1026
- [68] Reijnhart, R., Pieper, J., and Toneman, L. H., 1980, "Vapour Cloud Dispersion and the Evaporation of Volatile Liquids in Atmospheric Wind Fields – I. Theoretical Model," *Atmospheric Environment*, 14, pp. 751 – 758
- [69] Reijnhart, R., and Rose, R., 1980, "Vapour Cloud Dispersion and the Evaporation of Volatile Liquids in Atmospheric Wind Fields – II. Wind Tunnel Experiments," *Atmospheric Environment*, 14, pp. 759 – 762
- [70] Okamoto, K., Watanabe, N., Hagimoto, Y., Miwa, K., and Ohtani, H., 2010, "Evaporation characteristics of multi-component liquid," *Journal of Loss Prevention in the Process Industries*, 23, pp. 89 – 97
- [71] Okamoto, K., Watanabe, N., Hagimoto, Y., Miwa, K., and Ohtani, H., 2009, "Changes in evaporation rate and vapor pressure of gasoline with progress of evaporation," *Fire Safety Journal*, 44, pp. 756 – 763
- [72] Mackay, D., and Matsugu, R. S., 1973, "Evaporation Rates of Liquid Hydrocarbon Spills on Land and Water," *The Canadian Journal of Chemical Engineering*, 51, pp. 434 – 439
- [73] Gerendas, M., and Wittig, S., 2001, "Experimental and Numerical Investigation on the Evaporation of Shear-Driven Multicomponent Liquid Wall Films," *Journal of Engineering for Gas Turbines and Power*, 123, pp. 580 – 588
- [74] Fingas, M. F., 1997, "Studies on the evaporation of crude oil and petroleum products: I. the relationship between evaporation rate and time," *Journal of Hazardous Materials*, 56, pp. 227 – 236
- [75] Fingas, M. F., 1997, "Studies on the evaporation of crude oil and petroleum products II. Boundary layer regulation," *Journal of Hazardous Materials*, 57, pp. 41 – 58
- [76] Fingas, M. F., 2004, "Modeling evaporation using models that are not boundary-layer regulated," *Journal of Hazardous Materials*, 107, pp. 27 – 36



- [77] Woschni, G., 1967, "A Universally Applicable Equation for the Instantaneous Heat Transfer Coefficient in the Internal Combustion Engine," SAE Technical Paper No. 670931
- [78] De Petris, C., Giglio, V., and Police, G., 1977 "A Mathematical Model of the Evaporation of the Oil Film Deposited on the Cylinder Surface of IC Engines," SAE Technical Paper No. 972920
- [79] Audette, W. E., Wong, V. W., 1999, "A Model for Estimating Oil Vaporization From The Cylinder Liner As A Contributing Mechanism to Engine Oil Consumption," SAE Technical Paper No. 1999-01-1520
- [80] Audette, W. E., 1999, "Estimation of Oil Consumption Due to In-Cylinder Vaporization in Internal Combustion Engines," MASC thesis, Ph. D dissertation, Massachusetts Institute of Technology, Cambridge, MA
- [81] O'Rourke, P. J. and Amsden, A. A., 1996, "A Particle Numerical Model for Wall Film Dynamics in Port-Injected Engines," SAE Technical Paper No. 961961
- [82] Foucart, H., Habchi, C., Le Coz, J. F., and Baritaud, T., 1998, "Development of a Three Dimensional Model of Wall Fuel Liquid Film for Internal Combustion Engines," SAE Technical Paper No. 980133
- [83] Wahiduzzaman, S., Keribar, R., Dursunkaya, Z., and Kelley, F., 1992, "A Model for Evaporative Consumption of Lubricating Oil in Reciprocating Engines," SAE Technical Paper No. 922202
- [84] Mehta, R. D. and Bradshaw, P., 1979, "Design rules for small low speed wind tunnels," *The Aeronautical Journal of the Royal Aeronautical Society*, 83(827), pp. 443 – 453
- [85] Cattafesta, L., Bahr, C., and Mathew, J., 2010, "Fundamentals of Wind-Tunnel Design," *Encyclopedia of Aerospace Engineering*, John Wiley and Sons
- [86] Mehta, R. D., 1977, "The Aerodynamic Design of Blower Tunnels With Wide Angle Diffusers," *Prog. Aerospace Sci.*, 18, pp. 59 – 120
- [87] Morel, T., 1975, "Comprehensive Design of Axisymmetric Wind Tunnel Contractions," *ASME Journal of Fluids Engineering*, 97(2), pp. 225 – 233
- [88] Morel, T., 1977, "Design of Two-Dimensional Wind Tunnel Contractions," *ASME Journal of Fluids Engineering*, 99(2), pp. 371 – 377
- [89] Su, Y., 1991, "Flow analysis and design of three-dimensional wind tunnel contractions," *AIAA Journal*, 29(11), pp. 1912 – 1920
- [90] Kulkarni, V., Sahoo, N., and Chavan, S. D., 2011, "Simulation of honeycomb – screen combinations for turbulence management in a subsonic wind tunnel," *Journal of Wind Engineering and Industrial Aerodynamics*, 99(1), pp. 37 – 45
- [91] Mehta, R. D. and Hoffmann, P. H., 1987, "Boundary layer two-dimensionality in wind tunnels," *Experiments in Fluids*, 5(5), pp. 358 – 360
- [92] Groth, J., and Johansson, A. V., 1988, "Turbulence reduction by screens," *Journal of Fluid Mechanics*, 197, pp. 139 – 155
- [93] Mehta, R. D., 1985, "Turbulent Boundary Layer Perturbed by a Screen," *AIAA Journal*, 23(9), pp. 1335 – 1342

- [94] Hancock, P. E., 1998, "Plane multiple screens in non-uniform flow, with particular application to wind tunnel settling chamber screens," *European Journal of Mechanics – B/Fluids*, 17(3), pp. 357 – 369
- [95] Miller, D. S., 1978, *Internal Flow Systems*, 1st ed., British Hydromechanics Research Association
- [96] Atligan, M., and Calvert, J. R., 1980, "Geometry of transition sections between ducts of equal area," *Journal of Wind Engineering and Industrial Aerodynamics*, 6(1 – 2), pp. 25 – 37
- [97] Farell, C., and Xia, L., 1990, "A note on the design of screen-filled wide-angle diffusers," *Journal of Wind Engineering and Industrial Aerodynamics*, 33(3), pp. 479 – 486
- [98] Ward-Smith, A. J., Lane, D. L., Reynolds, A. J., Sahin, B., and Shawe, D. J., 1991, "Flow regimes in wide-angle screened diffusers," *International Journal of Mechanical Sciences*, 33(1), pp. 41 – 54
- [99] Roach, P. E., 1987, "The generation of nearly isotropic turbulence by means of grids," *International Journal of Heat and Fluid Flow*, 8(2), pp. 82 – 92.
- [100] Sciacchitano, A., Neal, D. R., Smith, B. L., Warner, S. O., Vlachos, P. P., Wieneke, B., and Scarano, F., 2015, "Collaborative framework for PIV uncertainty quantification: comparative assessment of methods," *Measurement Science and Technology*, 26(7), 074004
- [101] Petukhov, B. S., 1970 "Heat Transfer and Friction in Turbulent Pipe Flow with Variable Physical Properties." In *Advances in Heat Transfer*, ed. T. F. Irvine and J. P. Hartnett, Vol. 6. New York: Academic Press

# Appendix A – Blasius Laminar Boundary Layer Solution

The following is a solution to the Navier-Stokes equations for two-dimensional, steady flow with constant fluid properties, given by:

$$\frac{\partial u}{\partial x} + \frac{\partial v}{\partial y} = 0 \quad (\text{A-1})$$

$$u \frac{\partial u}{\partial x} + v \frac{\partial u}{\partial y} = -\frac{1}{\rho} \frac{\partial p}{\partial x} + \nu \left( \frac{\partial^2 u}{\partial x^2} + \frac{\partial^2 u}{\partial y^2} \right) \quad (\text{A-2})$$

$$u \frac{\partial v}{\partial x} + v \frac{\partial v}{\partial y} = -\frac{1}{\rho} \frac{\partial p}{\partial y} + \nu \left( \frac{\partial^2 v}{\partial x^2} + \frac{\partial^2 v}{\partial y^2} \right) \quad (\text{A-3})$$

Observing that  $\delta/L \ll 1$ , where  $\delta$  is the boundary layer thickness and  $L$  is the dimension of the surface in the  $x$ -direction, equations A1 – A3 may be simplified to the following, respectively:

$$\frac{\partial u}{\partial x} + \frac{\partial v}{\partial y} = 0 \quad (\text{A-3})$$

$$u \frac{\partial u}{\partial x} + v \frac{\partial u}{\partial y} = u_\infty \frac{\partial u_\infty}{\partial x} + \nu \frac{\partial^2 u}{\partial y^2} \quad (\text{A-4})$$

$$\frac{\partial p}{\partial y} \cong 0 \quad (\text{A-5})$$

where  $u = u_\infty$  for  $y \geq \delta$ . For the case of flow over a flat plate, where  $u_\infty = \text{constant}$  and  $p_\infty = \text{constant}$ , a solution proceeds by assuming similarity of the following form,

$$\eta = \frac{y}{\sqrt{\frac{\nu x}{u_\infty}}} = \frac{y}{x} \sqrt{\text{Re}_x} \quad (\text{A-6})$$

and also by defining a “streamfunction”  $\psi$ , which satisfies:

$$u = \frac{\partial \psi}{\partial y} \quad (\text{A-7})$$

$$v = \frac{\partial \psi}{\partial x} \quad (\text{A-8})$$

The solution then proceeds by finding solutions for the functions  $G(x)$  and  $F(\eta)$  by separation of variables, which is a problem defined by:

$$\psi(x, \eta) = G(x)F(\eta) \quad (\text{A-9})$$

When the first solution is assumed to be  $G(x) = \sqrt{u_\infty \nu x}$ , the following solution results:

$$F' = \frac{\partial F}{\partial \eta} = \frac{u}{u_\infty} \quad (\text{A-10})$$

$$-v = \frac{\partial \psi}{\partial x} = \sqrt{\frac{u_\infty \nu}{x}} \left( \frac{F - \eta F'}{2} \right) \quad (\text{A-11})$$

$$\frac{\partial u}{\partial x} = - \left( \frac{u_\infty}{2x} \right) \eta F'' \quad (\text{A-12})$$

$$\frac{\partial u}{\partial y} = \sqrt{\frac{u_\infty^3}{\nu x}} F'' \quad (\text{A-13})$$

$$\frac{\partial^2 u}{\partial y^2} = \left( \frac{u_\infty^2}{\nu x} \right) F''' \quad (\text{A-14})$$

Finally, this yields the Blasius equation for flow over a flat plate from equation A4 and equations A10 – A14, given by,

$$F''' + \frac{1}{2} F F'' = 0 \quad (\text{A-15})$$

for the boundary conditions:

$$y = 0 : u = 0, v = 0 \longrightarrow \eta = 0 : F = 0, F' = 0 \quad (\text{A-15})$$

$$y = \infty : u = u_\infty \longrightarrow \eta = \infty : F' = 1 \quad (\text{A-16})$$

Equation A15 may then be solved numerically, notably resulting in the following:

$$\eta = 0 : F'' = 0.33206 \quad (\text{A-15})$$

$$\delta^* = 1.72 \sqrt{\frac{\nu x}{u_\infty}} \quad (\text{A-16})$$

$$\theta = 0.665 \sqrt{\frac{\nu x}{u_\infty}} \quad (\text{A-17})$$

$$H = \frac{\delta^*}{\theta} = 2.59 \quad (\text{A-18})$$

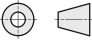
# Appendix B – Wind Tunnel Design Drawings

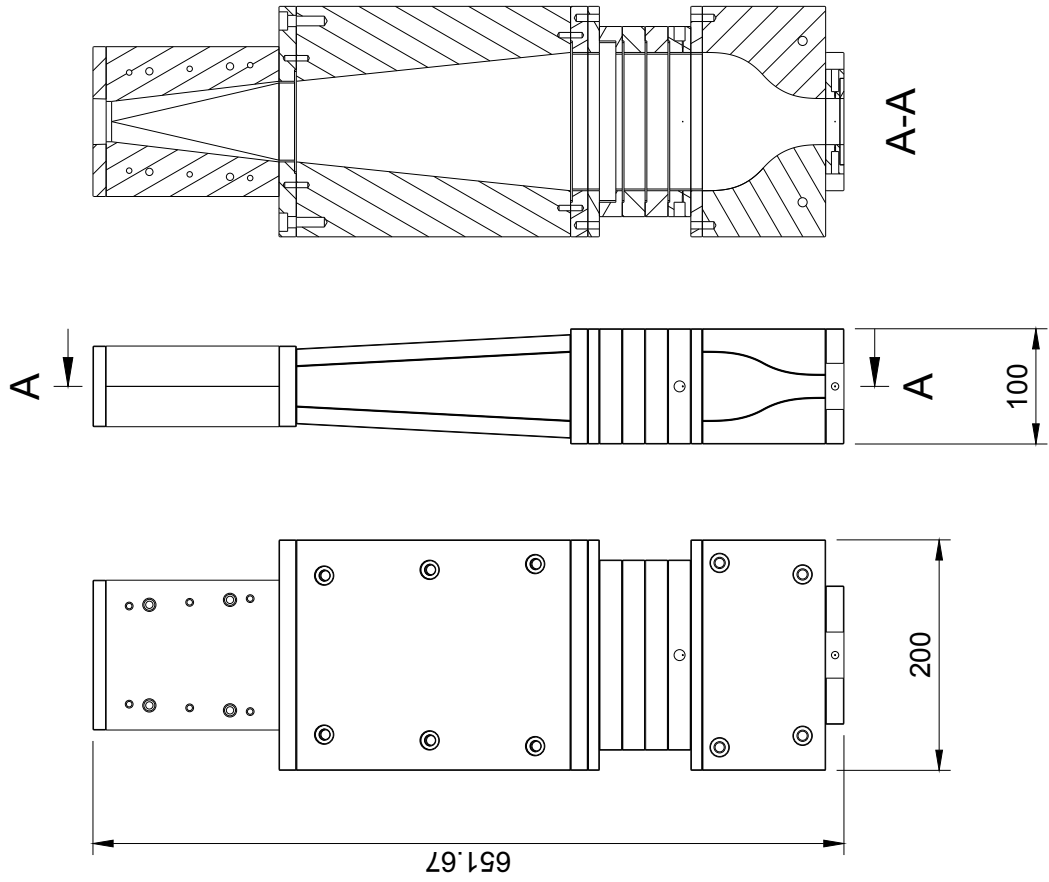
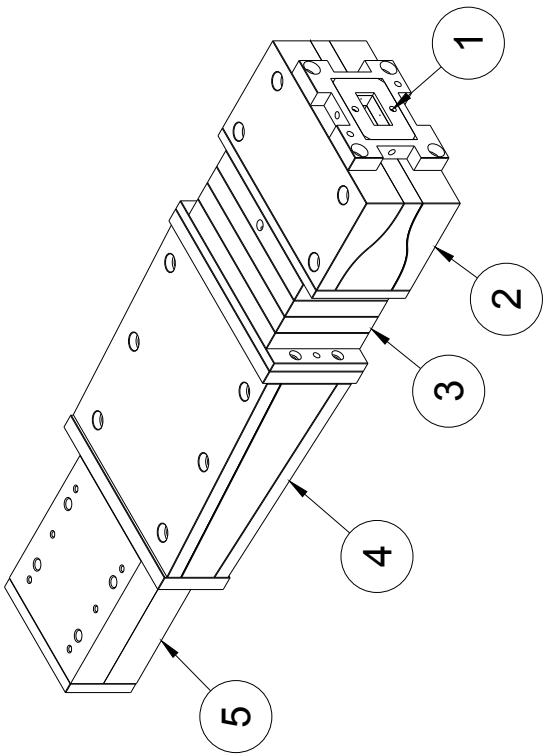
Below is a set of drawings describing the design of the wind tunnel used to produce the foregoing measurements. Critical dimensions are shown for each separate part along with the design diameters and depths for each hole. In general, the final geometry may differ due to changes made during machining. It is recommended that any modifications be made only after inspection of any related parts. The original CAD files are available upon request.

The drawings are subject to the following:

- i. Counterbored hole dimensions are shown for ideal dimensions. Clearances for standard socket-head cap screws were ensured during machining.
- ii. Any holes of the same diameter between parts are intended for stainless-steel alignment dowels with a ground finish. Tight, non-interference fits were ensured during machining.
- iii. Parts which are numbered the same may be rotated/flipped for assembly.
- iv. Additional alignment dowel holes were included at the machinist's discretion, and are not shown.

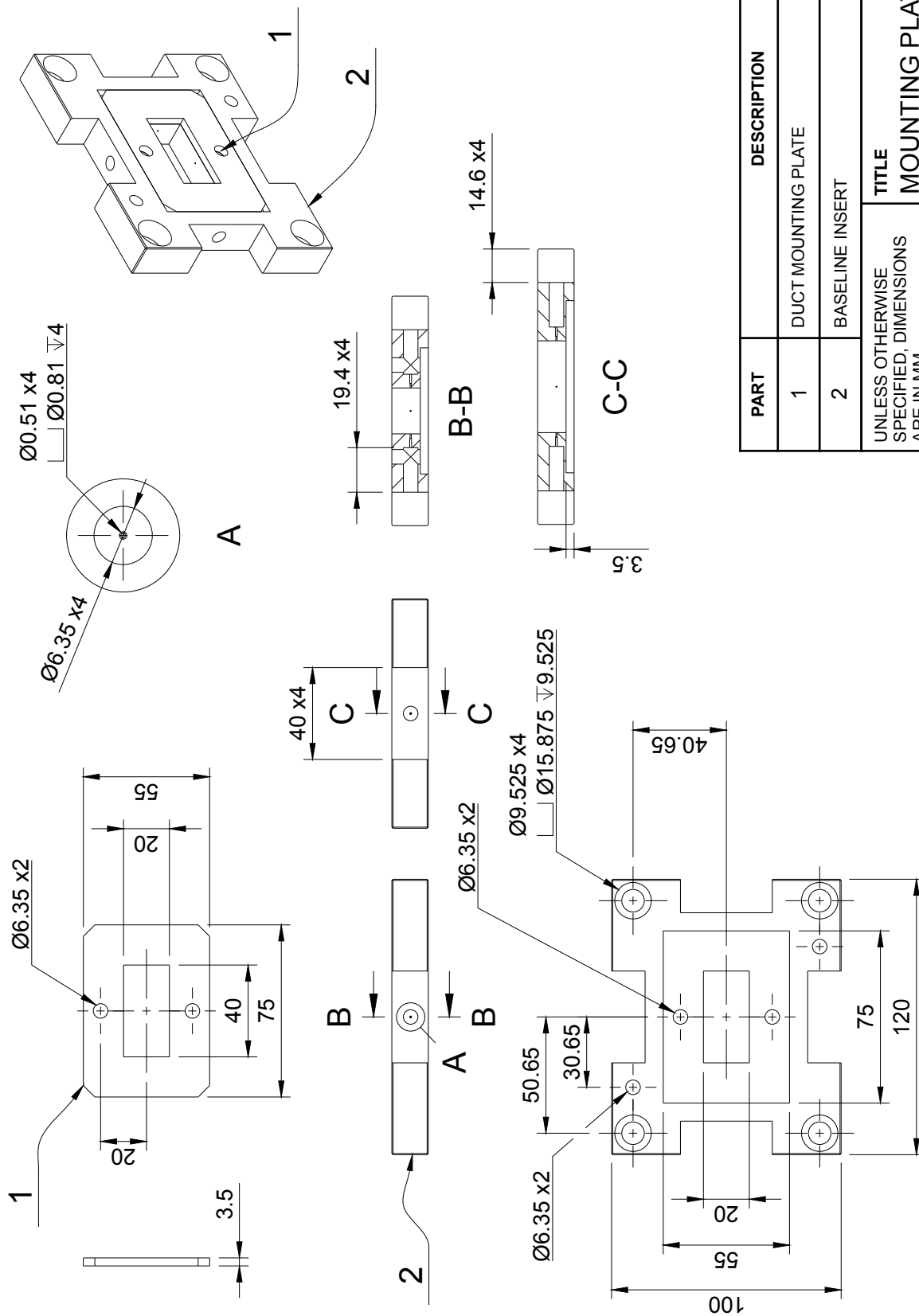
Some unfamiliar symbols may include:

- $\varnothing$       **Diameter**
- $\sqcup$       **Counterbore.** Following diameter and depth is for counterbore geometry.
- $\Downarrow$       **Depth.** Indicates a blind depth into a surface. When not shown for a hole callout, a through-hole can be assumed.
- TYP      **Typical dimension.** Indicates where a dimension is shared by similar geometry within the same drawing.
- XX.XX      **Theoretically Exact.** Design intent is for these dimensions to be exact to the precision shown.
-       **Third-Angle Projection.** Designates how projected views are shown with respect to a base view.



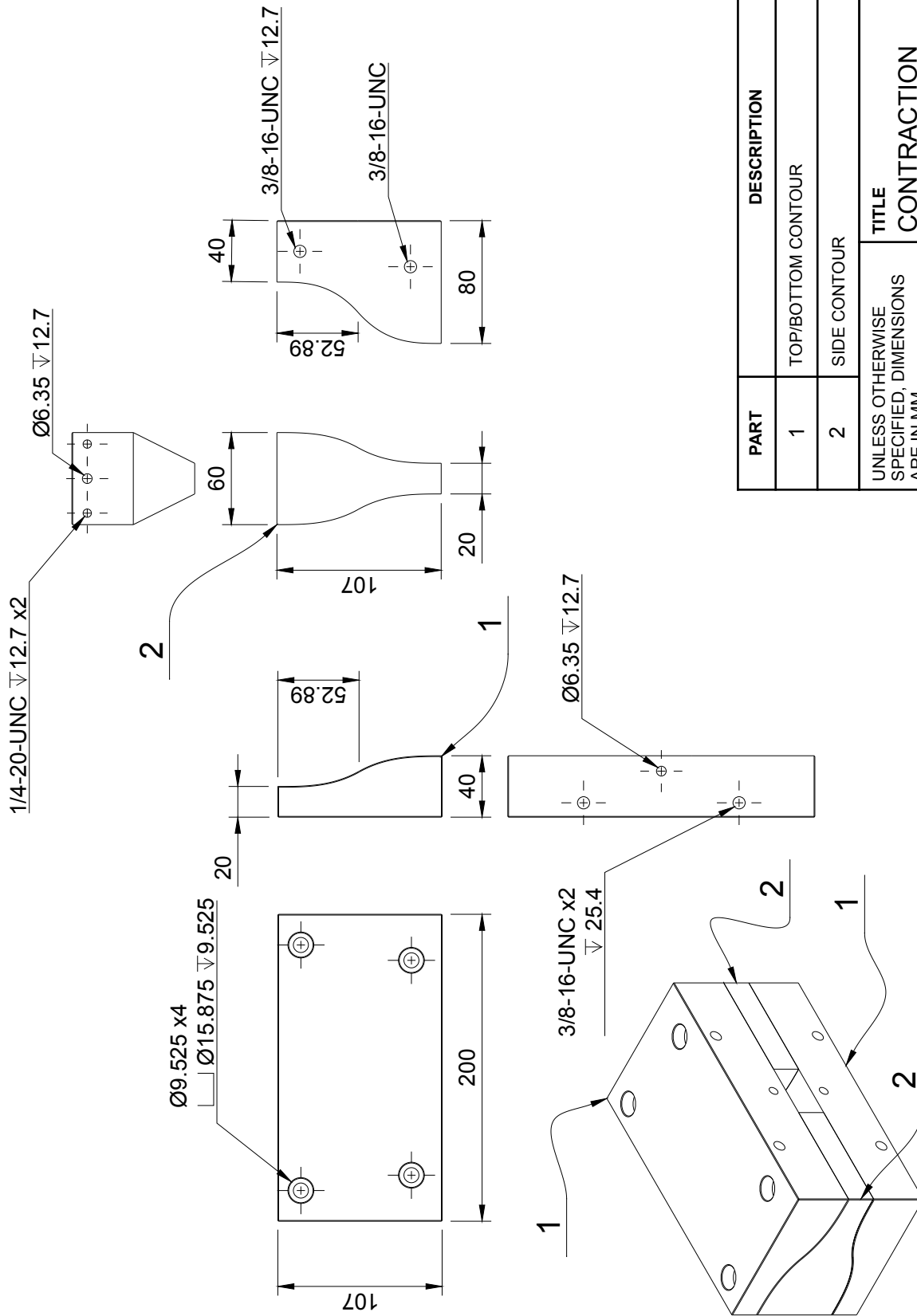
ASSY.	DESCRIPTION	TITLE	DRAWN	SHEET
1	DUCT MOUNTING PLATE	UNLESS OTHERWISE SPECIFIED, DIMENSIONS ARE IN MM. .xx ± 0.01 .xxx ± 0.01	S. J. GILL	1 OF 1
2	CONTRACTION			
3	SETTLING CHAMBER			
4	DIVERGING SECTION			
5	CIRCULAR — RECTANGULAR TRANSITION			
		ASSEMBLY		
		THIRD ANGLE PROJECTION		

Figure B-1. Drawing of wind tunnel settling chamber and component assemblies (assy.).



PART		DESCRIPTION
1	DUCT MOUNTING PLATE	
2	BASELINE INSERT	
UNLESS OTHERWISE SPECIFIED, DIMENSIONS ARE IN MM. .xx ± 0.01 .xxx ± 0.01		TITLE MOUNTING PLATE & INSERT
THIRD ANGLE PROJECTION		ASSEMBLY
		DUCT MOUNTING PLATE
DRAWN	S. J. GILL	SHEET 1 OF 1

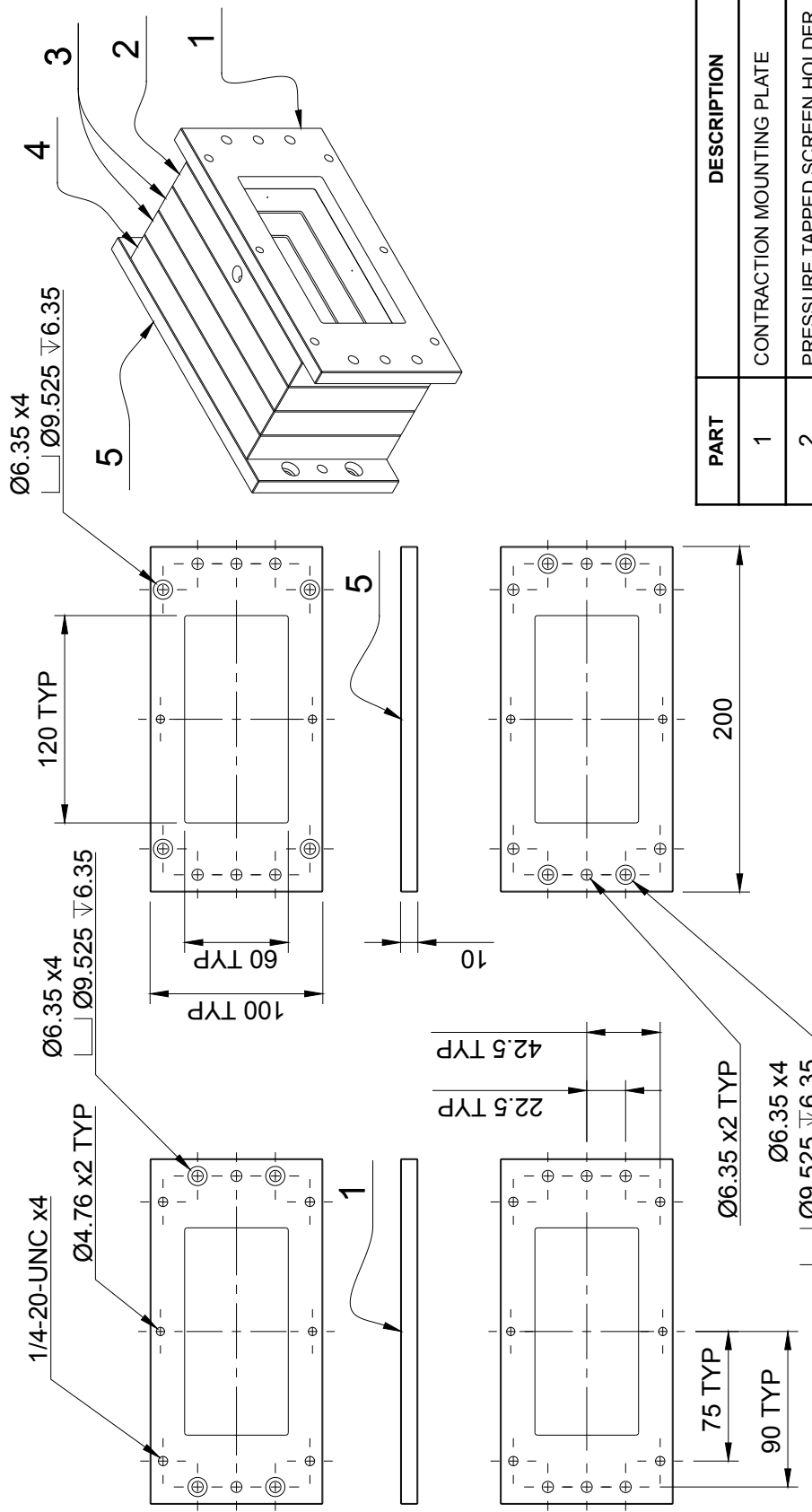
Figure B-2. Drawing of test section mounting plate and insert geometry.



PART		DESCRIPTION
1	TOP/BOTTOM CONTOUR	
2	SIDE CONTOUR	
UNLESS OTHERWISE SPECIFIED, DIMENSIONS ARE IN MM. .xx ± 0.01 .xxx ± 0.01		TITLE CONTRACTION CONTOUR SECTIONS
THIRD ANGLE PROJECTION		ASSEMBLY CONTRACTION
		DRAWN S. J. GILL
		SHEET 1 OF 1

Figure B-3. Drawing of top, bottom, and side contraction components.





PART	DESCRIPTION
1	CONTRACTION MOUNTING PLATE
2	PRESSURE TAPPED SCREEN HOLDER
3	SCREEN HOLDER
4	HONEYCOMB HOLDER
5	DIVERGING SECTION MOUNTING PLATE

TITLE	
MOUNTING PLATES	
ASSEMBLY	
SETTLING CHAMBER	
UNLESS OTHERWISE SPECIFIED, DIMENSIONS ARE IN MM. .xx ± 0.01 .xxx ± 0.01	THIRD ANGLE PROJECTION
DRAWN S. J. GILL	SHEET 1 OF 2

Figure B-4. Drawing of settling chamber mounting plates.

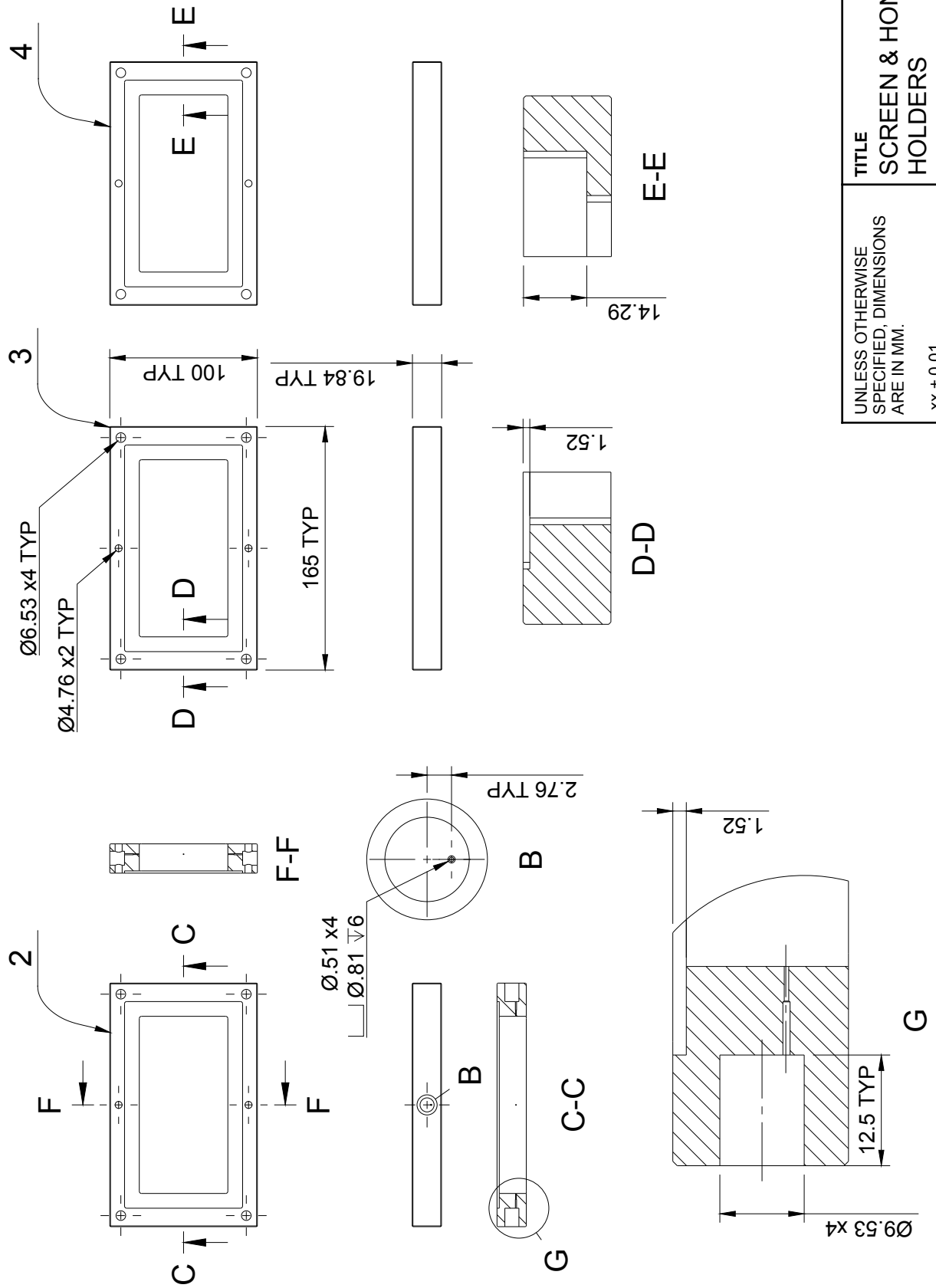
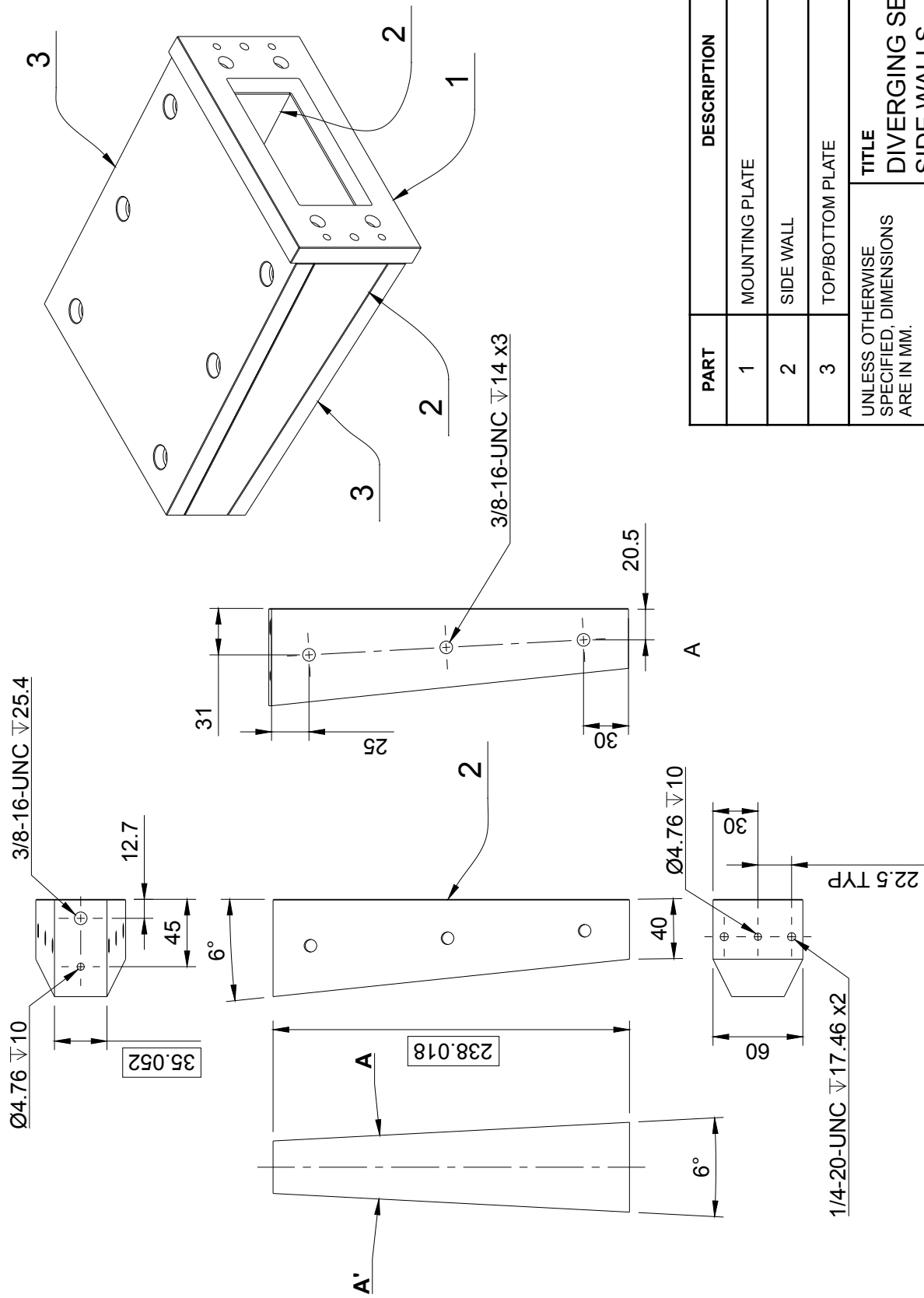


Figure B-5. Drawing of settling chamber screens and honeycomb holder.

UNLESS OTHERWISE SPECIFIED, DIMENSIONS ARE IN MM. .xx ± 0.01 .xxx ± 0.01	TITLE SCREEN & HONEYCOMB HOLDERS		THIRD ANGLE PROJECTION	DRAWN S. J. GILL	SHEET 2 OF 2
	ASSEMBLY SETTLING CHAMBER				



PART	DESCRIPTION
1	MOUNTING PLATE
2	SIDE WALL
3	TOP/BOTTOM PLATE
UNLESS OTHERWISE SPECIFIED, DIMENSIONS ARE IN MM. .xx ± 0.01 .xxx ± 0.01	
THIRD ANGLE PROJECTION	
TITLE DIVERGING SECTION SIDE WALLS	
ASSEMBLY DIVERGING SECTION	
DRAWN S. J. GILL	SHEET 1 OF 2

Figure B-6. Drawing of diverging section (diffuser) side wall components.





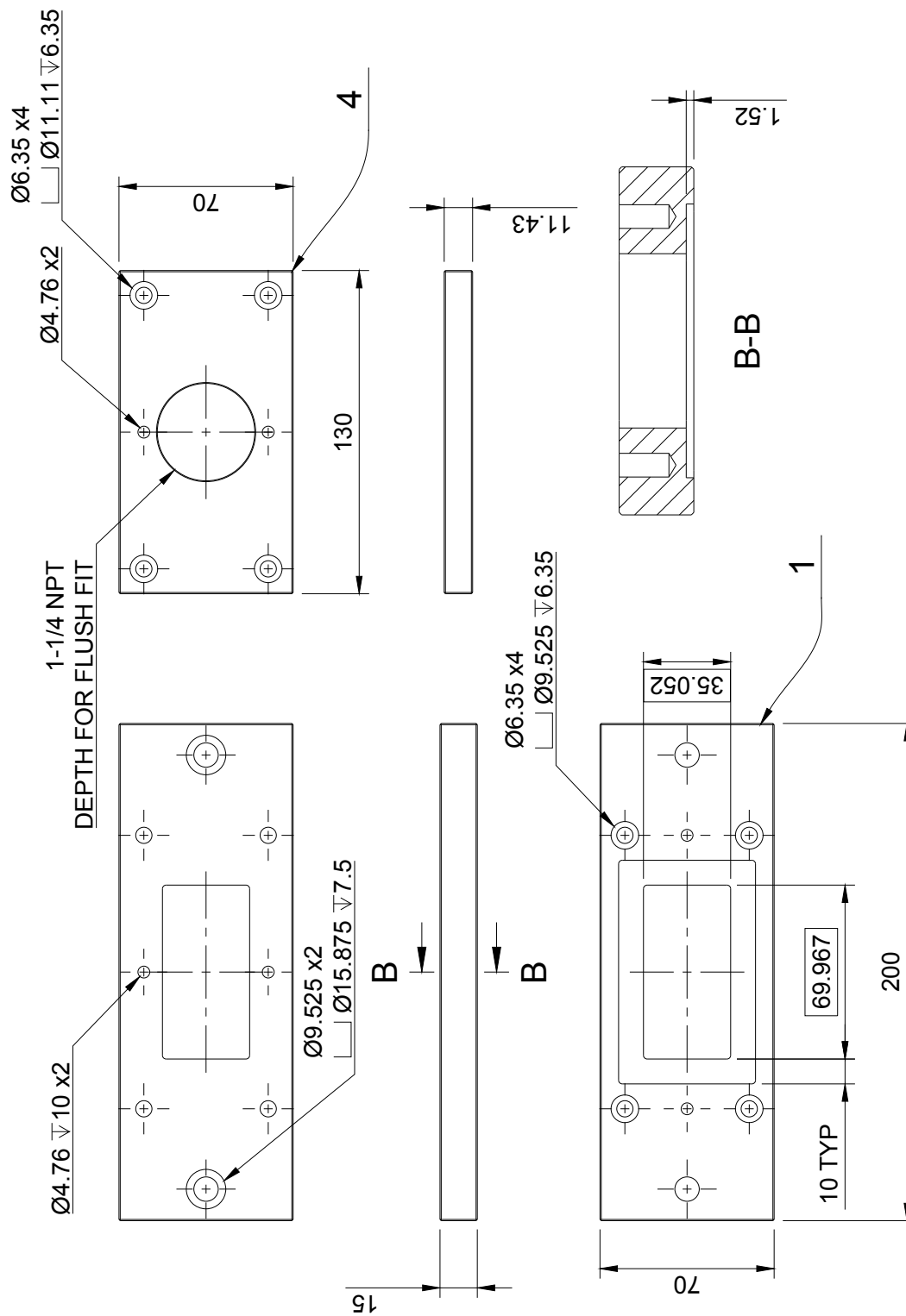


Figure B-9. Drawing of transition mounting plates.

UNLESS OTHERWISE SPECIFIED, DIMENSIONS ARE IN MM. .xx ± 0.01 .xxx ± 0.01	TITLE TRANSITION MOUNTING PLATES		DRAWN S. J. GILL	SHEET 2 OF 2
	ASSEMBLY CIRCULAR — RECTANGULAR TRANSITION			
THIRD ANGLE PROJECTION				

# Appendix C – Detailed Test Section Flow

A summary of the PIV measurements within the evaporation test section, detailed in §3.2 and §3.3.4, are presented in the Figures below. The entire dataset is available upon request. The PIV measurements in the  $x$ - $y$  plane for  $z/c = 0, 0.04, 0.08, 0.12, 0.16, 0.20, 0.24, 0.28, 0.32,$  and  $0.36$  were conducted for two overlapping FOVs. The region of overlap extends from  $0.38 \leq x'/c \leq 0.52$ . Within this region, the  $\langle u \rangle$  and  $u'_{\text{rms}}$  data is presented as an interpolation from one FOV to the other. In some cases, namely Figures C-5, C-6, C-10, and C-11, this produces a visible distortion in the flow near the boundary layer edge ( $\langle u \rangle/U \geq 0.9$ ). The flow outside the boundary layer in the Grid inlet cases ( $x/a = 2$ ) displays some non-uniformity due to the presence of the wire meshes, which is likely the cause of the differences between the FOVs.

In each b) and d) subfigure profiles for  $\langle u \rangle$  and  $u'_{\text{rms}}$  are presented at  $x'/c = 0.5$  for each  $z/c$  measurement plane. The following colour scheme is used to differentiate each  $z/c$  location:

**Table C-1. Colour scheme for  $z/c$  locations.**

$z/c$	0	0.04	0.08	0.12	0.16	0.20	0.24	0.28	0.32	0.36
Legend	●	●	●	●	●	●	●	●	●	●

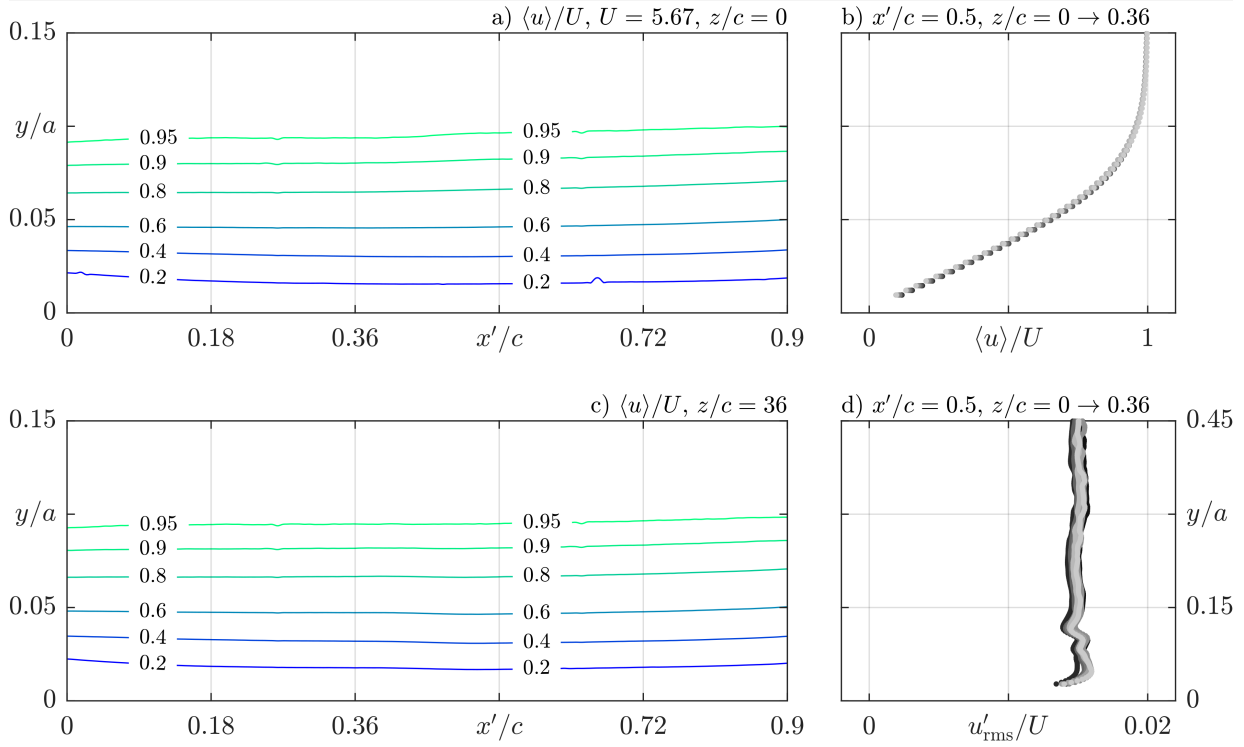


**Figure C-1. Summary of PIV measurements for Baseline,  $Re_{D_h} = 10,650$  case at  $x/a = 2$ .**

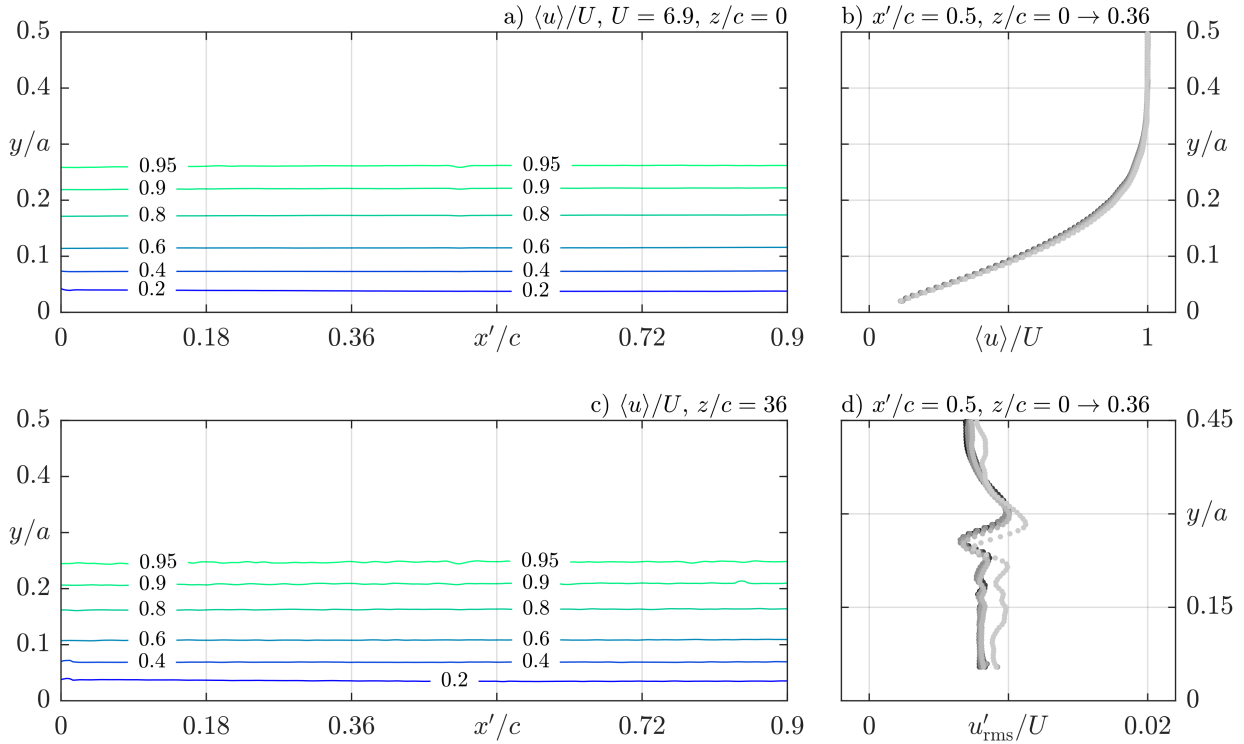


**Figure C-2. Summary of PIV measurements for Baseline,  $Re_{D_h} = 10,650$  case at  $x/a = 45$ .**



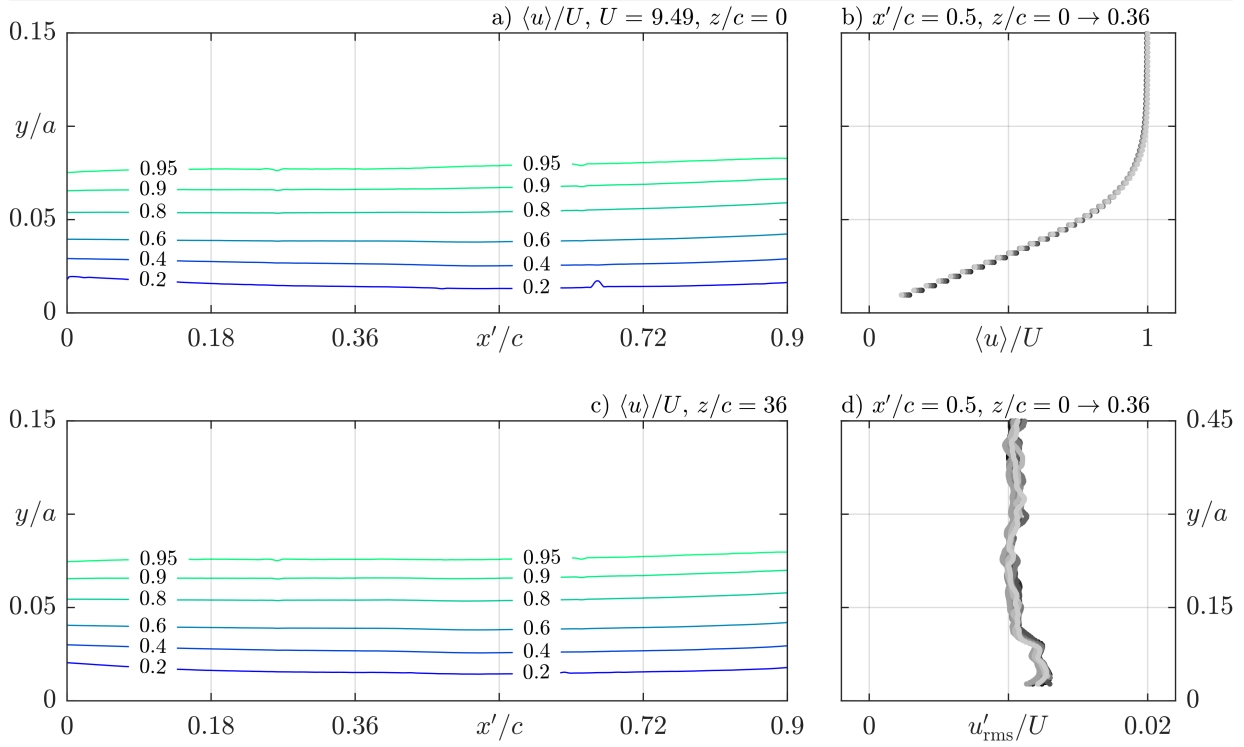


**Figure C-3. Summary of PIV measurements for Baseline,  $Re_{D_h} = 17,750$  case at  $x/a = 2$ .**

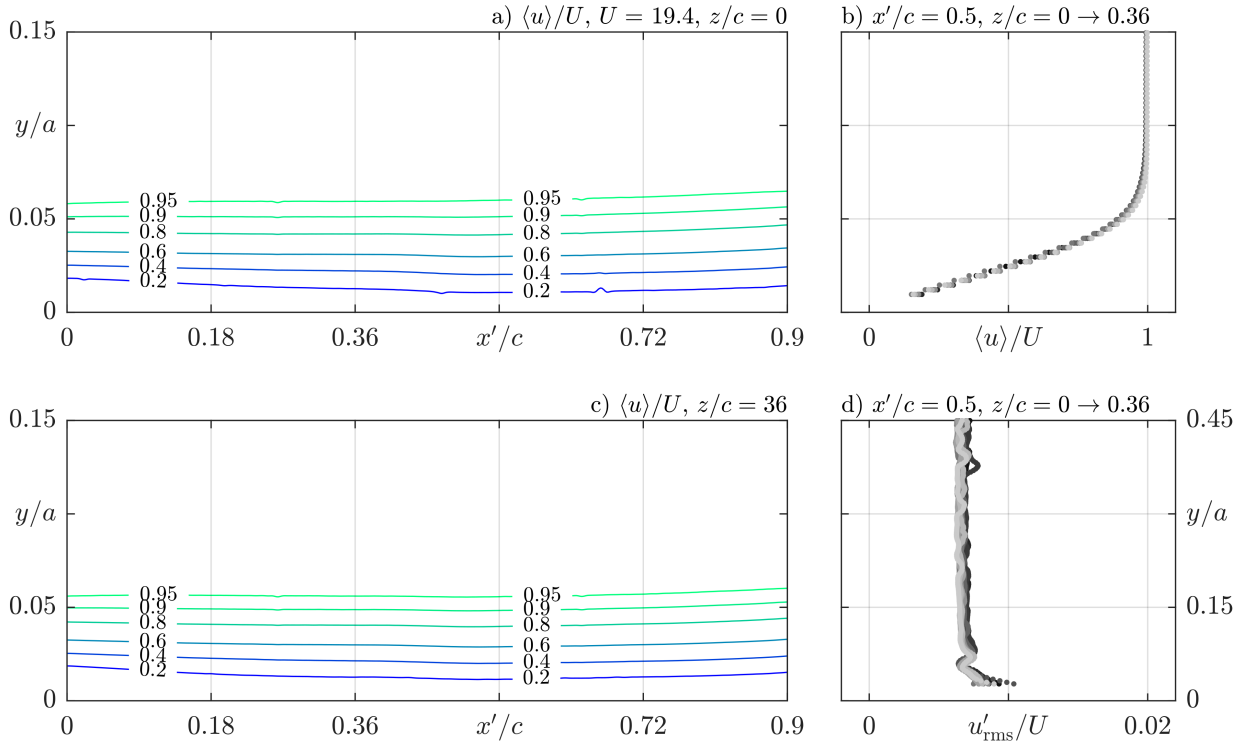


**Figure C-4. Summary of PIV measurements for Baseline,  $Re_{D_h} = 35,500$  case at  $x/a = 2$ .**

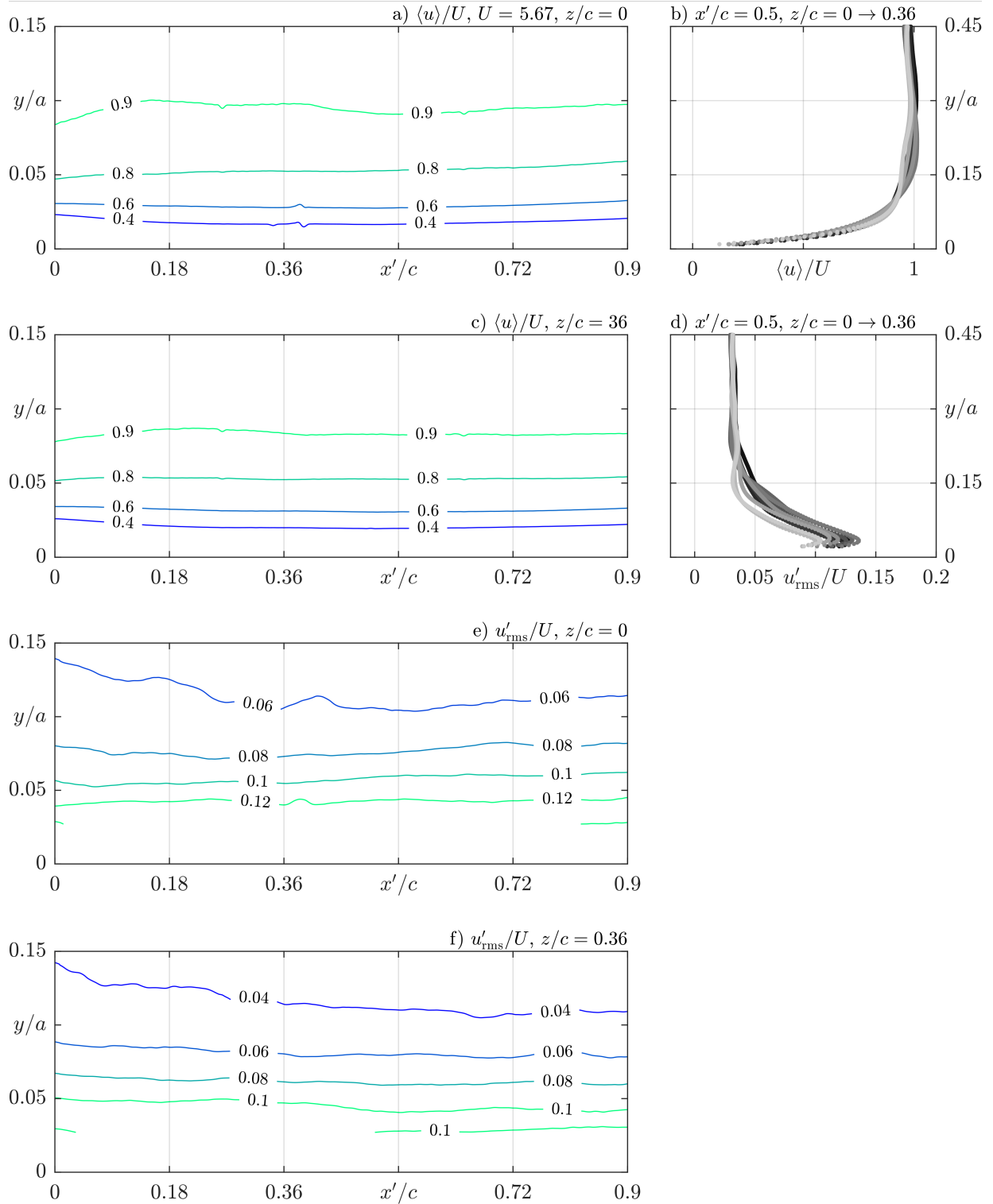


**Figure C-5. Summary of PIV measurements for Grid 3,  $Re_{D_h} = 10,650$  case at  $x/a = 2$ .**

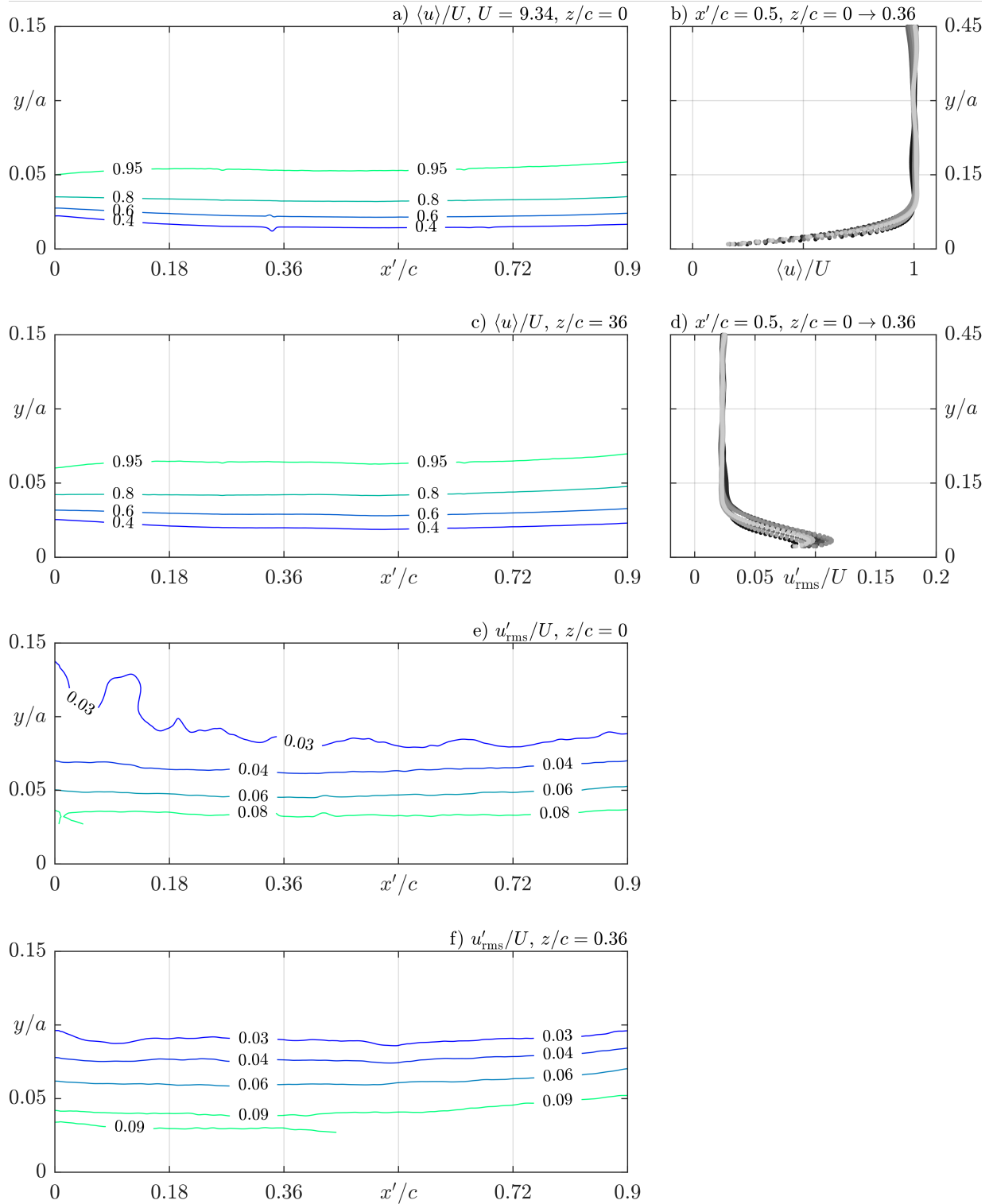


**Figure C-6. Summary of PIV measurements for Grid 1,  $Re_{D_h} = 17,750$  case at  $x/a = 2$ .**

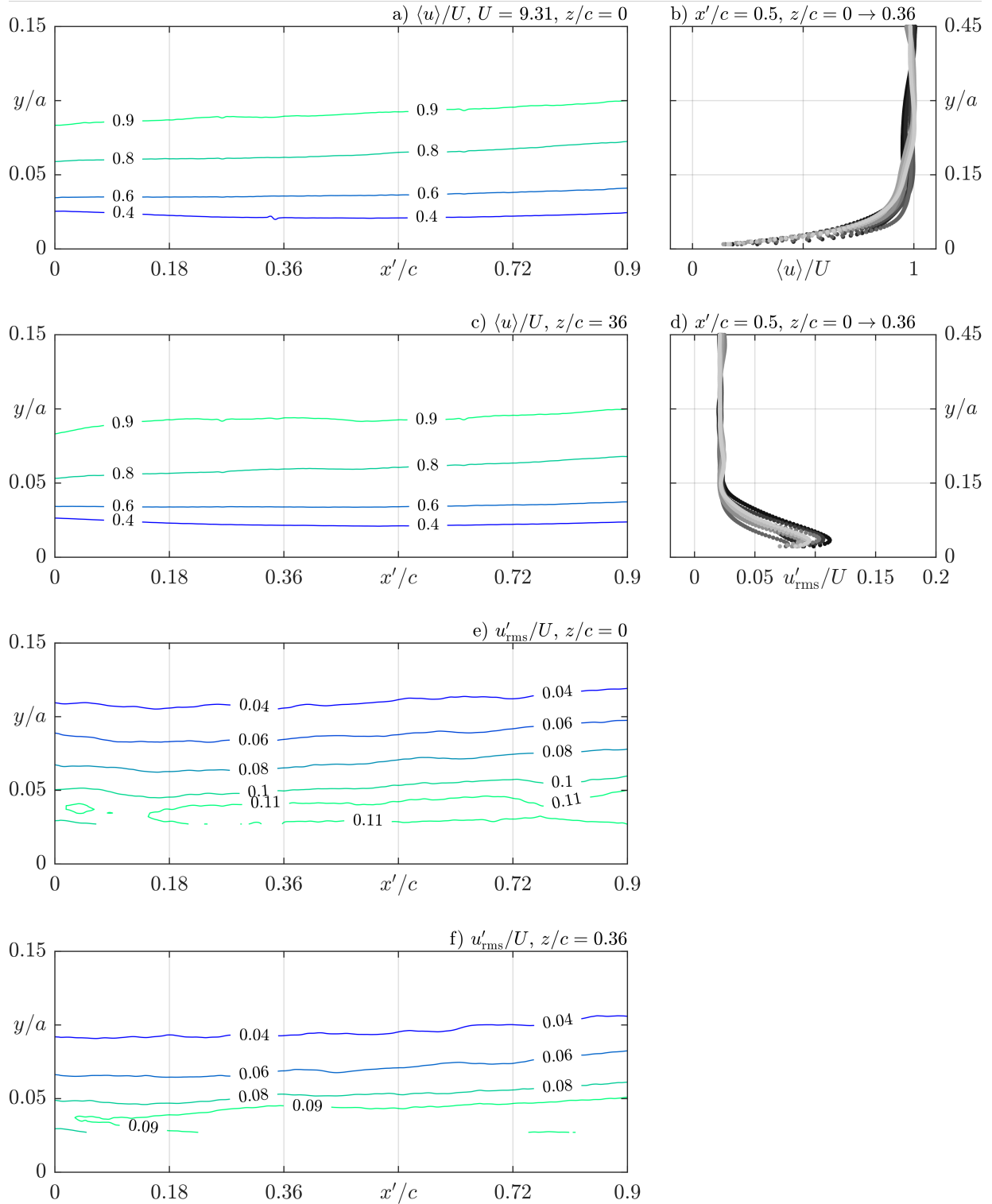


**Figure C-7. Summary of PIV measurements for Grid 2,  $Re_{D_h} = 17,750$  case at  $x/a = 2$ .**

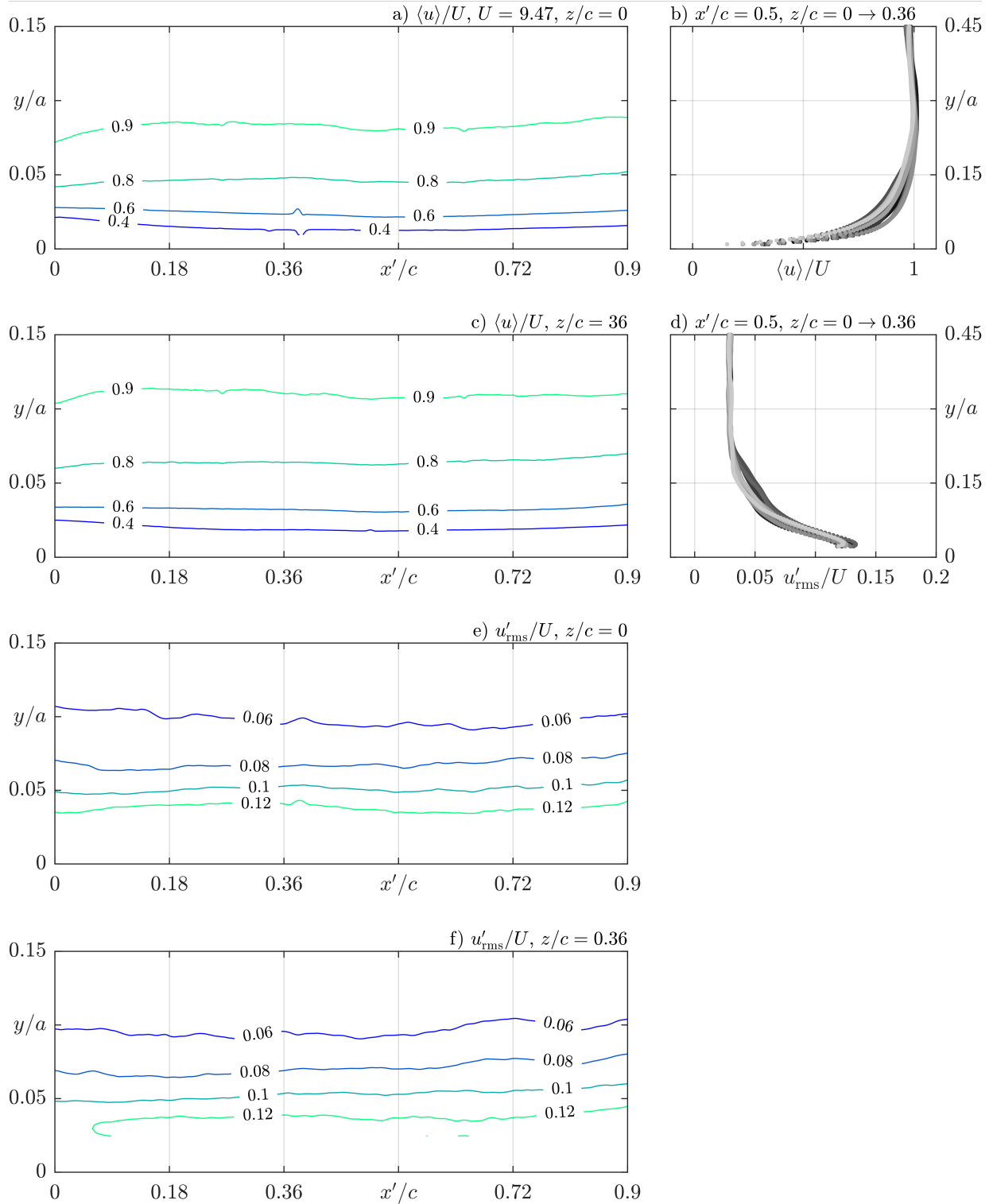


**Figure C-8. Summary of PIV measurements for Grid 3,  $Re_{D_h} = 17,750$  case at  $x/a = 2$ .**

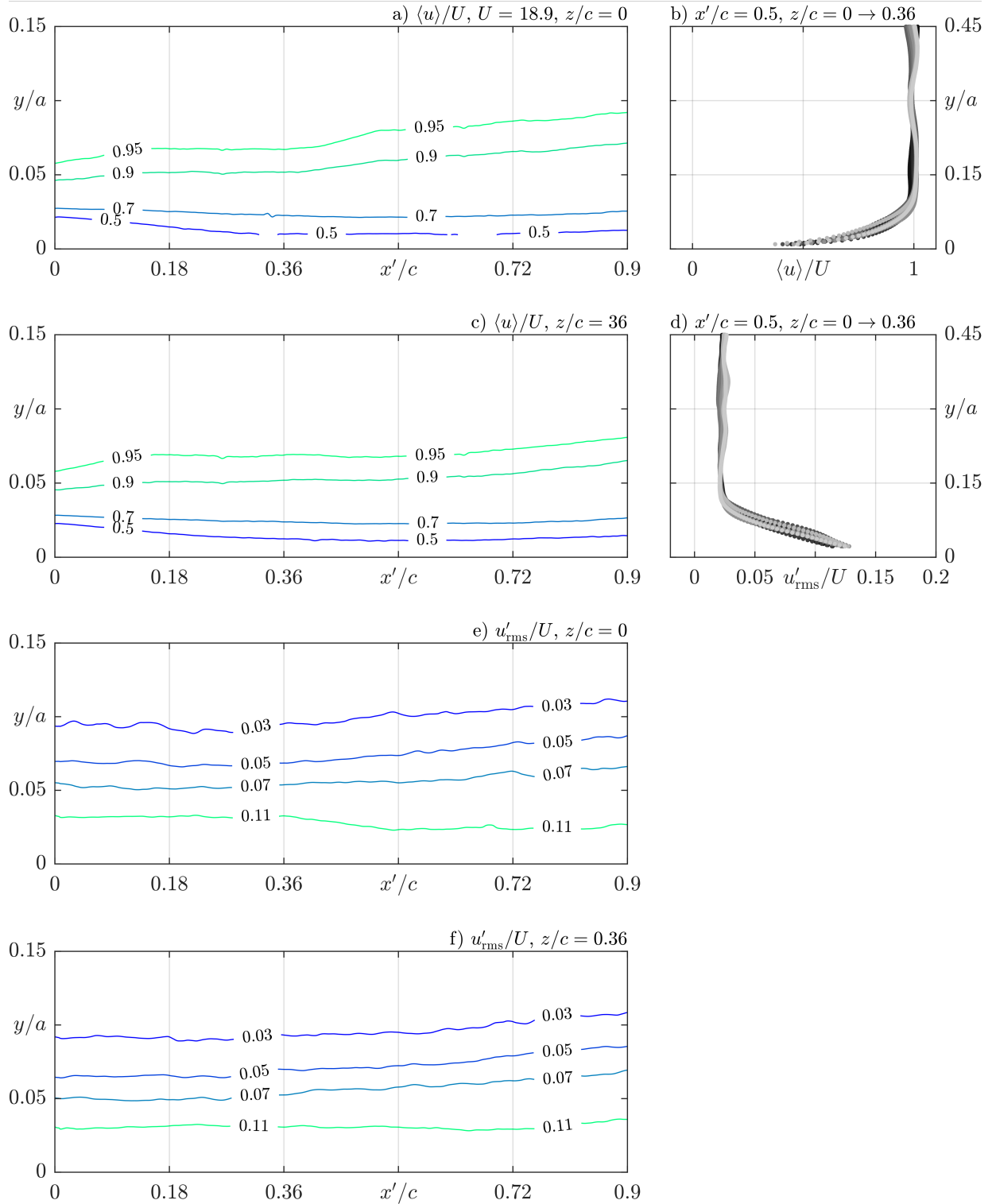


**Figure C-9. Summary of PIV measurements for Grid 1,  $Re_{D_h} = 35,500$  case at  $x/a = 2$ .**

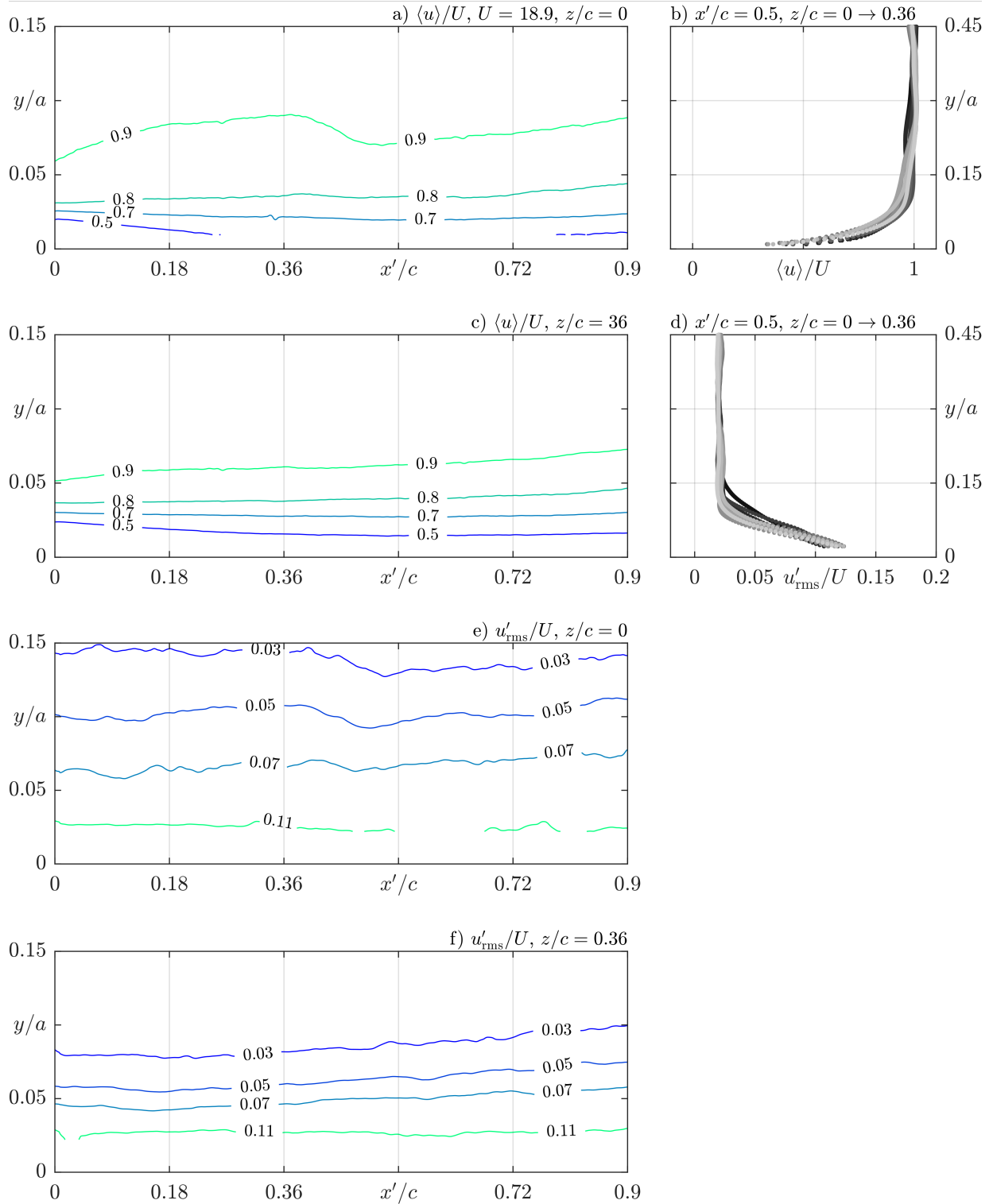


**Figure C-10. Summary of PIV measurements for Grid 2,  $Re_{D_h} = 35,500$  case at  $x/a = 2$ .**

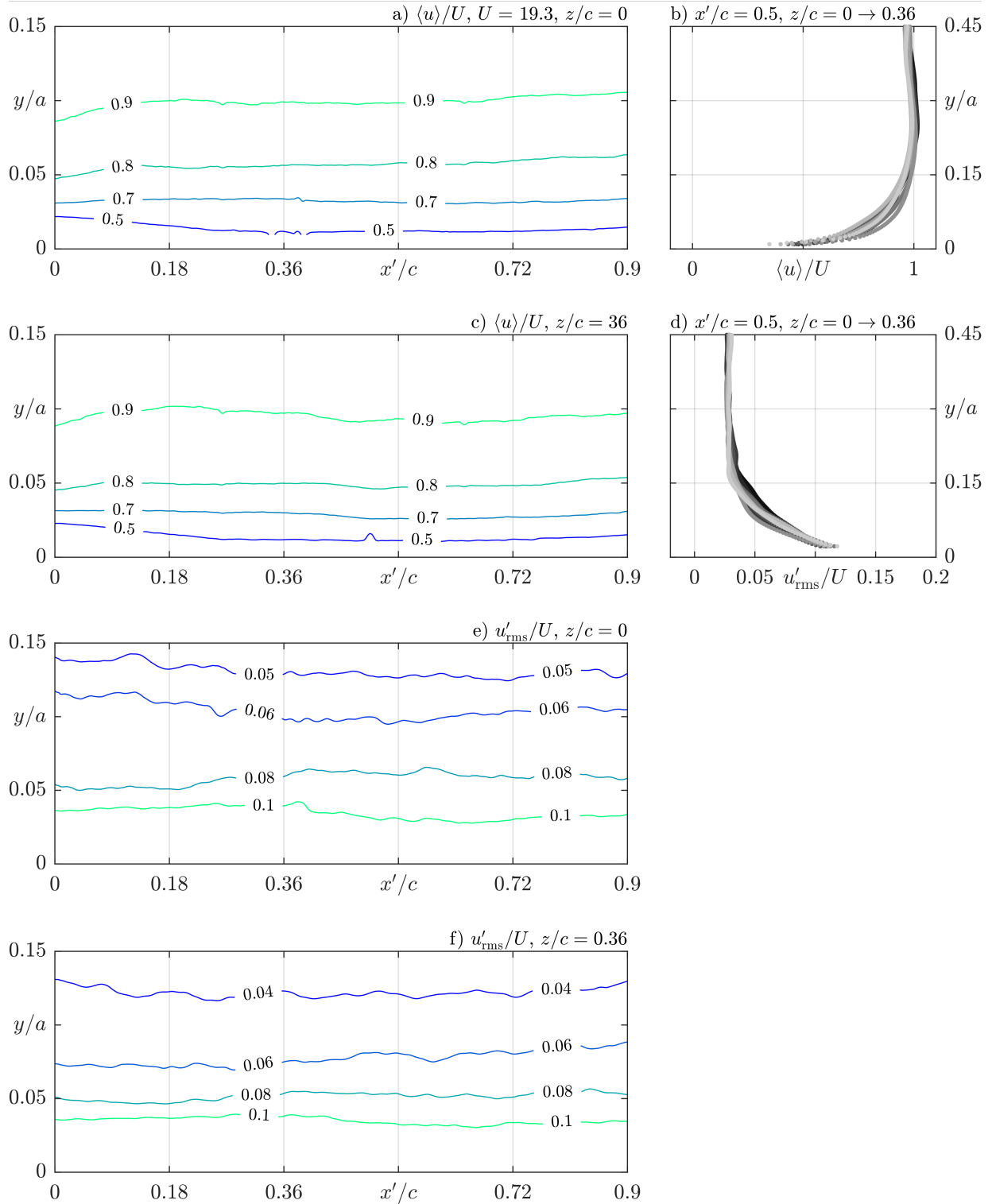


**Figure C-11. Summary of PIV measurements for Grid 3,  $Re_{D_h} = 35,500$  case at  $x/a = 2$ .**



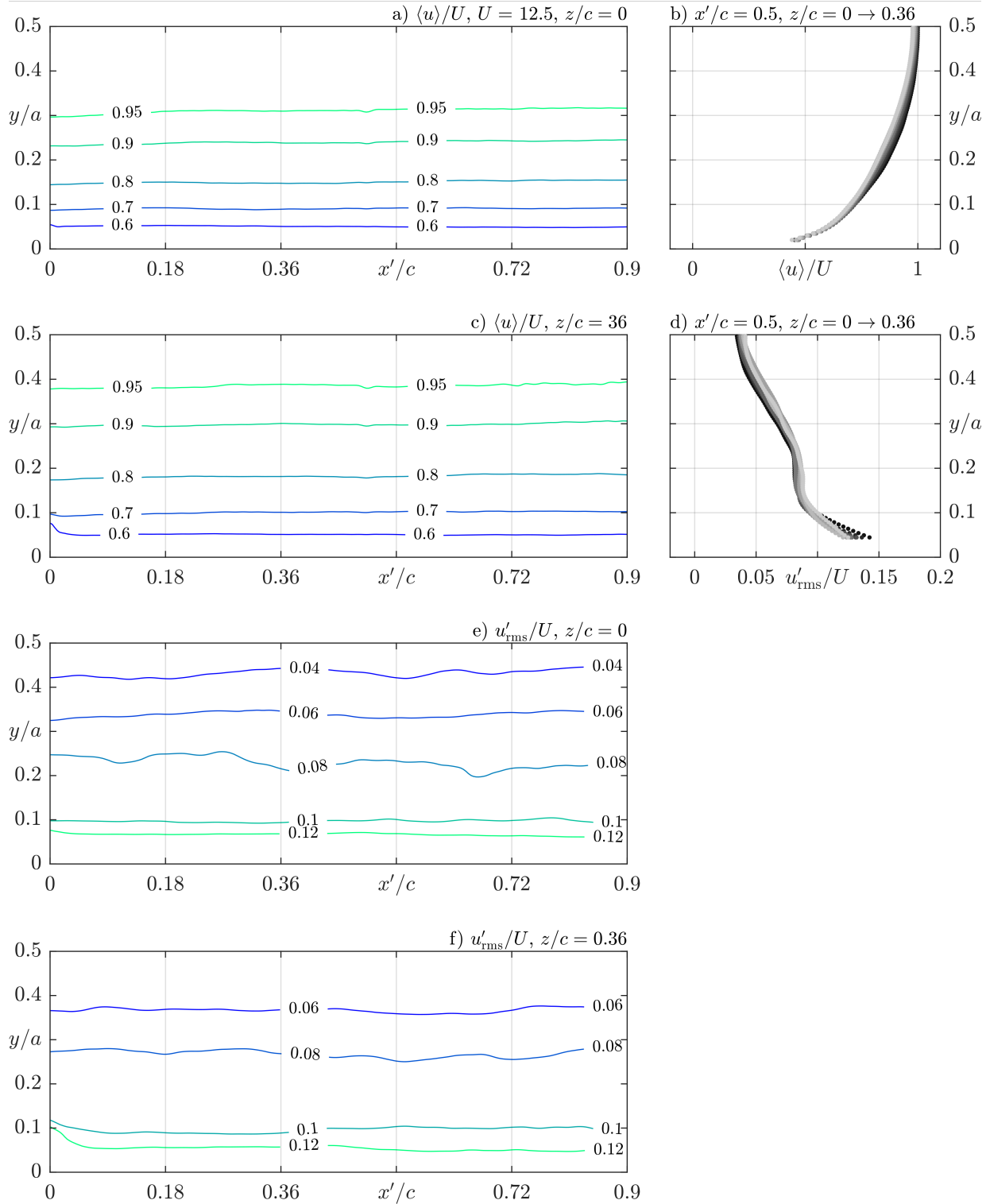


**Figure C-12. Summary of PIV measurements for Baseline,  $Re_{D_h} = 17,750$  case at  $x/a = 45$ .**

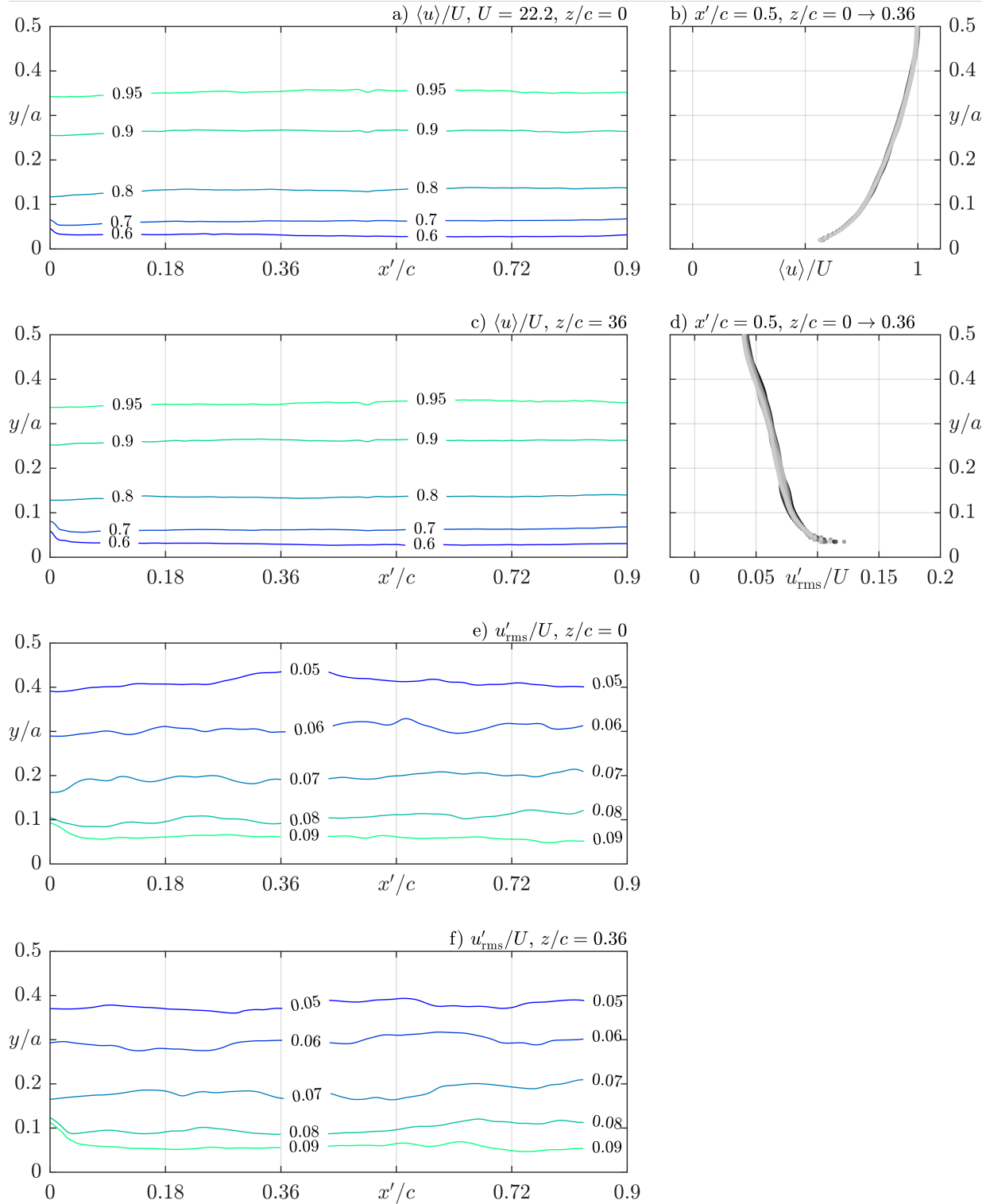


**Figure C-13. Summary of PIV measurements for Baseline,  $Re_{D_h} = 35,500$  case at  $x/a = 45$ .**

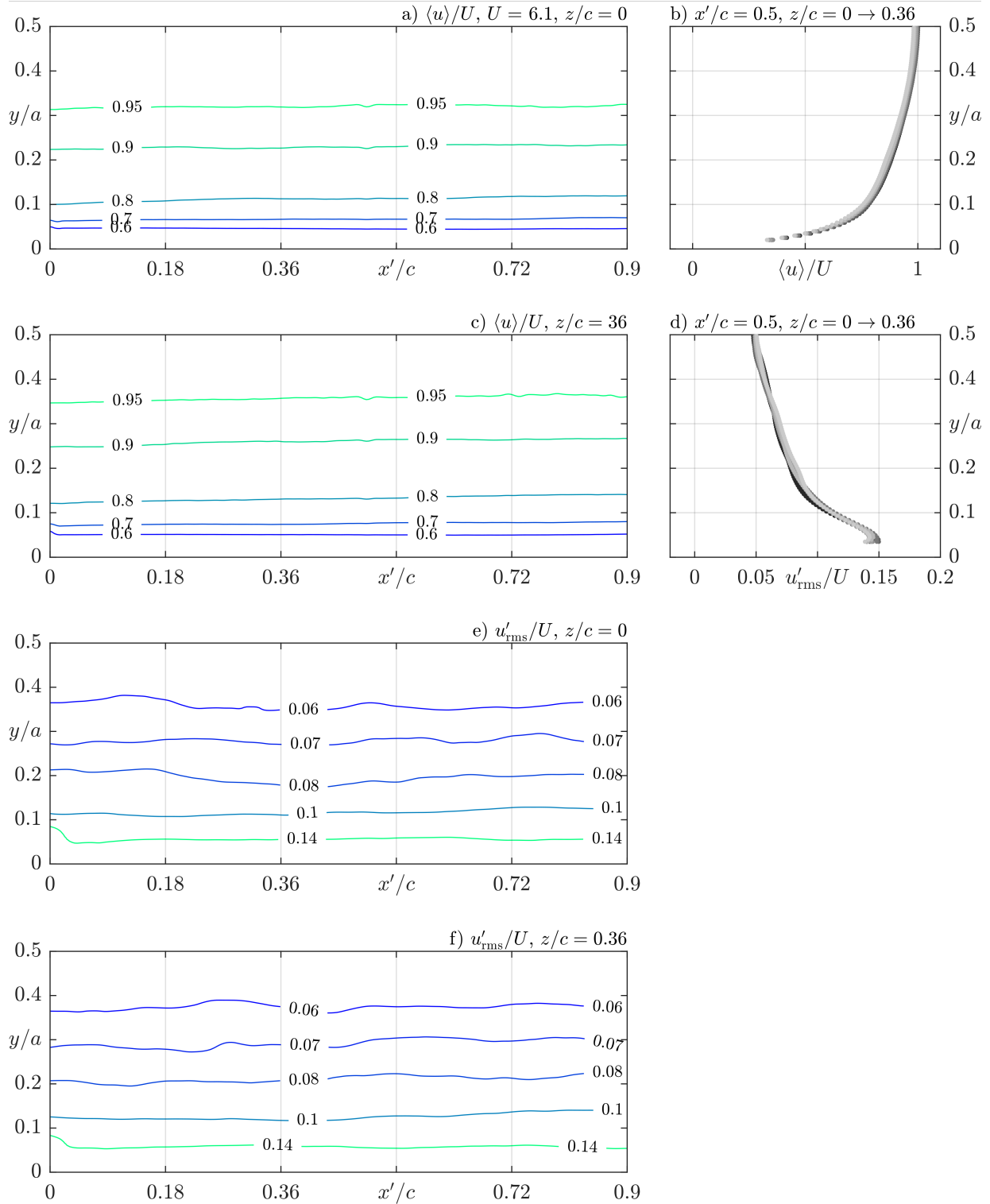


**Figure C-14. Summary of PIV measurements for Grid 3,  $Re_{D_h} = 10,650$  case at  $x/a = 45$ .**

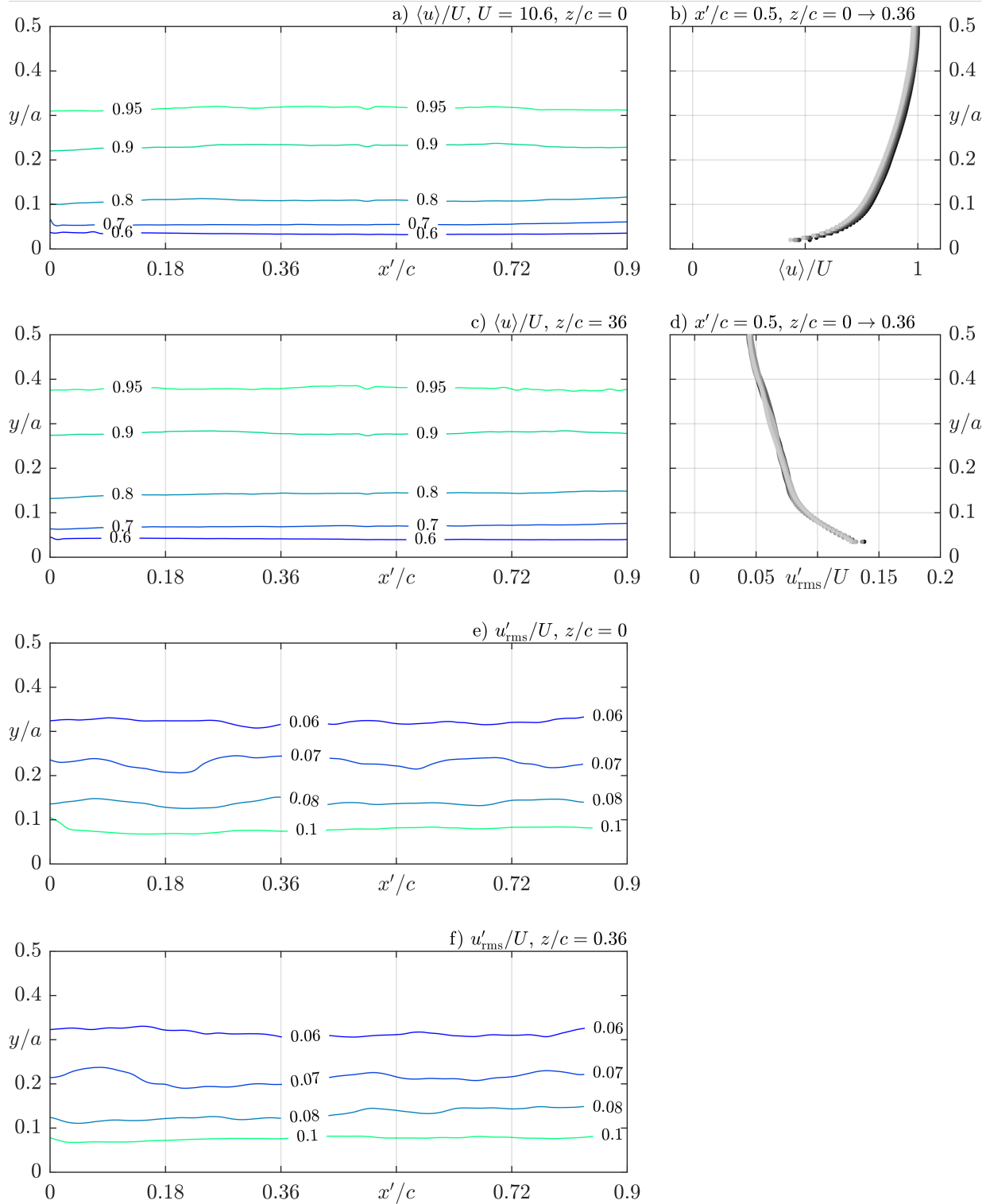


**Figure C-15. Summary of PIV measurements for Grid 1,  $Re_{D_h} = 17,750$  case at  $x/a = 45$ .**

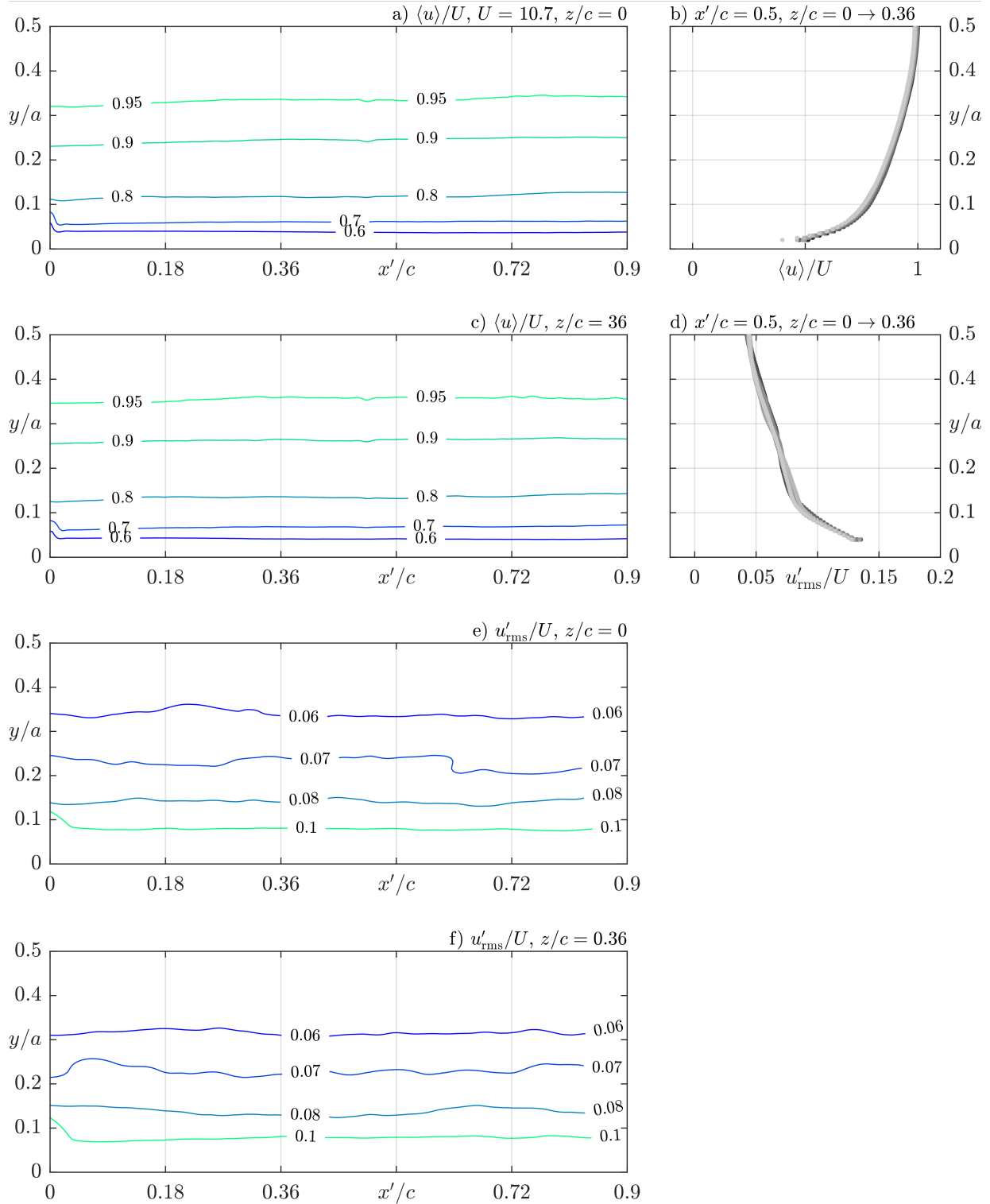


**Figure C-16. Summary of PIV measurements for Grid 2,  $Re_{D_h} = 17,750$  case at  $x/a = 45$ .**

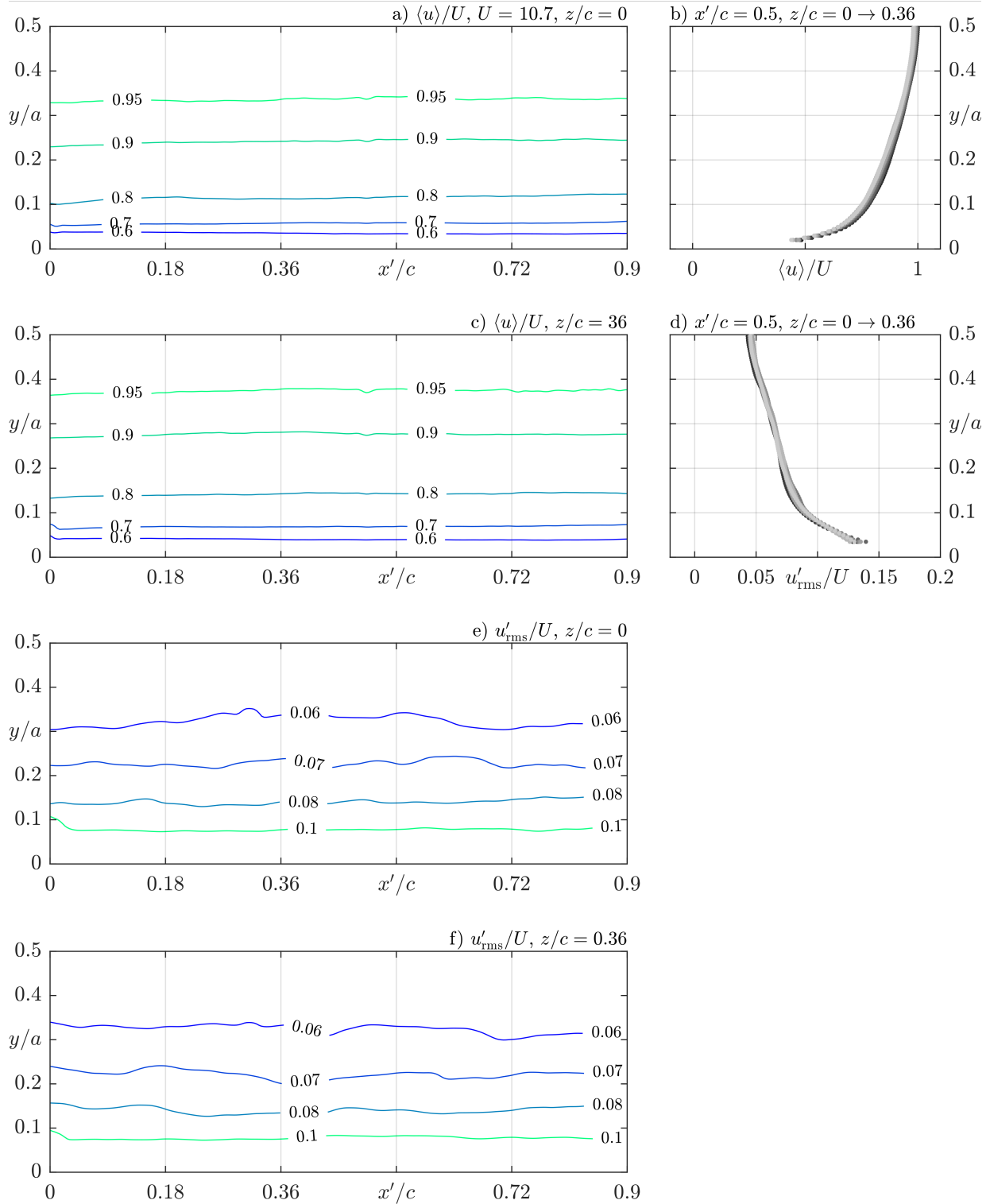


**Figure C-17. Summary of PIV measurements for Grid 3,  $Re_{D_h} = 17,750$  case at  $x/a = 45$ .**

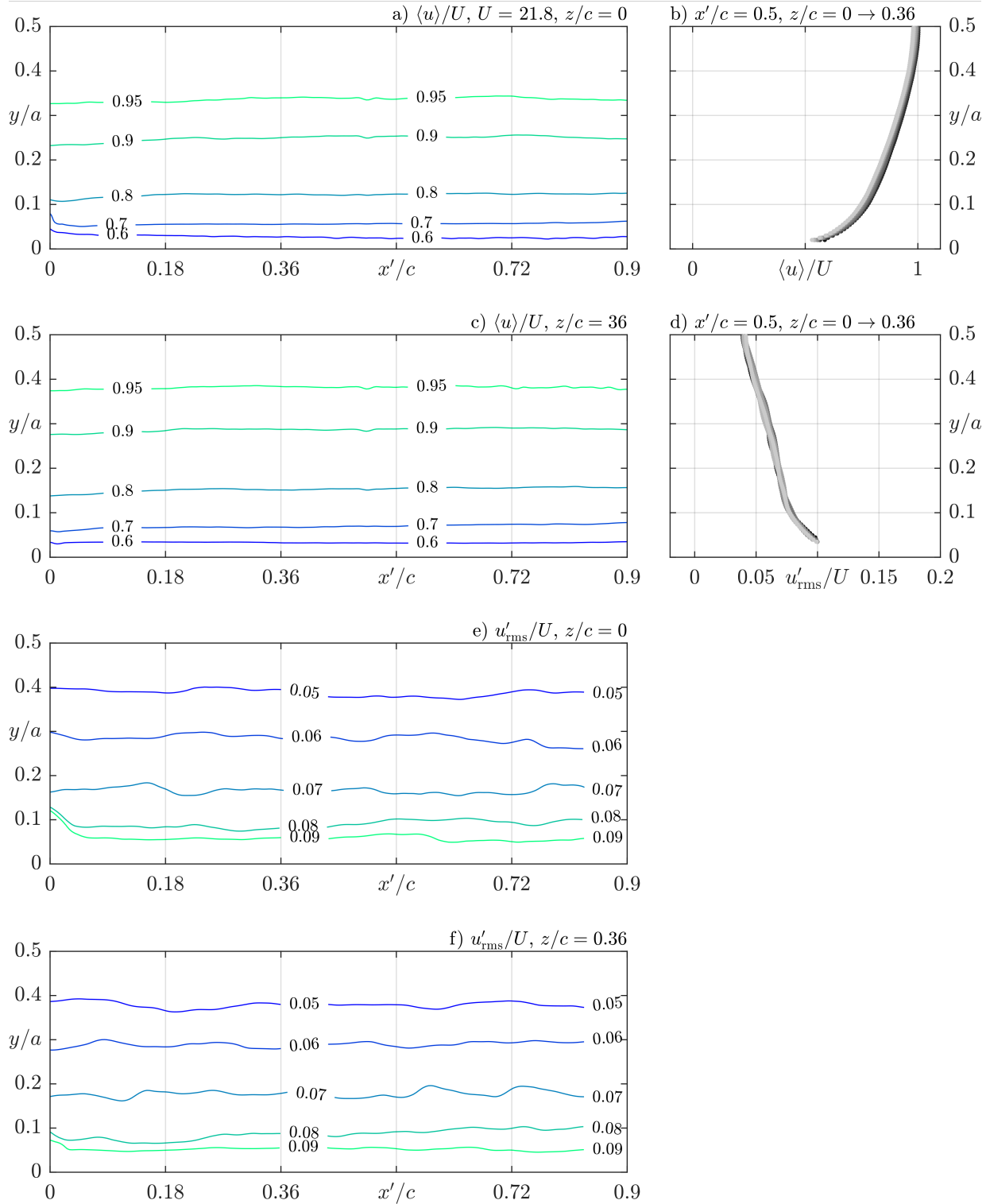


**Figure C-18. Summary of PIV measurements for Grid 1,  $Re_{D_h} = 35,500$  case at  $x/a = 45$ .**

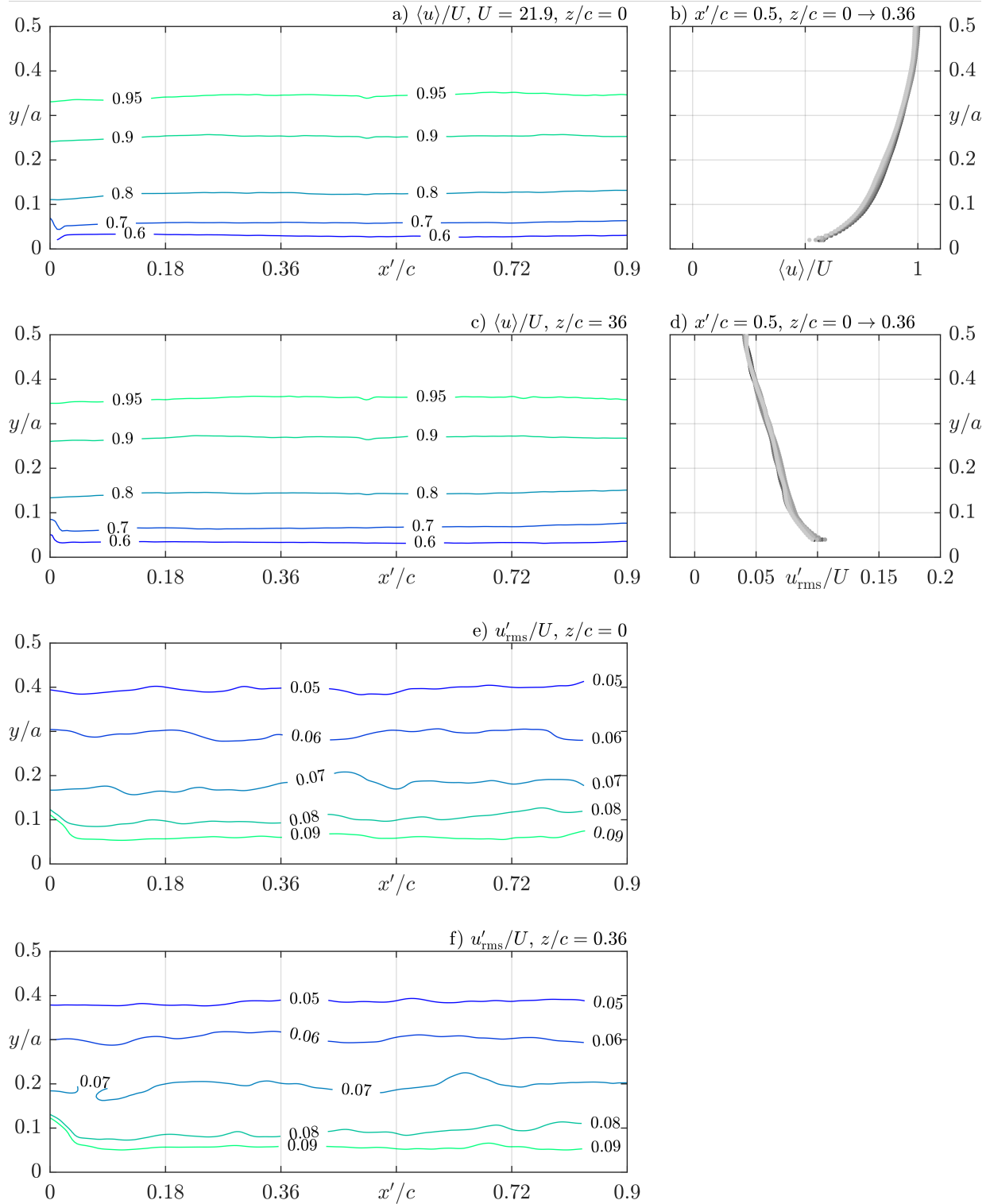


**Figure C-19. Summary of PIV measurements for Grid 2,  $Re_{D_h} = 35,500$  case at  $x/a = 45$ .**



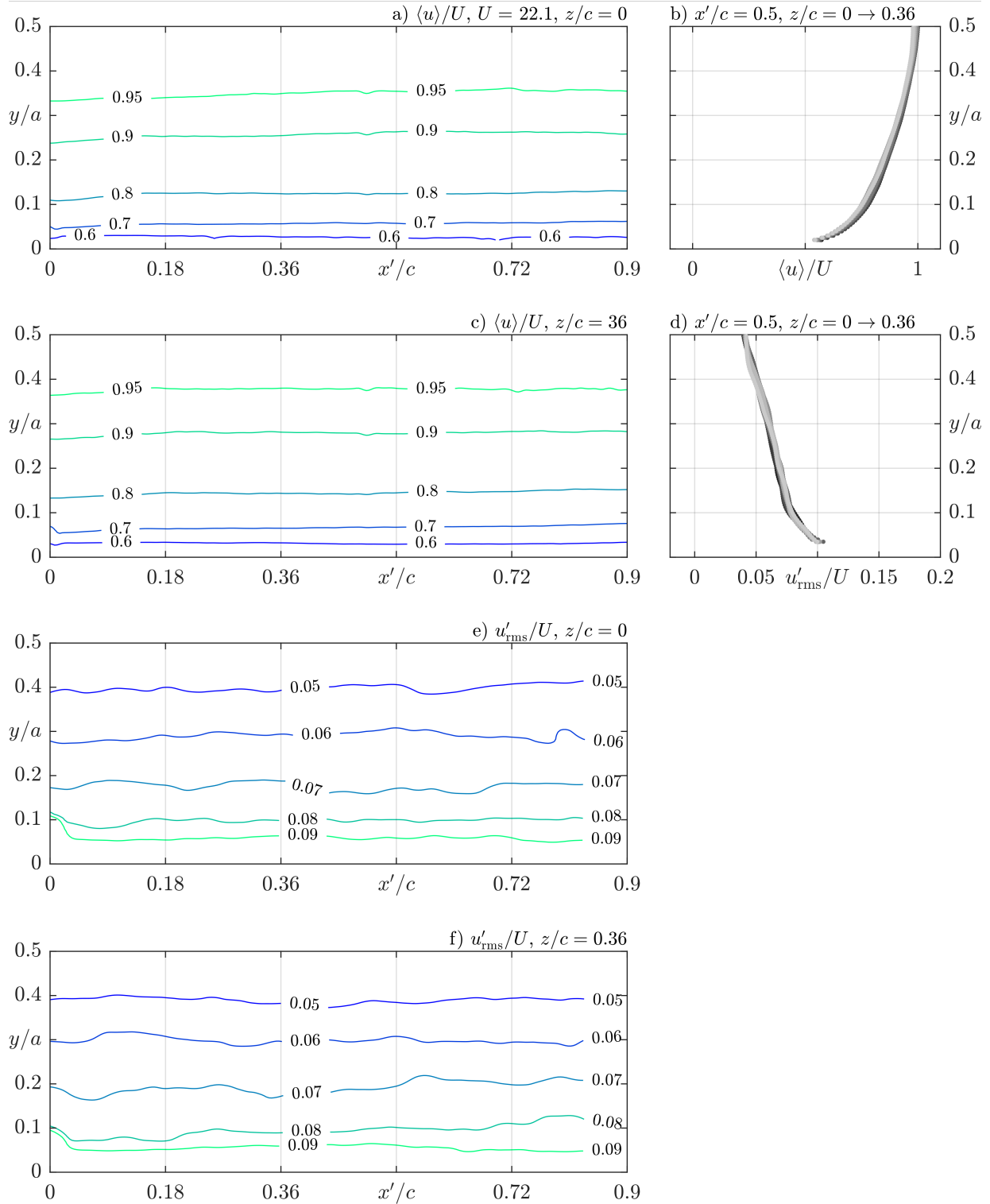


**Figure C-20. Summary of PIV measurements for Grid 3,  $Re_{D_h} = 35,500$  case at  $x/a = 45$ .**

# Appendix D – Evaporation Measurement Data

Each evaporation measurement taken in the foregoing work is tabulated below in Tables D-1 through D-10. The mean evaporated mass over each of the 5 (or 10) measurements for each exposure time ( $t$ ) is given as  $\bar{m}_{\text{evap}}$ . Similarly, the mean initial film mass is given by  $\bar{m}_o$ .

Consequently, the standard deviation for the  $m_{\text{evap},i}$  samples is given by:

$$\sigma = \sqrt{\frac{1}{N} \sum_{i=1}^N \left( m_{\text{evap},i} - \bar{m}_{\text{evap}} \right)^2} \quad (\text{D-1})$$

**Table D-1. Evaporation data for Natural Convection case ( $\text{Gr}_c = 3838$ )**

$t$ (s)	$m_o$ (g)	$m_1$ (g)	$m_i$ (g)	$m_2$ (g)	$m_f$ (g)	$m_{\text{evap}}$ (g)	$\bar{m}_o$ (g)	$\bar{m}_{\text{evap}}$ (g)	$\sigma$ (g)
0	31.50051	31.52660	0.02609	31.52643	0.02592	0.00017	0.02629	0.00020	0.00003
	31.50201	31.52877	0.02676	31.52861	0.02660	0.00016			
	31.50056	31.52659	0.02603	31.52636	0.02580	0.00022			
	31.50211	31.52820	0.02609	31.52801	0.02590	0.00019			
	31.50054	31.52702	0.02648	31.52678	0.02624	0.00024			
150	31.50051	31.52827	0.02776	31.52780	0.02729	0.00047	0.02660	0.00048	0.00003
	31.50201	31.52721	0.02520	31.52672	0.02471	0.00049			
	31.50056	31.52861	0.02805	31.52817	0.02761	0.00044			
	31.50211	31.52655	0.02444	31.52606	0.02395	0.00050			
	31.50054	31.52808	0.02754	31.52756	0.02702	0.00052			
300	31.50197	31.52867	0.02670	31.52789	0.02592	0.00078	0.02641	0.00079	0.00004
	31.50048	31.52665	0.02617	31.52589	0.02541	0.00076			
	31.50192	31.52822	0.02630	31.52747	0.02555	0.00074			
	31.50045	31.52694	0.02649	31.52610	0.02565	0.00084			
	31.50191	31.52831	0.02640	31.52749	0.02558	0.00082			
450	31.50213	31.52820	0.02607	31.52722	0.02509	0.00098	0.02615	0.00104	0.00006
	31.50077	31.52678	0.02601	31.52575	0.02498	0.00103			
	31.50191	31.52820	0.02629	31.52719	0.02528	0.00101			
	31.50057	31.52659	0.02602	31.52555	0.02498	0.00103			
	31.50207	31.52815	0.02608	31.52713	0.02506	0.00102			
	31.50045	31.52665	0.02620	31.52568	0.02523	0.00097			
	31.50207	31.52823	0.02616	31.52715	0.02508	0.00108			
	31.50056	31.52686	0.02630	31.52568	0.02512	0.00117			
	31.50210	31.52815	0.02605	31.52711	0.02501	0.00104			
	31.50056	31.52687	0.02631	31.52576	0.02520	0.00111			
600	31.50052	31.52686	0.02634	31.52549	0.02497	0.00137	0.02628	0.00135	0.00006
	31.50196	31.52810	0.02614	31.52683	0.02487	0.00127			
	31.50050	31.52670	0.02620	31.52534	0.02484	0.00136			
	31.50191	31.52832	0.02641	31.52690	0.02499	0.00142			
	31.50046	31.52675	0.02629	31.52545	0.02499	0.00130			

**Table D-2. Evaporation data for Baseline,  $\text{Re}_{D_h} = 17,750$  case ( $x/a = 2$ )**

$t$	$m_o$	$m_1$	$m_i$	$m_2$	$m_f$	$m_{\text{evap}}$	$\bar{m}_o$	$\bar{m}_{\text{evap}}$	$\sigma$
0	31.26419	31.29062	0.02643	31.29038	0.02619	0.00024	0.02640	0.00017	0.00005
	31.26409	31.29039	0.02630	31.29021	0.02612	0.00018			
	31.26405	31.29063	0.02658	31.29052	0.02647	0.00011			
	31.26409	31.29018	0.02609	31.28998	0.02589	0.00020			
	31.26414	31.29076	0.02662	31.29063	0.02649	0.00013			
25	56.51333	56.53975	0.02642	56.53913	0.02580	0.00063	0.02647	0.00051	0.00008
	56.51318	56.53968	0.02650	56.53925	0.02607	0.00043			
	56.51314	56.53937	0.02623	56.53889	0.02575	0.00048			
	56.51306	56.54000	0.02694	56.53955	0.02649	0.00044			
	56.51313	56.53939	0.02626	56.53883	0.02570	0.00057			
50	56.51332	56.54013	0.02681	56.53933	0.02601	0.00081	0.02657	0.00075	0.00007
	56.51325	56.53984	0.02659	56.53905	0.02580	0.00079			
	56.51319	56.53964	0.02645	56.53893	0.02574	0.00072			
	56.51312	56.53993	0.02681	56.53930	0.02618	0.00063			
	56.51311	56.53931	0.02620	56.53851	0.02540	0.00080			
150	56.51382	56.54053	0.02671	56.53872	0.02490	0.00180	0.02637	0.00172	0.00013
	56.54640	56.57263	0.02623	56.57116	0.02476	0.00147			
	56.51371	56.54033	0.02662	56.53875	0.02504	0.00158			
	56.51366	56.53980	0.02614	56.53806	0.02440	0.00174			
	56.51361	56.53962	0.02601	56.53793	0.02432	0.00168			
	56.51336	56.53946	0.02610	56.53787	0.02451	0.00159			
	56.51323	56.53932	0.02609	56.53746	0.02423	0.00186			
	56.51316	56.53975	0.02659	56.53798	0.02482	0.00177			
	56.51315	56.53999	0.02684	56.53822	0.02507	0.00177			
	56.51329	56.53966	0.02637	56.53777	0.02448	0.00190			

**Table D-3. Evaporation data for Baseline,  $Re_{D_h} = 10,650$  case ( $x/a = 2$ )**

$t$	$m_o$	$m_1$	$m_i$	$m_2$	$m_f$	$m_{\text{evap}}$	$\bar{m}_o$	$\bar{m}_{\text{evap}}$	$\sigma$
0	56.51300	56.53944	0.02644	56.53918	0.02618	0.00025	0.02663	0.00017	0.00006
	56.51286	56.53973	0.02687	56.53953	0.02667	0.00020			
	56.51282	56.53910	0.02628	56.53894	0.02612	0.00016			
	56.51271	56.53943	0.02672	56.53930	0.02659	0.00013			
	56.51270	56.53955	0.02685	56.53943	0.02673	0.00012			
25	56.51295	56.53978	0.02683	56.53937	0.02642	0.00041	0.02660	0.00037	0.00003
	56.51290	56.53972	0.02682	56.53939	0.02649	0.00033			
	56.51293	56.53934	0.02641	56.53896	0.02603	0.00038			
	56.51291	56.53936	0.02645	56.53898	0.02607	0.00038			
	56.51275	56.53925	0.02650	56.53891	0.02616	0.00034			
50	56.51286	56.53973	0.02687	56.53918	0.02632	0.00056	0.02662	0.00055	0.00007
	56.51283	56.53926	0.02643	56.53870	0.02587	0.00056			
	56.51263	56.53913	0.02650	56.53868	0.02605	0.00045			
	56.51278	56.53935	0.02657	56.53872	0.02594	0.00063			
	56.51264	56.53937	0.02673	56.53881	0.02617	0.00056			
150	56.51262	56.53940	0.02678	56.53822	0.02560	0.00118	0.02656	0.00104	0.00008
	56.51243	56.53895	0.02652	56.53799	0.02556	0.00096			
	56.51242	56.53896	0.02654	56.53792	0.02550	0.00104			
	56.51230	56.53908	0.02678	56.53804	0.02574	0.00103			
	56.51220	56.53837	0.02617	56.53735	0.02515	0.00101			

**Table D-4. Evaporation data for Baseline,  $Re_{D_h} = 35,500$  case ( $x/a = 2$ )**

$t$	$m_o$	$m_1$	$m_i$	$m_2$	$m_f$	$m_{\text{evap}}$	$\bar{m}_o$	$\bar{m}_{\text{evap}}$	$\sigma$
0	56.51360	56.54008	0.02648	56.53988	0.02628	0.00020	0.02649	0.00017	0.00006
	56.51348	56.53990	0.02642	56.53967	0.02619	0.00023			
	56.51375	56.54007	0.02632	56.53986	0.02611	0.00020			
	56.51352	56.54041	0.02689	56.54031	0.02679	0.00010			
	56.51336	56.53971	0.02635	56.53960	0.02624	0.00011			
25	56.51313	56.53982	0.02669	56.53902	0.02589	0.00079	0.02661	0.00073	0.00009
	56.51305	56.53984	0.02679	56.53926	0.02621	0.00059			
	56.51316	56.53925	0.02609	56.53853	0.02537	0.00072			
	56.51324	56.53979	0.02655	56.53897	0.02573	0.00082			
	56.51322	56.54014	0.02692	56.53940	0.02618	0.00074			
50	56.51349	56.53977	0.02628	56.53862	0.02513	0.00115	0.02657	0.00123	0.00005
	56.51348	56.54028	0.02680	56.53904	0.02556	0.00124			
	56.51353	56.54030	0.02677	56.53902	0.02549	0.00128			
	56.51338	56.54006	0.02668	56.53880	0.02542	0.00126			
	56.51346	56.53980	0.02634	56.53856	0.02510	0.00124			
150	56.51333	56.53959	0.02626	56.53689	0.02356	0.00270	0.02636	0.00272	0.00005
	56.51353	56.54004	0.02651	56.53731	0.02378	0.00272			
	56.51323	56.53976	0.02653	56.53703	0.02380	0.00273			
	56.51323	56.53952	0.02629	56.53674	0.02351	0.00278			
	56.51310	56.53933	0.02623	56.53667	0.02357	0.00265			

**Table D-5. Evaporation data for Grid 1,  $Re_{D_h} = 10,650$  case ( $x/a = 2$ )**

$t$	$m_o$	$m_1$	$m_i$	$m_2$	$m_f$	$m_{\text{evap}}$	$\bar{m}_o$	$\bar{m}_{\text{evap}}$	$\sigma$
0	56.51162	56.53786	0.02624	56.53774	0.02612	0.00012	0.02649	0.00018	0.00005
	56.51157	56.53801	0.02644	56.53788	0.02631	0.00013			
	56.51146	56.53811	0.02665	56.53791	0.02645	0.00020			
	56.51155	56.53800	0.02645	56.53775	0.02620	0.00025			
	56.51147	56.53813	0.02666	56.53794	0.02647	0.00018			
25	56.51153	56.53817	0.02664	56.53784	0.02631	0.00033	0.02648	0.00031	0.00004
	56.51141	56.53787	0.02646	56.53758	0.02617	0.00029			
	56.51156	56.53782	0.02626	56.53750	0.02594	0.00032			
	56.51141	56.53781	0.02640	56.53757	0.02616	0.00024			
	56.51144	56.53805	0.02661	56.53771	0.02627	0.00035			
50	56.51143	56.53800	0.02657	56.53751	0.02608	0.00049	0.02645	0.00050	0.00005
	56.51135	56.53766	0.02631	56.53722	0.02587	0.00044			
	56.51133	56.53775	0.02642	56.53724	0.02591	0.00051			
	56.51140	56.53807	0.02667	56.53751	0.02611	0.00057			
	56.51136	56.53763	0.02627	56.53712	0.02576	0.00051			
150	56.51165	56.53813	0.02648	56.53683	0.02518	0.00130	0.02640	0.00119	0.00013
	56.51152	56.53814	0.02662	56.53693	0.02541	0.00121			
	56.51162	56.53773	0.02611	56.53640	0.02478	0.00133			
	56.51145	56.53806	0.02661	56.53701	0.02556	0.00105			
	56.51134	56.53752	0.02618	56.53645	0.02511	0.00107			

**Table D-6. Evaporation data for Grid 1,  $Re_{D_h} = 17,750$  case ( $x/a = 2$ )**

$t$	$m_o$	$m_1$	$m_i$	$m_2$	$m_f$	$m_{\text{evap}}$	$\bar{m}_o$	$\bar{m}_{\text{evap}}$	$\sigma$
0	56.51308	56.53969	0.02661	56.53959	0.02651	0.00010	0.02654	0.00015	0.00003
	56.51300	56.53940	0.02640	56.53921	0.02621	0.00019			
	56.51294	56.53955	0.02661	56.53939	0.02645	0.00015			
	56.51290	56.53938	0.02648	56.53923	0.02633	0.00015			
	56.51295	56.53954	0.02659	56.53941	0.02646	0.00013			
25	56.51298	56.53959	0.02661	56.53907	0.02609	0.00052	0.02646	0.00053	0.00003
	56.51296	56.53920	0.02624	56.53866	0.02570	0.00055			
	56.51283	56.53947	0.02664	56.53899	0.02616	0.00048			
	56.51299	56.53947	0.02648	56.53891	0.02592	0.00056			
	56.51308	56.53939	0.02631	56.53884	0.02576	0.00055			
50	56.51306	56.53964	0.02658	56.53878	0.02572	0.00086	0.02668	0.00081	0.00003
	56.51294	56.53971	0.02677	56.53891	0.02597	0.00080			
	56.51299	56.53933	0.02634	56.53853	0.02554	0.00080			
	56.51295	56.53975	0.02680	56.53895	0.02600	0.00080			
	56.51284	56.53973	0.02689	56.53896	0.02612	0.00077			
150	56.51299	56.53972	0.02673	56.53815	0.02516	0.00157	0.02673	0.00155	0.00003
	56.51292	56.53950	0.02658	56.53794	0.02502	0.00156			
	56.51289	56.53951	0.02662	56.53795	0.02506	0.00156			
	56.51283	56.53963	0.02680	56.53808	0.02525	0.00155			
	56.51281	56.53971	0.02690	56.53821	0.02540	0.00150			

**Table D-7. Evaporation data for Grid 2,  $Re_{D_h} = 17,750$  case ( $x/a = 2$ )**

$t$	$m_o$	$m_1$	$m_i$	$m_2$	$m_f$	$m_{\text{evap}}$	$\bar{m}_o$	$\bar{m}_{\text{evap}}$	$\sigma$
0	56.51303	56.53950	0.02647	56.53935	0.02632	0.00015	0.02652	0.00015	0.00003
	56.51295	56.53951	0.02656	56.53937	0.02642	0.00014			
	56.51298	56.53956	0.02658	56.53938	0.02640	0.00018			
	56.51300	56.53946	0.02646	56.53930	0.02630	0.00016			
	56.51270	56.53924	0.02654	56.53913	0.02643	0.00011			
25	56.51304	56.53926	0.02622	56.53868	0.02564	0.00058	0.02643	0.00050	0.00006
	56.51301	56.53927	0.02626	56.53879	0.02578	0.00048			
	56.51292	56.53963	0.02671	56.53922	0.02630	0.00041			
	56.51296	56.53942	0.02646	56.53888	0.02592	0.00054			
	56.51290	56.53940	0.02650	56.53890	0.02600	0.00050			
50	56.51290	56.53935	0.02645	56.53856	0.02566	0.00079	0.02665	0.00074	0.00005
	56.51288	56.53966	0.02678	56.53894	0.02606	0.00072			
	56.51293	56.53950	0.02657	56.53878	0.02585	0.00073			
	56.51302	56.53994	0.02692	56.53927	0.02625	0.00067			
	56.51306	56.53958	0.02652	56.53881	0.02575	0.00077			
150	56.51325	56.53942	0.02617	56.53773	0.02448	0.00169	0.02653	0.00170	0.00008
	56.51315	56.53953	0.02638	56.53795	0.02480	0.00158			
	56.51315	56.53990	0.02675	56.53810	0.02495	0.00180			
	56.51303	56.53993	0.02690	56.53825	0.02522	0.00168			
	56.51295	56.53941	0.02646	56.53767	0.02472	0.00174			

**Table D-8. Evaporation data for Grid 3,  $Re_{D_h} = 17,750$  case ( $x/a = 2$ )**

$t$	$m_o$	$m_1$	$m_i$	$m_2$	$m_f$	$m_{\text{evap}}$	$\bar{m}_o$	$\bar{m}_{\text{evap}}$	$\sigma$
0	56.51305	56.53949	0.02644	56.53937	0.02632	0.00012	0.02650	0.00015	0.00003
	56.51293	56.53935	0.02642	56.53918	0.02625	0.00017			
	56.51302	56.53957	0.02655	56.53942	0.02640	0.00015			
	56.51291	56.53938	0.02647	56.53927	0.02636	0.00011			
	56.51296	56.53958	0.02662	56.53939	0.02643	0.00019			
25	56.51307	56.53956	0.02649	56.53901	0.02594	0.00055	0.02655	0.00055	0.00006
	56.51299	56.53947	0.02648	56.53890	0.02591	0.00057			
	56.51283	56.53949	0.02666	56.53902	0.02619	0.00047			
	56.51300	56.53940	0.02640	56.53877	0.02577	0.00063			
	56.51295	56.53966	0.02671	56.53910	0.02615	0.00055			
50	56.51305	56.53959	0.02654	56.53869	0.02564	0.00090	0.02662	0.00083	0.00009
	56.51303	56.53954	0.02651	56.53875	0.02572	0.00079			
	56.51306	56.53967	0.02661	56.53893	0.02587	0.00075			
	56.51301	56.53977	0.02676	56.53901	0.02600	0.00076			
	56.51306	56.53971	0.02665	56.53878	0.02572	0.00094			
150	56.51301	56.53951	0.02650	56.53779	0.02478	0.00171	0.02652	0.00168	0.00007
	56.51295	56.53977	0.02682	56.53812	0.02517	0.00165			
	56.51302	56.53935	0.02633	56.53758	0.02456	0.00177			
	56.51289	56.53929	0.02640	56.53772	0.02483	0.00157			
	56.51275	56.53933	0.02658	56.53765	0.02490	0.00168			

**Table D-9. Evaporation data for Baseline,  $Re_{D_h} = 10,650$  case ( $x/a = 45$ )**

$t$	$m_o$	$m_1$	$m_i$	$m_2$	$m_f$	$m_{\text{evap}}$	$\bar{m}_o$	$\bar{m}_{\text{evap}}$	$\sigma$
0	56.51157	56.53774	0.02617	56.53757	0.02600	0.00017	0.02631	0.00011	0.00004
	56.51138	56.53760	0.02622	56.53753	0.02615	0.00007			
	56.51133	56.53792	0.02659	56.53784	0.02651	0.00008			
	56.51126	56.53755	0.02629	56.53743	0.02617	0.00012			
	56.51124	56.53754	0.02630	56.53745	0.02621	0.00009			
25	56.51148	56.53764	0.02616	56.53737	0.02589	0.00028	0.02641	0.00025	0.00004
	56.51145	56.53772	0.02627	56.53747	0.02602	0.00025			
	56.51149	56.53819	0.02670	56.53790	0.02641	0.00029			
	56.51138	56.53799	0.02661	56.53781	0.02643	0.00018			
	56.51146	56.53774	0.02628	56.53748	0.02602	0.00026			
50	56.51149	56.53789	0.02640	56.53752	0.02603	0.00037	0.02640	0.00036	0.00003
	56.51148	56.53775	0.02627	56.53733	0.02585	0.00041			
	56.51145	56.53783	0.02638	56.53750	0.02605	0.00034			
	56.51144	56.53793	0.02649	56.53758	0.02614	0.00035			
	56.51138	56.53782	0.02644	56.53750	0.02612	0.00033			
150	56.51140	56.53773	0.02633	56.53678	0.02538	0.00095	0.02639	0.00095	0.00003
	56.51138	56.53766	0.02628	56.53669	0.02531	0.00097			
	56.51125	56.53793	0.02668	56.53701	0.02576	0.00092			
	56.51129	56.53774	0.02645	56.53683	0.02554	0.00091			
	56.51125	56.53746	0.02621	56.53647	0.02522	0.00099			

**Table D-10. Evaporation data for Baseline,  $Re_{D_h} = 17,750$  case ( $x/a = 45$ )**

$t$	$m_o$	$m_1$	$m_i$	$m_2$	$m_f$	$m_{\text{evap}}$	$\bar{m}_o$	$\bar{m}_{\text{evap}}$	$\sigma$
0	56.51143	56.53756	0.02613	56.53745	0.02602	0.00011	0.02631	0.00014	0.00004
	56.51142	56.53765	0.02623	56.53755	0.02613	0.00010			
	56.51146	56.53783	0.02637	56.53763	0.02617	0.00020			
	56.51153	56.53806	0.02653	56.53794	0.02641	0.00012			
	56.51150	56.53777	0.02627	56.53761	0.02611	0.00016			
25	56.51150	56.53776	0.02626	56.53731	0.02581	0.00044	0.02646	0.00056	0.00007
	56.51142	56.53771	0.02629	56.53713	0.02571	0.00057			
	56.51150	56.53812	0.02662	56.53750	0.02600	0.00062			
	56.51142	56.53786	0.02644	56.53728	0.02586	0.00058			
	56.51137	56.53804	0.02667	56.53745	0.02608	0.00059			
50	56.51155	56.53792	0.02637	56.53710	0.02555	0.00082	0.02632	0.00090	0.00009
	56.51155	56.53797	0.02642	56.53708	0.02553	0.00088			
	56.51168	56.53783	0.02615	56.53679	0.02511	0.00105			
	56.51147	56.53774	0.02627	56.53684	0.02537	0.00090			
	56.51150	56.53790	0.02640	56.53704	0.02554	0.00086			
150	56.51159	56.53817	0.02658	56.53631	0.02472	0.00186	0.02643	0.00171	0.00013
	56.51158	56.53781	0.02623	56.53605	0.02447	0.00176			
	56.51150	56.53829	0.02679	56.53669	0.02519	0.00161			
	56.51159	56.53789	0.02630	56.53613	0.02454	0.00176			
	56.51160	56.53785	0.02625	56.53630	0.02470	0.00155			